

SYMPATHETIC HEATING AND COOLING OF TRAPPED ATOMIC AND MOLECULAR IONS

A Thesis
Presented to
The Academic Faculty

by

Craig R. Clark

In Partial Fulfillment
of the Requirements for the Degree
Doctor of Philosophy in the
Department of Chemistry and Biochemistry

Georgia Institute of Technology
May 2012

SYMPATHETIC HEATING AND COOLING OF TRAPPED ATOMIC AND MOLECULAR IONS

Approved by:

Professor Kenneth R. Brown, Advisor
Department of Chemistry and
Biochemistry
Georgia Institute of Technology

Professor Jean-Luc Brédas
Department of Chemistry and
Biochemistry
Georgia Institute of Technology

Professor Alex Kuzmich
Department of Physics
Georgia Institute of Technology

Professor David Sherrill
Department of Chemistry and
Biochemistry
Georgia Institute of Technology

Dr. Richard Slusher
Georgia Tech Research Institute
Georgia Institute of Technology

Date Approved: 9 December 2011

ACKNOWLEDGEMENTS

I would like to first express my gratitude to my advisor, Prof. Kenneth Brown, for the continuous support of my Ph.D study and research, for his patience, motivation, enthusiasm, and knowledge. I could not have imagined having a better advisor and mentor for my Ph.D study.

Besides my advisor, I would like to thank the rest of my thesis committee: Prof. Jean-Luc Brédas, Prof. Alex Kuzmich, Prof. David Sherrill, and Dr. Richart Slusher, for their encouragement, insightful comments, and hard questions.

I also would like to thank the Georgia Tech Research Institute and the Robert G. Shackelford fellowship program, for offering me financial support over the course of my graduate study and research.

I thank my fellow labmates in the Brown Group: Dr. C. Ricardo Viteri, James Goeders, Grahame Vittorini, Ncamiso Khanyile, True Merrill, Dr. Gang Shu, Yu Tomita, Mauricio Gutiérrez, Chingiz Kabytayev, and Yatis Dodia for the stimulating discussions, for the sleepless nights we were working together, and for all the fun we have had over the last five years.

I would like to thank my parents, Ron and Diane Clark, for supporting me throughout my life, and teaching me the work ethic needed to accomplish a desired goal.

Last and most importantly, I would like to thank Jesus Christ, my Lord and Savior. I owe my life and everything accomplished in this thesis to Him. For His grace is sufficient for me, and His power is made perfect in my weakness.

TABLE OF CONTENTS

ACKNOWLEDGEMENTS	iii
LIST OF TABLES	vii
LIST OF FIGURES	viii
SUMMARY	x
I INTRODUCTION	1
1.1 Historical background	1
1.2 Trapped atomic ions for quantum information processing	5
1.3 Cold molecules	7
1.4 Organization of this thesis	8
II ION TRAPPING, COOLING, AND HEATING	10
2.1 Linear rf ion traps and ion motion	10
2.1.1 Quadrupole potentials in a 3D linear ion trap	10
2.1.2 The Mathieu equations and trap stability	11
2.1.3 Secular motion and micromotion	13
2.2 Laser cooling and heating	17
2.2.1 Doppler cooling and heating	17
2.2.2 Resolved sideband cooling	23
2.2.3 Sympathetic cooling	25
2.2.4 Trap heating	26
2.3 Conclusion	26
III EXPERIMENTAL OVERVIEW	27

3.1	Sublimation and ionization of calcium	27
3.2	Laser systems and frequency stabilization	28
3.3	Experimental traps, vacuum systems and imaging systems	30
3.3.1	Atomic ion trap	30
3.3.2	Molecular ion trap	31
3.4	Conclusion	33
IV	SYMPATHETIC HEATING SPECTROSCOPY OF CALCIUM ISO-	
	TOPES	34
4.1	Introduction	34
4.2	Experiment	37
4.2.1	Experimental setup	37
4.2.2	Experimental procedure	37
4.2.3	Effect of laser powers on SHS	42
4.2.4	Effect of t_{heat} on SHS	44
4.3	Conclusion	48
V	SPECTROSCOPY ON THE $S_{1/2}$-$D_{5/2}$ OPTICAL QUBIT TRAN-	
	SITION	51
5.1	Introduction	51
5.2	Resolved sideband spectroscopy of Ca^+	52
5.2.1	Experimental	52
5.2.2	Zeeman effect on $S_{1/2}$ - $D_{5/2}$ transition	54
5.2.3	Sideband measurement, cooling and coherent dynamics	57
5.3	Resolved sideband mass spectrometry	61
5.3.1	Experimental	61

5.3.2	Resolved sideband mass spectrometry	62
5.4	Conclusion	68
VI	RESOURCE REQUIREMENTS FOR FAULT-TOLERANT QUANTUM SIMULATION: THE TRANSVERSE ISING MODEL GROUND STATE	70
6.1	Introduction	70
6.2	Transverse Ising model	72
6.3	TIM quantum simulation resource estimates	74
6.3.1	Phase estimation circuit	74
6.3.2	Decomposition of quantum circuit into fault-tolerant gates	76
6.3.3	Mapping onto the QLA architecture	80
6.3.4	Resource estimates for the 1-D TIM problem	83
6.3.5	Discussion of the resource estimates	85
6.4	Generalizing to higher spatial dimensions	87
6.5	Comparison with factoring	88
6.6	Conclusion	91
VII	CONCLUSION AND OUTLOOK	93
7.1	Future direction	94
	REFERENCES	97

LIST OF TABLES

1	Physical properties of ^{40}Ca	29
2	Isotopic abundances and transition shifts	29
3	Landé g factors for calcium	55
4	Comparison of secular frequencies for optical mass spectrometry . . .	66
5	Comparison of mass for optical mass spectrometry (no stray field) . .	66
6	Comparison of mass for optical mass spectrometry (stray field) . . .	68

LIST OF FIGURES

1	Linear Paul trap	12
2	Radial potential	13
3	Mathieu stability plot	14
4	Schematic of a two level system.	17
5	Schematic of Doppler cooling cycle	17
6	Schematic of a three level system	21
7	Λ system excited state population for Ca^+	22
8	Two scheme for sideband cooling	25
9	CCD image of calcium ions	28
10	Calcium energy diagram	28
11	Atomic trap and chamber	31
12	Molecular trap and chamber	32
13	Emission spectrum of the Ca^+	38
14	Procedure for sympathetic heating spectroscopy	39
15	Comparison of Doppler recooling fluorescence	41
16	Doppler recooling fluorescence trajectories	42
17	Average of the first 3 time bins for 20 Doppler recooling trajectories .	43
18	Effect of 397 nm laser powers on SHS	45
19	Effect of 866 nm laser powers on SHS	46
20	Effect of t_{heat} on SHS	47
21	Lower limit of SHS	49
22	Typical pulse sequence for spectroscopy of the $\text{S}_{1/2}$ - $\text{D}_{5/2}$ transition . .	54

23	Energy diagram of $^{40}\text{Ca}^+$ including Zeeman sublevels	55
24	Zeeman spectrum of $S_{1/2}$ - $D_{5/2}$	56
25	Spin polarization spectra of the $S_{1/2}^{m_j=-1/2}$ - $D_{5/2}^{m_j=-5/2}$ transition	57
26	Resolved sideband spectrum of $S_{1/2}^{m_j=-1/2}$ - $D_{5/2}^{m_j=-5/2}$	58
27	Laser frequency stability	59
28	Sideband cooling spectra	60
29	Rabi coherent dynamics	61
30	CCD image of calcium and calcium oxide ions	63
31	Broad sideband spectrum of two $^{40}\text{Ca}^+$	64
32	Red sideband spectra of the center-of-mass normal mode	65
33	Experimental secular frequency	67
34	Phase estimation algorithm circuit model	75
35	Circuit for the controlled unitary operation $U(2^m\tau)$	77
36	The decomposition of the controlled unitary operation $U_x(\theta)$	78
37	The decomposition of the controlled unitary operation $U_{zz}(2\theta)$	78
38	QLA architecture for the TIM problem	82
39	The number of logical cycles and days of computation	84
40	The total computation time in days	86
41	Performance characteristics of different QLA-based QC	89

SUMMARY

Laser-cooled atomic ions have led to an unprecedented amount of control over the quantum states of matter. The Coulombic interaction allows for information to be transferred between neighboring ions, and this interaction can be used to entangle qubits for logic operations in quantum information processors. The same procedure for logic operations can be used for high resolution atomic spectroscopy, and is the basis for the most accurate atomic optical clocks to date. This thesis describes how laser-cooled atomic ions can impact physical chemistry through the development of molecular ion spectroscopy techniques and the simulation of magnetic systems by ion trap quantum computers.

A new technique developed for spectroscopy, Sympathetic Heating Spectroscopy (SHS), takes advantage of the Coulombic interaction between two trapped ions: the control ion and a spectroscopy ion. SHS uses the back action of the interrogating laser to map spectroscopy ion information onto the Doppler shift of the control ion for measurement. SHS only requires Doppler cooling of the ions and fluorescence measurement and represents a simplification of quantum logic spectroscopy. This technique is demonstrated on two individual isotopes of calcium: $^{40}\text{Ca}^+$ for cooling and $^{44}\text{Ca}^+$ as the spectroscopy ion.

Having demonstrated SHS with atomic ions, the next step was to extend the technique by loading and characterizing molecular ions. The identification of an unknown molecular ion is necessary and can be achieved by monitoring the change in motion of the two ion crystal, which is dependent on the molecular ion mass. The motion of two trapped ions is described by their normal modes, which can be accurately measured by performing resolved sideband spectroscopy of the $S_{1/2}$ - $D_{5/2}$

transition of calcium. The resolved sidebands can be used to identify unknown ions (atomic and molecular) by calculating the mass based on the observed value in axial normal mode frequencies. Again, the trapped molecular ion is sympathetically cooled via the Coulombic interaction between the $^{40}\text{Ca}^+$ and the unknown molecular ion. The sensitivity of SHS could be improved by implementing sympathetic sideband cooling and determining the heating by measuring single quanta of motion.

The ultimate limit of control would be the development of an ion trap quantum computer. Many theoretical quantum computing researchers have made bold claims of the exponential improvement a quantum computer would have over a classical computer for the simulation of physical systems such as molecules. These claims are true in principle for ideal systems, but given non-ideal components it is necessary to consider the scaling due to error correction. An estimate of the resource requirements, the total number of physical qubits and computational time, required to compute the ground state energy of a 1-D quantum Transverse Ising Model (TIM) of N spin-1/2 particles, as a function of the system size and the numerical precision, is presented. This estimate is based on analyzing the impact of fault-tolerant quantum error correction in the context of the quantum logic array architecture. The results show that a significant amount of error correction is required to implement the TIM problem due to the exponential scaling of the computational time with the desired precision of the energy. Comparison of this result to the resource requirements for a fault-tolerant implementation of Shor's quantum factoring algorithm reveals that the required logical qubit reliability is similar for both the TIM problem and the factoring problem.

CHAPTER I

INTRODUCTION

The primary accomplishment of my graduate career was development of a new spectroscopy technique for both atomic and molecular ions. Spectroscopy is the study of the interaction of matter with light. To develop techniques which have high resolution and precision, it is necessary to have good control of the matter and light. Over the last few centuries, scientists have made substantial advances in the control of both light and matter. In this Chapter, we review the development of spectroscopy, the laser, and relevant applications. Sec. 1.1 focuses on the historical background of spectroscopy, the laser, and laser cooling. In Sec. 1.2, the use of laser cooled atomic ions in quantum information processing and in the construction of highly accurate atomic clocks is discussed. Finally, Sec. 1.3 concludes with a review of cold molecules and discusses the application of quantum information processing techniques to high precision spectroscopy.

1.1 Historical background

In the 17th century, only broadband light sources such as fire and the sun were available. In 1666, I. Newton showed that sunlight could be dispersed into a continuous array of colors [1], the first step in showing that light could be controlled. Using a small pinhole and a lens he was able to collimate the sunlight through a prism causing the light to disperse into the visible light spectrum [1]. In the 1880's, J. Fraunhofer showed that monochromatic light could be selected from a broadband light source with the invention of the diffraction grating [1]. It was because of this ability to select monochromatic light that G. Kirchhoff was able to perform experiments showing

that each element and chemical compound had a unique absorption spectrum when interacting with light [1]. His studies demonstrated that a spectrum of an unknown compound would yield the composition of the compound and represent the birth of spectroscopy as a discipline [1].

By the late 19th century, the study of atomic spectral lines was a robust discipline. In 1885, J. J. Balmer, a mathematician by training, showed the spectral line of atomic hydrogen could be represented by a simple mathematical formula, now known as the Balmer series [1, 2]. It was later determined that his formula was a specific case of the Rydberg-Ritz combination principle, which gave a more natural expression for the spectral lines. J. R. Rydberg empirically determined the general formula, which related the frequencies of spectral lines to the sum difference between two quantities. He found the emission frequencies could be determined by a single, universal constant known as the Rydberg constant [1, 2]. N. Bohr's quantum theory of hydrogen described J. J. Balmer and J. R. Rydberg's results [1, 2] and suggested that light is emitted when an electron makes a transition from a higher energy state to a lower one. Further, he claimed the "lost" energy was carried away by a photon. This work was a revolutionary step in spectroscopy and the insight needed for E. Schrodinger and W. Heisenberg to develop modern quantum mechanics [1, 2]. Using the new developments in spectroscopy, W. Pauli determined in 1925 that no two electrons in an atom have the same quantum numbers; now famously known as the Pauli Exclusion Principle [1, 2].

For years, advances in spectroscopy were made using spectral lamps, but now most modern spectroscopy techniques use lasers. A laser allows for intense, phase coherent, collimated monochromatic radiation to be provided throughout the optical spectral range [1, 2, 3]. The advent of lasers immediately stimulated new interest in atomic and molecular spectroscopy leading to high resolution spectroscopy. The important theoretical milestone in the development of the laser was the introduction

of the concept of spontaneous and stimulated emission by A. Einstein in 1916 [4, 5]. Einstein was able to combine classical and quantum theories with Bohr's spectral theory and introduced stimulated emission [5]. Within a few years, theoretical physicists were able to build a quantum theory that describes scattering, refraction, and light dispersion [5].

The underlying principle of a laser is stimulated emission of electromagnetic (EM) radiation in a medium of atoms, molecules, or other material. A laser requires a lasing medium that undergoes a population inversion. This means more particles in the lasing medium are in an excited state than are in the ground state. Population inversion in working devices was first demonstrated in the microwave region of the EM spectrum where spontaneous emission probabilities are negligible [5]. In 1955, Microwave Amplification by Stimulated Emission of Radiation (MASER) was experimentally demonstrated by C. H. Townes [5, 6], for which he was awarded the Nobel prize in 1964 with N. G. Basov and A. M. Prokhorov. The development of the MASER prompted many researchers to pursue an optical maser, which is now known as a laser. It was another five years (July 1960) before the laser was implemented at Hughes Research Laboratories by T. H. Mainman, with ruby as the active material [5, 7]. Later in 1960, the He-Ne gaseous laser was developed at Bell Laboratories by A. Javan and W. R. Bennet Jr. [8, 5]. Ever since the development of the first lasers, researchers have been interested in new lasing materials. Other types of lasers include: ion lasers (1963 [9]), molecular lasers (CO_2 , 1963 [10, 11, 12]), excimer lasers (1970 [13], 1972 [14]), liquid dye lasers (1967 [15, 16, 17]), and semiconductor lasers (1962 [18, 19]). Over the last half century many advances in laser technology have led to scientific discoveries across many disciplines, specifically in atomic and molecular physics.

If the state of matter is not well controlled, it is assumed that the system is in a thermal state. In gas samples this inhomogeneity leads to Doppler broadening

of spectral lines and measurement uncertainty. With advances in laser technology, we can now use lasers to cool atoms and molecules. This increased control of light has led to better control of matter. In 1975, D. Wineland and R. Dehmelt [20], and simultaneously T. Hänsch and A. Schawlow [21], proposed the use of a laser to exert a radiative pressure on an atom by tuning the laser frequency red of the atomic resonance thus removing energy from the external motion of the atom on emission of a photon. The 1997 Nobel prize was awarded to S. Chu, W. Phillips, and C. Cohen-Tannoudji for advances made in laser cooling techniques. Currently, laser cooling of atoms is used by many research groups to cool the atom's motion close to absolute zero. The 2001 Nobel prize was awarded to E. Cornell, C. Wieman, and W. Ketterle for the demonstration of Bose-Einstein Condensation, which requires initial laser cooling of neutral atoms followed by evaporative cooling to demonstrate this new state of matter.

One might wonder why laser cooling atoms has garnered such an interest in the scientific community. Clearly, the laser is a useful tool to study atoms and molecules. If these species are in the gas phase at room temperature, then their thermal velocity is ≈ 300 m/s. At this high speed, accurate measurements are very difficult because the laser-atom interaction time is very small leading to lower resolution [22]. Additionally, the spectral measurements are Doppler broadened and shifted [22]. One method to improve gas phase spectra is to use a refrigerant such as liquid nitrogen (77 K) or helium (4 K) to slow down the gas to ≈ 150 m/s or ≈ 90 m/s respectively [22]. To slow the thermal velocity to 1 m/s would result in a gas at equilibrium to condense leaving no particle in the gas phase [22]. With the advent of laser cooling, thermal velocities below 1 m/s could be achieved for certain gas phase species leading to interesting scientific applications including higher resolution spectra [22].

Since the 17th century, many advances in controlling light and matter have given scientist the ability to develop applications which rely on spectroscopic information.

The use of laser cooled atoms has led to applications in quantum computation using neutral and ionic species [23, 24], quantum logic gates [25, 26, 27], quantum teleportation [28, 29], and quantum memories [30]. Another important advancement is the testing of fundamental physical constants (e. g., the fine structure constant [31, 32, 33]). Laser cooling atomic species allows high resolution spectroscopy to be performed [24, 34, 35, 36, 37], which has resulted in more accurate atomic optical clocks [38, 39, 40, 41, 33, 42].

The use of laser cooled atoms has also led to advancements in molecular physics by using the atomic species to sympathetically cool the molecules or by reacting ultracold atoms to form ultracold molecules. Scientists have started to investigate if reactions proceed differently at the single molecule level [43, 44], considered the effects of cold reactants by combining ion traps with quadrupole velocity guides [43], performed fundamental high resolution spectroscopy of molecules [43, 45, 46, 47, 48, 44, 49, 50, 51, 52, 53], compared differences in the mass of the electron to the mass of the proton [33, 54], more recently investigated laser cooling rotational and vibrational degrees of freedom [55, 56], and even explored molecular species for direct laser cooling [57, 58, 59]. All of these research areas are a direct result of advances in spectroscopy.

1.2 Trapped atomic ions for quantum information processing

This section focuses on some of the fundamental work related to laser-cooled trapped atomic ions and their practical applications to Quantum Information Processing (QIP). In 1994, P. Shor introduced a new quantum algorithm to factor numbers more efficiently [60], resulting in increased interest in quantum information science. A year later (1995), I. Cirac and P. Zoller proposed a scheme for using trapped atomic ions as computational elements in a quantum computer [61]. In their scheme, two

ions in a common potential well are entangled using their mutual Coulombic interaction [61]. Later in 1995, quantum logic operations were first demonstrated [62] with the development of sideband cooling but the proposed Cirac-Zoller gate was not completely implemented until 2003 [63].

Many researchers have decided to follow R. Feynman's insight from 1982 to use one quantum system to simulate the dynamics of another quantum system [64]. One prime candidate for quantum simulation is trapped atomic ions, although many other systems have been proposed for a quantum simulator [65]. Quantum simulation with trapped ions has been applied to problems in condensed matter physics. C. Monroe's group simulated the quantum phase transition of a 1D transverse Ising model using a string of trapped ions by varying the strength of the spin-spin and magnetic field interaction [66], and they have started to simulate effects of spin frustration [67]. Quantum simulators may also be used to investigate relativity. R. Blatt's group has performed a quantum simulation of the Dirac equation [68], the Klein Paradox [69], and relativistic quantum mechanics [70]. These quantum simulations are milestones which have arisen on the path to using trapped atomic ions to make a large scale quantum processor.

Although ion traps have been used for QIP for over 16 years, other applications have emerged from the field. One such application takes advantage of entangled states to improve the sensitivity of spectroscopy [24, 34, 35, 36, 37]. It has also been shown that spectroscopic information for species that do not have cycling transitions, or have transitions at inconvenient wavelengths, can be studied by coupling the spectroscopic information onto a species that can be measured. It was shown that using a Cirac-Zoller type approach that spectroscopic information of $^{27}\text{Al}^+$ can be measured via a $^9\text{Be}^+$ ion [38, 39]. This technique, known as Quantum Logic Spectroscopy (QLS), was one of the motivations for the advances reported in this thesis. This optical transition

in $^{27}\text{Al}^+$ is now used for a very accurate optical clock [42] and comparison to a Hg^+ optical clock results in an uncertainty of a few parts in 10^{17} [39, 71].

1.3 Cold molecules

Physical chemists began studying cold molecules using supersonic free-jet molecular beams [72] in the 1980's. This method provides a way for a variety of molecules to be produced with cold translational temperatures on the order of 1 K in the beam frame [72, 73, 74]. As a result of the collisions that occur in the expansion of the beam, the internal degrees of the molecule relax towards the translational temperature [73], especially for the rotational degrees of freedom which equilibrate quickly [73]. Because the vibrational temperature equilibrates more slowly, the supersonic molecular beam also results in substantial vibrational cooling upon expansion [72]. Using supersonic crossed molecular beams creates an ideal environment to study dynamics of reactions, giving access to quantum mechanical effects [75]. Although molecular beams create a platform for dynamic studies of cold chemical reactivity, they lack the robustness to perform repeated measurements of single molecules, which are of interest for metrology studies.

In the mid 1990's, chemical physicists became interested in cold molecular gases due to the many advances in atomic physics that resulted from studying cold atoms [76]. Because molecules have intriguing properties, researchers have proposed possible advances in QIP [46, 77] or even in quantum degenerate dipolar systems [76, 46, 77]. Some envision using cold molecules to test fundamental physics such as time-reversal symmetry, parity [76, 46, 77] and the Pauli principle [46, 77]. Performing high resolution spectroscopy of cold molecules is also important to astrophysical observations, such as possible space-time variations of fundamental constants [33, 54, 76, 46, 77]. There are two main methods for producing cold molecules (<1 K). The first is an indirect method which involves using ultracold (<1 mK) atoms to produce molecules

by decelerating a supersonic molecular beam [76, 46, 77], or selecting slower molecules of an ensemble [76, 46, 77]. Molecules produced via a direct method can be cooled further through sympathetic cooling with a cold atomic buffer gas [76, 46, 77], or in the case of trapped molecules, laser cooled atoms [76, 46, 77].

It has been demonstrated that molecular ions can be loaded in ion traps and sympathetically cooled to milikelvin temperatures using atomic ions as a refrigerant [78, 79, 80, 81]. Even molecules as large as Alexa Flour 350 and some biomolecules can be trapped and cooled [80, 82]. Rotational and vibration spectroscopy can be performed using large Coulomb crystals in a destructive manner [83, 84, 85, 86], and this thesis presents a series of experiments resulting in a non-destructive spectroscopy technique for single, sympathetically cooled, trapped molecular ions. Some research groups have also started to look at reaction rates of ultracold molecules [43, 51, 87, 88]. If the de Broglie wavelength is long compared to the molecular dimensions (range of interaction) then wave effects dominate the collisional behavior. At low temperatures in a thermal distribution, few internal quantum states are populated and these collisional dynamics in the quantum regime have yet to be studied extensively. Physical chemist, T. Softley, and two physicists, M. Drewson and S. Schiller, have demonstrated the first proof of concept experiments using ion traps to investigate cold reaction [43, 51, 87, 88]. For a review of the emerging field of cold molecules see Ref. [76].

1.4 Organization of this thesis

The remainder of this thesis is divided into six chapters. Chapter 2 provides an introduction to the theory and operation of linear Paul ion traps and laser cooling techniques. Chapter 3 provides an overview of the calcium ion trapping experiment. Chapter 4 discusses a new spectroscopy technique termed Sympathetic Heating Spectroscopy (SHS). SHS uses a two-step process in which we heat a two ion Coulombic

crystal via the spectroscopy ion and then obtain spectroscopic information by observing changes in fluorescence of the control ion as the system is recooled. Chapter 5 discusses results of resolved sideband measurements and ground state cooling of both atomic Ca^+ and molecular ions. These measurements are used to accurately measure molecular ion masses by optical detection. Chapter 6 changes direction and discusses a theoretical result regarding the resource requirements for fault tolerant quantum simulation of the 1-D Ising model. The thesis concludes with Chapter 7, which summarizes the results presented and provides an outlook for future experiments.

CHAPTER II

ION TRAPPING, COOLING, AND HEATING

Ion trap technology has been used for years to study atomic and molecular ions, in both mass spectrometry and atomic and molecular physics [89]. In the few decades, ion trap quantum processors have attracted attention [90]. The included work has used ion traps to study atomic and molecular ions using similar protocols as those used for ion trap quantum computing. In this chapter, the fundamental formulas describing ion trapping are derived and the basic concepts of laser cooling and heating are presented. A complete, detailed description of ion traps can be found in Ref. [89] and laser cooling in Ref. [91].

2.1 Linear rf ion traps and ion motion

2.1.1 Quadrupole potentials in a 3D linear ion trap

In this work quadrupole ions traps are used, and the quadrupole electric scalar potential (ϕ) in three dimensions is given by

$$\phi(t) = \frac{\phi_0}{2r_0^2}(\lambda x^2 + \sigma y^2 + \gamma z^2), \quad (1)$$

where ϕ_0 is the externally applied potential, and λ, σ, γ are geometric constants which depend on the spatial boundary conditions [89]. From Laplace's equation, the geometric constants must satisfy

$$\nabla^2\left(\frac{\phi_0}{2r_0^2}(\lambda x^2 + \sigma y^2 + \gamma z^2)\right) = 0, \quad (2)$$

requiring $(\lambda + \sigma + \gamma) = 0$, which implies at least one component of the potential must be repulsive [89]. Therefore, to successfully confine a charged particle the applied fields cannot be static in time. A basic example of a quadrupole linear ion trap is shown in Figure 1 in which a radio-frequency (rf) field is applied to opposite rods to confine an ion in the radial (x,y) direction. Considering only the radial components the potential may be written as

$$\phi_{x,y} = \frac{\phi_0}{2r_0^2}(\lambda x^2 + \sigma y^2). \quad (3)$$

Satisfying Laplace's equation leads to a potential which is attractive in one direction (x) and repulsive in the other (y), thus creating a saddle potential (Figure 2) [89]. The radial confining potential with the addition of a DC bias, U_x , is

$$\phi_{x,y}(t) = \frac{1}{2}(U_x + V_0 \cos(\Omega_T t))(1 + \frac{x^2 - y^2}{r_0^2}), \quad (4)$$

where V_0 is the amplitude of the rf potential, and r_0 is the distance from the center of the trap to the rods [89]. The ion is confined in the axial (z) direction by applying a DC potential, U_0 , to the electrodes known as the endcaps (Figure 1).

This introduces the basic physics of the electric trapping potential, in the next section we use Equation 4 to describe the motion of the confined charge particle.

2.1.2 The Mathieu equations and trap stability

Given the electric trapping potential (Equation 4), the classical equations of motion of a charged particle of mass m and charge e are given by the set of differential equations

$$\frac{d^2x}{dt^2} + \frac{e}{mr_0^2}(U_x + V_0 \cos(\Omega_T t))x = 0 \quad (5)$$

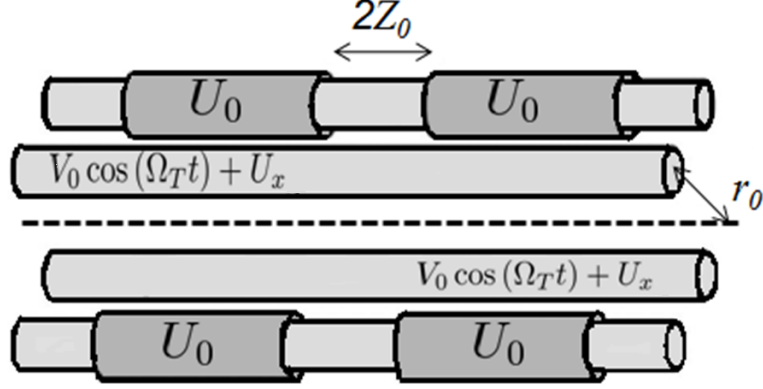


Figure 1: Schematic of the linear Paul trap. Two opposing rods provide a potential $V = U_x + V_0 \cos(\Omega_T t)$, where V_0 is the amplitude of the rf voltage and U_x is a DC bias. The other pair of rods are held at ground or an additional DC bias can be applied for compensation purposes which will be discussed later [92].

$$\frac{d^2 y}{dt^2} - \frac{e}{mr_0^2}(U_x + V_0 \cos(\Omega_T t))y = 0 \quad (6)$$

$$\frac{d^2 z}{dt^2} = 0 \quad (7)$$

and are simplified by substituting

$$a = \frac{4eU_x}{mr_0^2\Omega_T^2}; \quad q = \frac{2eV_0}{mr_0^2\Omega_T^2}, \quad 2\zeta = \Omega_T t \quad (8)$$

to obtain the Mathieu equations. The Mathieu equations are

$$\frac{d^2 x}{d\zeta^2} + (a - 2q \cos(2\zeta))x = 0 \quad (9)$$

$$\frac{d^2 y}{d\zeta^2} - (a + 2q \cos(2\zeta))y = 0. \quad (10)$$

These equations can be solved using Floquet theory [94], and result in stable ion trajectories for only certain ranges of a and q . Figure 3 shows a plot of the primary

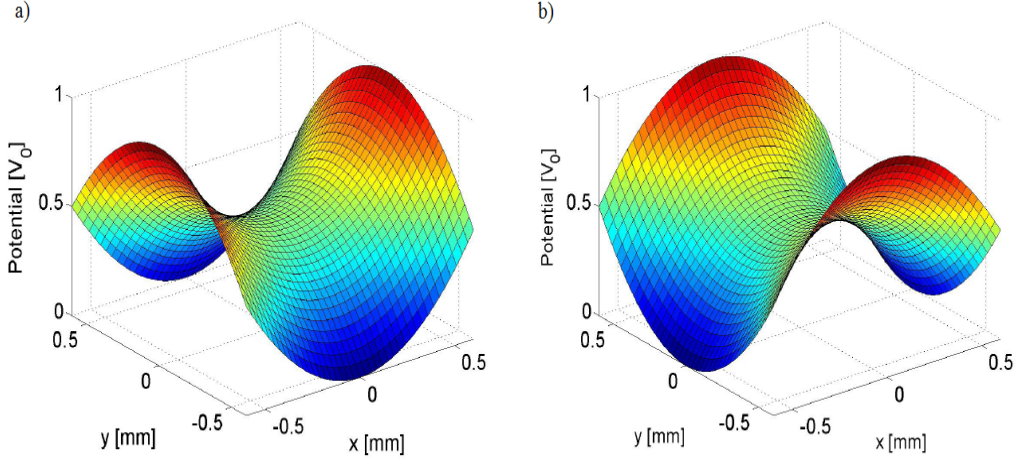


Figure 2: The radial potential at two points in time, with $U_x = 0$. (a) The potential is attractive in x and repulsive in y , at $t = 0$. (b) The situation has reversed, and the potential is now attractive in y , after half a period [93].

stability region. The ion is stable in the region labeled xy-stable [93]. If it is assumed that the DC bias $U_x = 0$ then $a = 0$, which gives an upper limit within the primary stability region on the value of q of 0.908. Typically the trap parameters are set such that q is between 0 and 0.908. For trapping Ca^+ , we set our trap parameters such that $q \approx 0.4$, which makes it possible to trap a range of masses (13-200 amu for singly charged ions) without changing the trap parameters.

2.1.3 Secular motion and micromotion

Now that we have derived a set of parameters (a and q) which are useful for determining appropriate fields to trap charged particles, it is possible to investigate the ion motion. A trapped ion undergoes two types of movements: fast micromotion and slow, harmonic secular oscillations. Micromotion results from the fast oscillation of the rf field. At the null of the rf field the micromotion vanishes [92]. For an ideal linear Paul trap, the rf null overlaps the trap minimum, but due to imperfections in trap construction and stray charges this is not always the case. Therefore a set of compensation electrodes are used to apply DC voltages to minimize micromotion

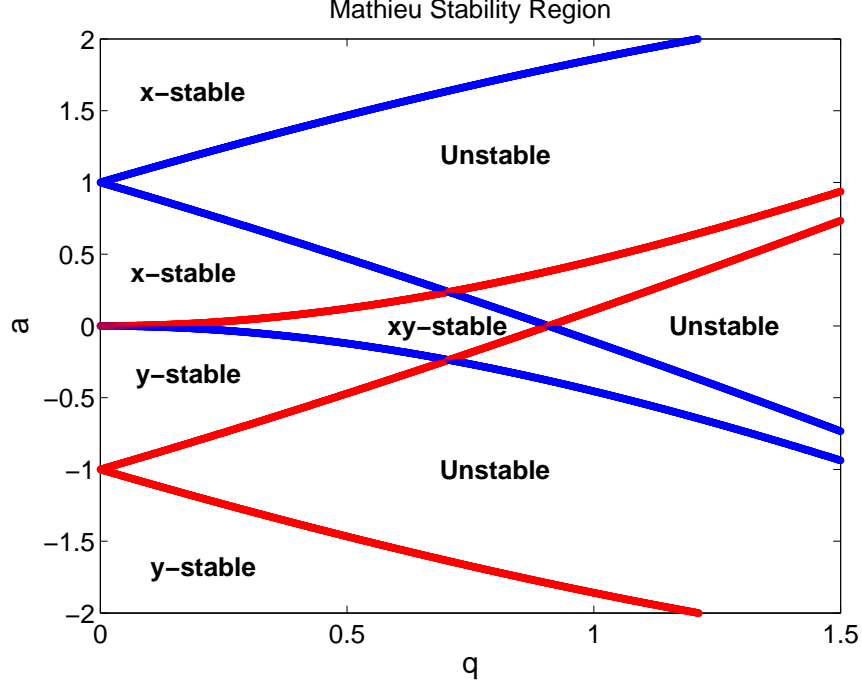


Figure 3: Mathieu stability regions in the a - q plane. Stability region along x (blue) or y (red) and in both dimensions labeled xy -stable.

in non-ideal traps. For small micromotion displacements, the micromotion can be detected by the correlation between the ion fluorescence and the rf drive [92]. In contrast, the secular motion is harmonic within the pseudopotential well, and the secular frequency can be calculated from the trap parameters [92].

To detail these motions, we separate the ion's movement into two components: the fast micromotion, and the slow secular motion. For clarity we only consider one radial dimension and decompose the ion's coordinates as $x = X_s + x_\mu$, where X_s is the amplitude of the secular motion and x_μ is the amplitude of the micromotion in the x -dimension [88, 89, 93]. Assuming

$$X_s \gg x_\mu \quad \text{and} \quad \frac{dx_\mu}{dt} \gg \frac{dX_s}{dt} \quad (11)$$

and substituting x into the equation of motion (Equation 9), we arrive at

$$\frac{d^2 x_\mu}{d\zeta^2} = -(a - 2q \cos(2\zeta))X_s. \quad (12)$$

If X_s does not vary over a single rf cycle and $a \approx 0$, which is normally the case, then integrating the previous equation gives

$$x_\mu = \frac{qX_s}{2} \cos(2\zeta). \quad (13)$$

The micromotion is driven at the fundamental frequency ($2\zeta = \Omega_T$) of the trap, its amplitude is linearly dependent on the secular amplitude, and it is proportional to the rf amplitude through the q parameter. It should be noted that the micromotion over a single rf cycle integrates to zero [88, 89, 93]. Equation 13 can be substituted in $x = X_s + x_\mu$, giving a new expression for x to be used in Equation 9. We can simplify further by assuming that the secular amplitude varies little over a single rf cycle, which eliminates the micromotion and the cosine terms to obtain [93, 89, 88]

$$\frac{d^2 X_s}{dt^2} = -(a + \frac{q^2}{2})\frac{\Omega_T^2}{4}X_s. \quad (14)$$

This equation is exactly the equation of motion for a harmonic oscillator with frequency

$$\omega_x = (a + \frac{q^2}{2})^{1/2}\frac{\Omega_T}{2}. \quad (15)$$

Now that we have determined that the secular motion is that of a harmonic oscillator, the trap potential can be approximated in terms of a two dimensional harmonic oscillator as [93, 89, 88]

$$\phi_{pseudo}(\mathbf{r}) = \frac{1}{2}m\omega_x^2 x^2 + \frac{1}{2}m\omega_y^2 y^2. \quad (16)$$

This effective potential is referred to as the pseudopotential. If we now assume that $a = 0$, and substituting the trap radius r_0 for the appropriate spatial coordinates, we can obtain a term for the maximum trap depth of

$$\phi_{pseudo}(r_0) = \frac{eV_0^2}{mr_0^2\Omega_T^2}. \quad (17)$$

Normal quadrupole trap depths are on the order of several eV.

The previous discussion has only considered the radial motion of the ion in the x and y dimensions, but there is also motion in the z dimension. Axial confinement is achieved in a linear Paul trap by applying DC voltages to a set of endcaps (labeled by U_0) as shown in Figure 1. The axial confinement potential can also be approximated as a harmonic potential and is written as

$$\phi_{axial}(z) = \frac{1}{2}m\omega_z^2 z^2, \quad (18)$$

which leads to an axial secular frequency of

$$\omega_z = \sqrt{2a_z} \frac{\Omega_T}{2}, \quad (19)$$

with

$$a_z = \frac{4Z_0 e \kappa U_0}{mr_0^2 \Omega_T^2} \quad (20)$$

where U_0 is the voltage applied to the endcaps, κ is a constant which depends on the trap geometry, and Z_0 is the distance between endcaps [92, 89]. It is now possible to determine the secular frequencies and amplitude of the micromotions from the applied trap voltages.

Using these arguments, we have derived formulas based on the Mathieu stability parameters to describe the fundamental frequency of a trapped charge particle by

separating the variables in terms of the fast and slow motion. The ions are effectively in a three dimensional harmonic potential.

2.2 *Laser cooling and heating*

2.2.1 Doppler cooling and heating

2.2.1.1 *Two level atom*

Once the ion is confined in the trap, excess translational energy is removed by using laser cooling techniques; the basis for this technique arises from a velocity-dependent radiative pressure exerted by the laser on the atom or ion. One laser cooling method is Doppler cooling, and it is easiest to describe in terms of a two level system with the level structure shown in Figure 4 [91]. With this method, ion temperatures in the mK regime can be readily obtained; a schematic of the Doppler cooling process is shown in Figure 5.

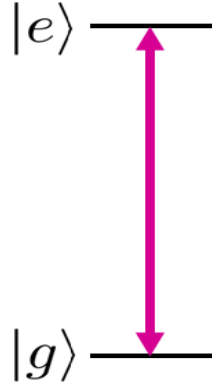


Figure 4: Schematic of a two level system.

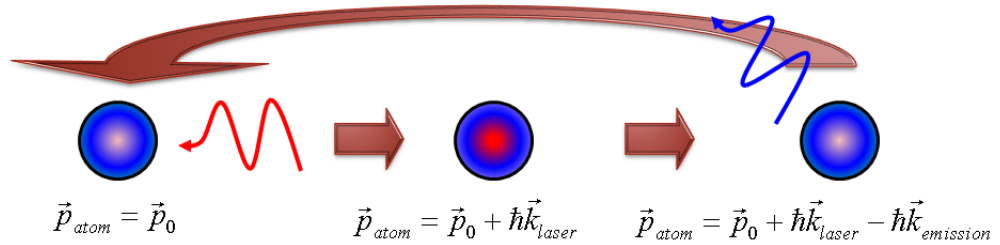


Figure 5: Schematic of Doppler cooling cycle. See text for a description

An atom interacting with a near resonant laser (red detuned) with wavevector \vec{k} results in a momentum kick of $\hbar\vec{k}$ in the direction of the laser beam for each photon that is absorbed [91, 95]. The photon is absorbed due to the Doppler shift associated with the counter propagating motion of the atom with respect to the direction of the wave vector of the laser. If each spontaneously emitted photon is emitted in a random direction, when averaging over many absorption-emission cycles the net force will only be in the direction of the laser beam. The radiative force is defined by the momentum change per photon scattered, $\hbar\vec{k}$, times the scattering rate [91]

$$F = \hbar\vec{k}\gamma\rho_{ee}, \quad (21)$$

with γ equal to the natural linewidth of the atomic transition, and ρ_{ee} equal to the excited state population given by

$$\rho_{ee} = \frac{s/2}{1 + s + (2\delta/\gamma)^2}. \quad (22)$$

Here δ is the detuning of the laser from the atomic resonance and s is the saturation parameter defined as [91]

$$s = \frac{I}{I_0}, \quad (23)$$

where I_0 is the saturation intensity given by

$$I_0 = \frac{\pi\hbar c}{2\lambda^3\tau}, \quad (24)$$

and $\tau = \gamma^{-1}$. The Rabi frequency is also defined in terms of the saturation intensity as [91]

$$\Omega_{Rabi} = \gamma\sqrt{\frac{I}{2I_0}}. \quad (25)$$

The intensity of the laser is the easiest parameter to measure in most experiments, and can be used as a variable to control the Rabi frequency.

The radiative force slows the atom down as long as the atom's velocity is opposite the laser's direction of propagation. As the ion's velocity changes so will the excited state population through the detuning parameter. The atomic transition is Doppler shifted by the atom's velocity by an amount [91]

$$\delta_{Doppler} = \vec{k} \cdot \vec{v}. \quad (26)$$

The above case describes laser cooling of a free atom. When dealing with a trapped atomic ion the process is slightly different because the direction the ion moves depends on the rf cycle. A bound ion oscillates harmonically with the trap which leads to a sinusoidally time dependent velocity. If a resonant laser is directed at the trapped ion, the ion will experience a force in the direction of the laser that will result in heating for half of the trap cycle and cooling the other half. Therefore it is important to ensure that the cooling for a cycle is greater than the heating. This is achieved by tuning the laser frequency below the atomic resonance for the atom at rest [95]. The detuning of the laser with respect to the true atomic resonance is

$$\delta = \delta_0 + \delta_{Doppler}, \quad (27)$$

where δ_0 is the laser detuning and $\delta_{Doppler}$ is the detuning of the atomic resonance due to the Doppler shift. As the ion oscillates in the trap the detuning δ , and ρ_{ee} , will oscillate, and by setting $\delta_0 < 0$ this will ensure that δ is closer to 0 as the ion moves opposite \vec{k} . During the half cycle that the ion moves opposite \vec{k} there is a small detuning, which results in more scattered photons and leads to cooling [95].

The lowest temperature that can be achieved by Doppler cooling is the Doppler limit,

$$k_B T_D = \frac{\hbar \gamma}{2}, \quad (28)$$

where k_B is Boltzmann's constant and T_D is the temperature limit for Doppler cooling [91, 95]. In Ca^+ , the $S_{1/2} - P_{1/2}$ cooling transition at 397 nm has a natural linewidth $\gamma = 2\pi \times 22$ MHz, which results in $T_D = 570$ μK .

It should be noted, and is important later in this document, that if the laser is tuned to the blue of the atomic resonance the ion will be heated, because $\delta_0 > 0$ results in δ (Equation 27) being closer to 0 as the ion moves with \vec{k} . As the ion moves with \vec{k} during half of the rf cycle, this results in Doppler heating which dominates the process.

2.2.1.2 Three level atom

The description above is the simplest way to consider Doppler cooling. When dealing with most atomic systems there are also metastable states which require additional repumper lasers to maintain the closed cooling cycle. In this work, the laser cooled ion is Ca^+ , which has an excited state that is linked to both the ground state and a metastable state as shown in Figure 6. This level configuration is known as a Λ -system. The addition of the metastable state affects the maximum likelihood the atom will be in the excited state. This is due to the branching ratio of the decay from the excited state to the ground and metastable states [95, 96]. For Ca^+ , the branching ratio is 18:1 for the decay to $S_{1/2}:D_{3/2}$ from $P_{1/2}$ [97].

One common issue to avoid in a Λ -system is coherent population trapping. Coherent population trapping occurs when two laser fields coherently couple to a common excited state creating a dark resonance [95, 96]. When trapped in the dark state, the

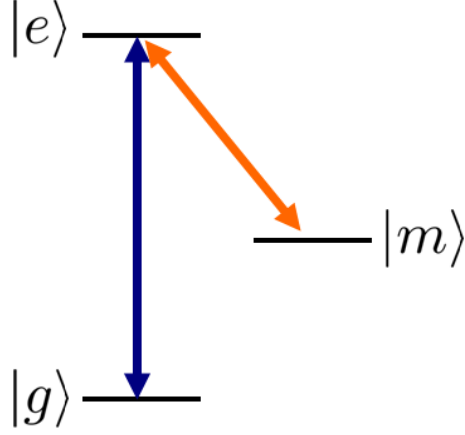


Figure 6: Schematic of a three level system. $|g\rangle$ is the ground state, $|e\rangle$ the excited state and $|m\rangle$ is the metastable state

ion's excited state population, ρ_{ee} , is zero. Since the radiative force and the cooling rate depend on the excited state population, coherent population trapping must be avoided in order to efficiently Doppler cool a three level atom. By detuning the repumper laser blue of the atomic resonance, coherent population trapping can be avoided. A detailed description of coherent population trapping can be found in Ref. [96].

Now that there is a metastable state which couples to the excited states, Equation 22 no longer describes the excited state population. If the two applied lasers are denoted e and m , which represent transition from the ground to excited state and metastable to excited states, respectively, then ρ_{ee} as a function of detunings δ_e and δ_m , Rabi frequencies (as in Equation 25) Ω_e and Ω_m , and linewidths γ_e and γ_m is [96]

$$\rho_{ee} = \frac{N}{D} \quad (29)$$

$$N = 4\Omega_e^2\Omega_m^2(\gamma_e + \gamma_m)(\delta_e - \delta_m)^2 \quad (30)$$

$$\begin{aligned} D = & (\delta_e - \delta_m)^2 \{ 8\Omega_e^2\Omega_m^2(\gamma_e + \gamma_m) + 16\Omega_e\gamma_m[(\gamma_e + \gamma_m)^2 + \delta_m^2] \\ & + 16\Omega_m\gamma_e[(\gamma_m + \gamma_e)^2 + \delta_e^2] \} + 8(\delta_e - \delta_m)(\Omega_e^4\delta_m\gamma_m - \Omega_m^4\delta_e\gamma_e) \\ & + (\Omega_e^2\gamma_m + \Omega_m^2\gamma_e)(\Omega_e^2 + \Omega_m^2)^2. \end{aligned} \quad (31)$$

Equation 29 is the excited steady state population for a Λ -system and Eqs. 30 and 32 show that as $\delta_e \rightarrow \delta_m$ then $N \rightarrow 0$ and $D \rightarrow 0$, resulting in an excited state population of zero. Figure 7 is an example of the excited state population of Ca^+ as the detuning of the two lasers are varied with the saturations held constant at $s_e=10$ and $s_m=1000$, which are common saturations used in our experiments.

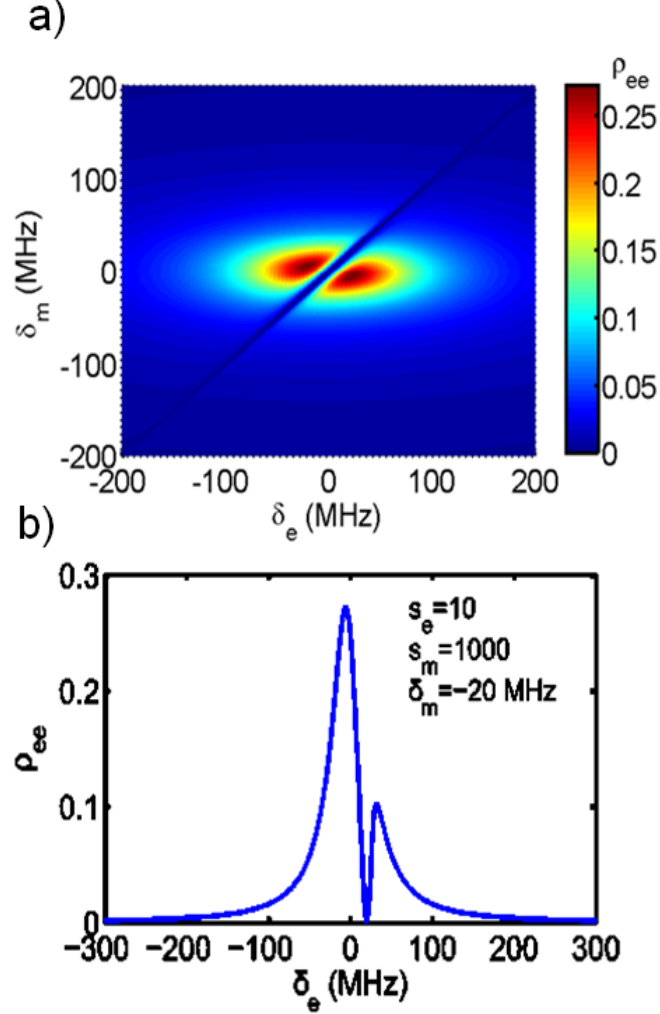


Figure 7: (a) The excited state population as the detuning of two Ca^+ lasers are varied with $s_e=10$ and $s_m=1000$. The coherent population trapping occurs when $\delta_e = \delta_m$. (b) The excited state population varying δ_e with $\delta_m = -20$ MHz, which is common for most experiments in this thesis.

It should be noted that for a two level system the maximum excited steady state population is $\frac{1}{2}$ as the saturation is increased however for a three level system the maximum excited population is $\frac{1}{3}$. This leads to a lower fluorescence signal than for a two level system. Also, with the application of a \vec{B} field the energy levels experience a Zeeman shift. In this case a more accurate description of the excited state population requires the optical Bloch equation for all eight sub-levels to be solved [98]. In this work the three level approximation is sufficient.

2.2.2 Resolved sideband cooling

While discussing Doppler cooling we determined a lower temperature limit known as the Doppler limit, T_D . Earlier in this chapter we also determined that the trapped ion effectively behaves as a harmonic oscillator. Therefore, by combining these concepts, it is possible to determine the average number of quanta a trapped ion has after Doppler cooling. Using an energy argument, the average occupation number $\langle n \rangle$ of the trapped ion can be determined as follows [99, 100, 62]

$$k_b T_D = \hbar \omega (\langle n \rangle + \frac{1}{2}). \quad (32)$$

For example, for a trapped Ca^+ , T_D is $570 \mu\text{K}$ and a common radial secular frequency is 1.2 MHz , which results in $\langle n \rangle = 8$ after Doppler cooling. From this equation we see that even after reaching the Doppler cooling limit the ion still has many quanta of energy. Therefore, to cool the ion to the ground harmonic state, a second stage of laser cooling must be performed, which is known as resolved sideband cooling or ground state cooling.

The Lamb-Dicke parameter, η , relates the spatial extent of the lowest harmonic oscillator state to the wavelength of the atomic transition,

$$\eta = \frac{2\pi}{\lambda} x_0 = \frac{2\pi}{\lambda} \sqrt{\frac{\hbar}{2m\omega_{sec}}}. \quad (33)$$

In the Lamb-Dicke regime, defined by the condition $\eta^2 \langle n \rangle \ll 1$, the atomic wavepacket is confined to a space much smaller than the wavelength of the transition. It should be stated that the Lamb-Dicke regime is always defined with respect to the wavelength of the transition involved [99, 100].

Sideband cooling on an atomic transition requires the trap frequency to be larger than the laser linewidth ($\omega \gg \gamma_{laser}$), and the excited state to have a long decay rate allowing the laser to be tuned to the lower (red, $\Delta n = -1$) motional sideband of the transition. Pulsing the laser on the lower motional sideband leads to the reduction of one quanta with each excitation to the upper level. If spontaneous decay occurs, it will most likely not affect the motional state as long as the Lamb-Dicke criteria holds [99, 100].

Figure 8 shows two schemes for sideband cooling. The first shows excitation to an upper state lowers the number of quanta by one, and the second scheme shows that the lifetime of the upper state may be shortened by coupling it to an auxiliary level that has a fast decay rate [99, 100]. For our sideband cooling experiments with Ca^+ , the second scheme is used. We first excite the quadrupole $S_{1/2} - D_{5/2}$ transition and then drive the dipole $D_{5/2} - P_{3/2}$ transition to take advantage of the fast decay rate of the $P_{3/2} - S_{1/2}$ transition.

Assuming the atom has been sufficiently cooled the average number of quanta can be obtained by comparing the ratio of the red and blue sideband amplitudes as in Ref. [101]

$$\langle n \rangle = \frac{A_{red}}{A_{blue} - A_{red}}. \quad (34)$$

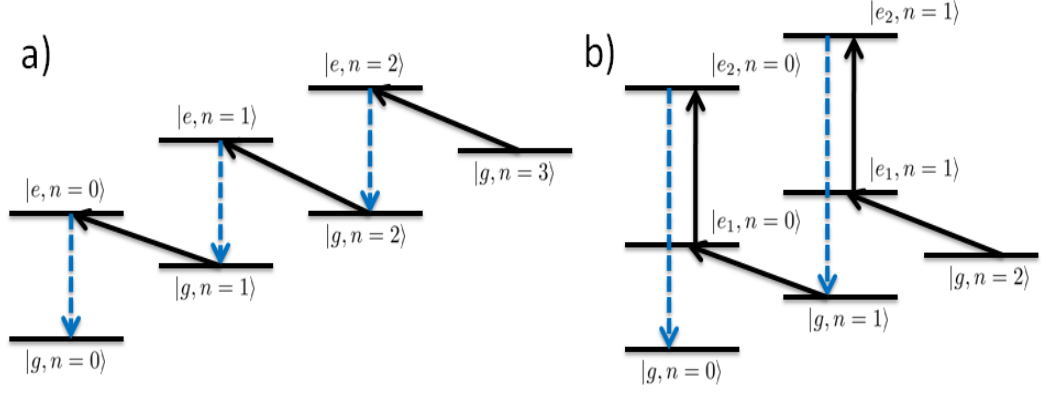


Figure 8: (a) Each excitation to the upper state lowers the number of vibrational quanta by one. (b) The lifetime of the upper level may be artificially shortened by coupling to an auxiliary level that has a higher decay rate, which speeds up the cooling process.

After successful sideband cooling, the atomic ion will be cooled to $T \approx 10\mu\text{K}$ for an axial frequency of 600 kHz. It should be noted that the temperature is a representation of the zero-point kinetic energy. The quantum limited motion of the ion after sideband cooling has been used to perform high resolution spectroscopy [38, 39, 102], to perform basic trap characterization [103, 104], and as a qubit due to its long coherence time [90].

2.2.3 Sympathetic cooling

Sympathetic cooling of trapped ions has been demonstrated by many groups, as discussed in Chapter 1 [36, 37, 34, 38, 39]. With two ions in a trap, one can be laser cooled while the other has no direct interaction with the laser field. There are two ways to achieve this. First by focusing the laser such that the second ion does not interact with the beam, or more commonly, by using a different ion species. The thermalization of the two ions, which is possible due to the Coulomb interaction, allows the ion being laser cooled to dampen the motion of the other ion. Thermalization allows ions without accessible laser cooling transitions to be cooled via the Coulomb interaction. This was first demonstrated by Larson *et al.* [105].

2.2.4 Trap heating

A common concern for high precision measurements in ions traps is heating of the motional states of the ion. Excess trap heating leads to broadening of transitions and to decoherence of the system, which is a major problem for many quantum computing protocols [106]. Trap heating is thought to come from electrical noise or charge build up on the electrodes [106]. Quantifying the trap heating is determined by turning the cooling lasers off for a fixed time, which typically results in an increase in motional quanta. There are two methods for measuring the heating rate. The first method uses the fluorescence during Doppler re-cooling to determine the heating, and the second uses the change in the motional sideband amplitudes [107, 104].

2.3 *Conclusion*

In this chapter, we have defined the trap potential and described the motion of a trapped ion in terms of the Mathieu stability parameters. It was shown that the motion of the ion is harmonic, which allows us to describe the effective pseudopotential which defines a harmonic oscillator potential. This chapter also introduced the basic concepts of Doppler, sideband, and sympathetic cooling of a trapped ion. These are all fundamental concepts used to perform the experiments described in this thesis. Chapter 4 uses Doppler cooling and heating for a novel spectroscopy technique. In Chapter 5, we use the motional sidebands of the optical qubit transition to identify dark molecular ions.

CHAPTER III

EXPERIMENTAL OVERVIEW

Now that the general concepts of ion traps and laser cooling techniques have been introduced in Chapter 2, it is possible to explore the basic experimental overview. This chapter introduces the atomic ion used in our experiment, the laser systems, and the experimental apparatus. It should be noted that any atomic ion which has a hydrogen-like structure (alkali earth metals, Yb^+ , Hg^+ , Cd^+ , Zn^+) can be used for similar experiments. These ions have simple energy structures resulting in direct cooling transitions. In this work, we choose Ca^+ because the transitions are positioned such that standard diode lasers are readily available. Also, the mass allows for a fixed set of trap parameters to probe a variety of species with different masses using sympathetic cooling and heating techniques. In this thesis two similar experimental setups are used and both are described in detail in this chapter.

3.1 Sublimation and ionization of calcium

To trap calcium, it is first sublimated and then photoionized. Solid calcium is sublimated by resistively heating a stainless steel packet with a small hole in the center sending a stream of hot calcium through the trapping region. Calcium ions can be isotopically selected via two photon photoionization of neutral calcium (Figure 10) by exciting the $4s^2\ ^1S_0 \leftrightarrow 4s5p\ ^1P_1$ transition at 423 nm [108, 109]. A second photon at 375 nm then ionizes the excited calcium. Figure 9 is a CCD image of different numbers of ions loaded into the trap. We use the abundant isotope, $^{40}\text{Ca}^+$, for most

experiments and an energy level diagram is shown in Figure 10. Each of the transitions can be addressed with the appropriate laser, and the details of each of the transitions, along with isotope shifts, are shown in Tables 1 and 2 [110, 108, 109, 97].

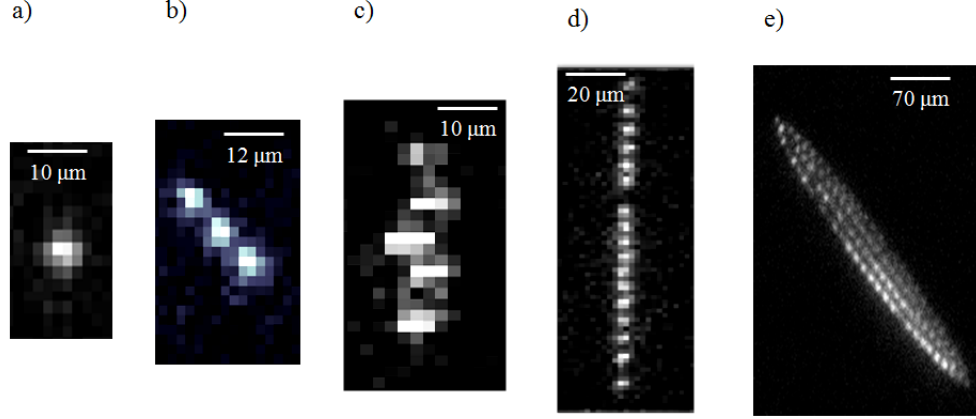


Figure 9: CCD image of calcium ions in the trap. a) one ion b) string of three ion c) string of five ions d) string of 18 ions e) large Coulomb crystal of ions.

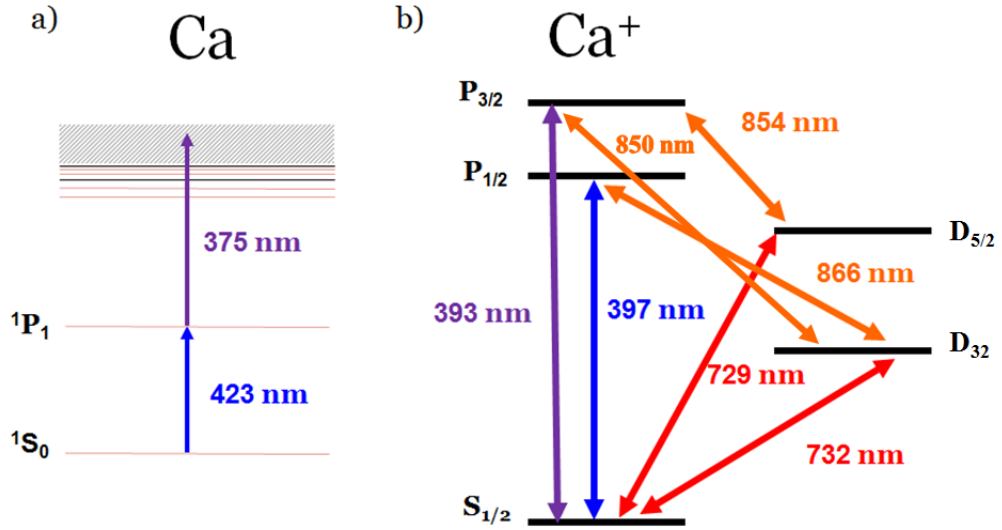


Figure 10: (a) Two photon photoionization of neutral calcium (b) Energy diagram of singly ionized calcium

3.2 Laser systems and frequency stabilization

All lasers necessary for cooling Ca^+ are commercially available as diode lasers. The photoionization lasers consist of an external cavity diode laser (ECDL) at 846 nm,

Table 1: Physical properties of ^{40}Ca . * Relevant neutral calcium transition.[110, 35, 36, 40, 97]

Transition	Calcium Frequency (air) (THz)	$A_{21}/2\pi$ (s^{-1})	t_{spont}
$^1S_0 - ^1P_1$ (423 nm)*	709.07837 [110]	2.18×10^8	0.73 ns
$S_{1/2} - P_{3/2}$ (393 nm)	761.9050 [35]	23.7×10^6	6.8 ns
$S_{1/2} - P_{1/2}$ (397 nm)	755 2228 [36]	22×10^6	7.1 ns
$S_{1/2} - D_{5/2}$ (729 nm)	411.0421 [40]	2.1×10^{-1}	0.77 s
$S_{1/2} - D_{3/2}$ (732 nm)	409.2122 [97]	2.1×10^{-1}	0.77 s
$D_{3/2} - P_{3/2}$ (850 nm)	352.6734 [97]	176×10^3	900 ns
$D_{5/2} - P_{3/2}$ (854 nm)	352.6734 [97]	1.6×10^6	101 ns
$D_{3/2} - P_{1/2}$ (866 nm)	345.9913 [97]	1.7×10^6	94.3 ns

Table 2: Isotope transition shifts in MHz. All shift can be found in Ref. [110, 108, 109]

Mass number	Natural abundance	Ca $^1S_0 - ^1P_1$ 423 nm	Ca ⁺ S-P 397 nm [393 nm]	Ca ⁺ P-D 866 nm [854, 850 nm]
40	96.9 %	0	0	0
42	0.647 %	393.1	426	-2340
43	0.135 %	610.7	688	-3465
44	2.09 %	773.8	842	-4496
46	0.004 %	1160	1287	-6478
48	0.187 %	1513.1	1697	-8288

which is cavity-enhanced and frequency-doubled to 423 nm (Toptica SHG 110), and a free-running 375 nm laser diode (Nichia). The Ca⁺ Doppler cooling lasers are a tapered amplified ECDL at 792 nm, which is cavity-enhanced and frequency-doubled to 397 nm (Toptica TA-SHG 110), or an ECDL at 397 nm (Toptica DL100), and one of two ECDLs at 866 nm (Toptica DL100). Each Doppler cooling laser is stabilized with a Toptica PID lock circuit using a home built low finesse Ultra Low Expansion (ULE) cavity with piezo control for easy tunability. The sideband cooling lasers are an ECDL at 854 nm (Toptica DL100), which is locked to a High Finesse WS7 wavemeter [10 MHz resolution and 60 MHz (3σ) absolute accuracy] and an ECDL at 729 nm. The 729 nm laser is locked with a home built Pound-Drever Hall circuit to an Advanced Thin Film ULE etalon cavity, with a finesse of ≈ 100000 , which is held at high vacuum (10^{-8} torr) with two stages of temperature control ($\Delta T=0.01^\circ\text{C}$). The 729 nm laser

is narrowed using a Toptica Fast Analog Linewidth Control (FALC 110) with active feedback to a Field-Effect Transducer (FET) on the current. The result is a 500 kHz laser narrowed to 10 kHz. The laser powers and beam profiles are measured using a Thorlabs S140A power meter (5% error) and a Thorlabs WM100-SI beam profiler (5% error). In some cases, the lasers are pulsed using shutters with 2-ms response times (Uniblitz VS25), but most experiments are controlled using AOMs and driven with a home built pulse programmer consisting of an Opal Kelly XEM3010-1000 Field Programmable Gate Array (FPGA) and three Analog Devices AD9850 Direct Digital Synthesizer (DDS) controllers.

3.3 Experimental traps, vacuum systems and imaging systems

3.3.1 Atomic ion trap

The experiments described in Chapter 4 are performed in a linear Paul trap held in vacuum at 1×10^{-10} torr. The trap is a five-segment version of the three-segment trap described in Ref. [111] and a duplicate of the trap used in Ref. [112]. The trap parts were machined at the University of Osaka under the supervision of Prof. S. Urabe. Figure 11 shows an image of the trap along with a schematic of the electrode layout. The trap is driven at 14.5 MHz and the secular frequencies for $^{40}\text{Ca}^+$ are measured to be 0.5, 1.0, and 1.3 MHz. It should be noted that when a from Equation 15 is not zero, then $\omega_x \neq \omega_y$ resulting in three secular frequencies. The ion micromotion is minimized by applying compensation voltages (to electrode 2, 3, and the compensation electrode) while measuring the correlation between the fluorescence and the trap drive [92].

Ion fluorescence is collected simultaneously using an electron-multiplied CCD (EMCCD) camera (Princeton Instruments Photon Max 512) and a photon counter (Hamamatsu H7360-02 with a dark count rate of 50 counts/second). A beam splitter directs 70% of the light to the photon counter which measures fluorescence. The

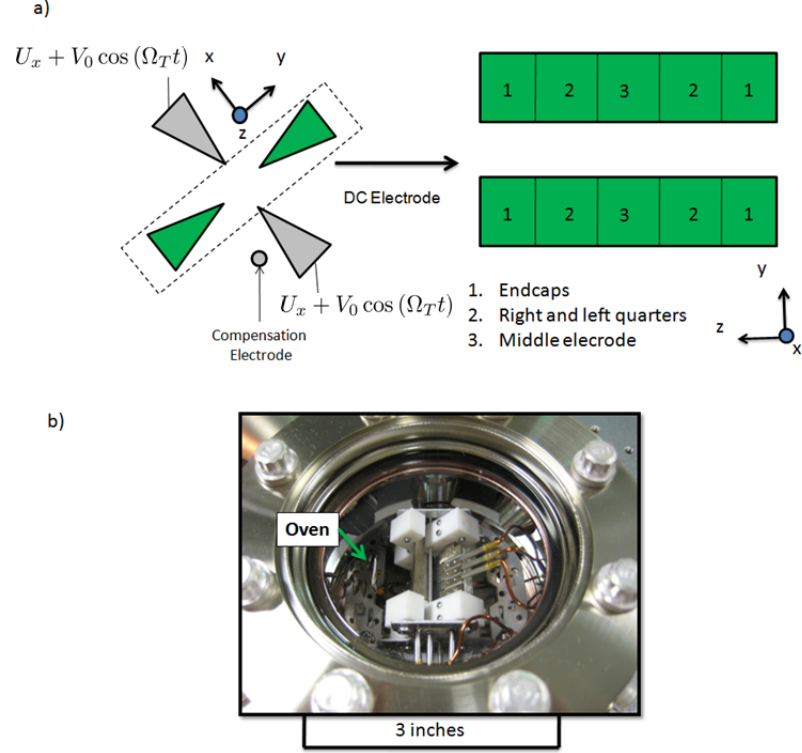


Figure 11: (a) Schematic of the linear ion trap electrode structure (b) Image of ion trap under vacuum

spatial resolution of the EMCCD is used to monitor ion position and ion loss. The collection efficiency at the photon counter (including all losses) is 0.01% of the photons scattered from the ion.

3.3.2 Molecular ion trap

The experiments in Chapter 5 are performed in a linear Paul trap held in vacuum at 2×10^{-10} torr. The trap consists of eleven wedge-shaped segments allowing for up to five distinct trapping regions. All electrodes are made of Nitronic 50 stainless steel. The trap was machined by Wiesmanntool, Inc, of Roswell, GA and designed by James Goeders. A more detailed description of the trap can be found in Ref. [113]. The trap is driven at 14 MHz and typical secular frequencies for $^{40}\text{Ca}^+$ are 0.7 MHz in the axial direction and 1.2 MHz radially but vary depending on the trap parameters.

The edge of each electrode has a curvature of 0.5 mm and is located a distance $r_0=1.0$ mm from the trap axis. Diagonally opposed rf electrodes span the entire length of the trap (52 mm total). DC electrodes are also diagonally opposite, and consist of nine 3 mm wide electrodes arranged at 0.5 mm intervals, and two 10 mm wide endcaps. The electrode structure is shown in Figure 12. Additionally, two stainless steel rods of 0.8 mm diameter and 52 mm in length are placed 5 mm from the trap axis, for the application of compensation voltages. The eleven segments are secured along one axis by screwing them into 5 mm thick Macor plates placed on the side of the electrodes furthest from the trapping region. The electrodes are secured in the other two axes by Macor rods 3 mm in diameter that run the length of the trap. Two grounded 10 mm thick stainless steel end pieces secure the Macor rods and plates in place and are located 5 mm from the endcaps.

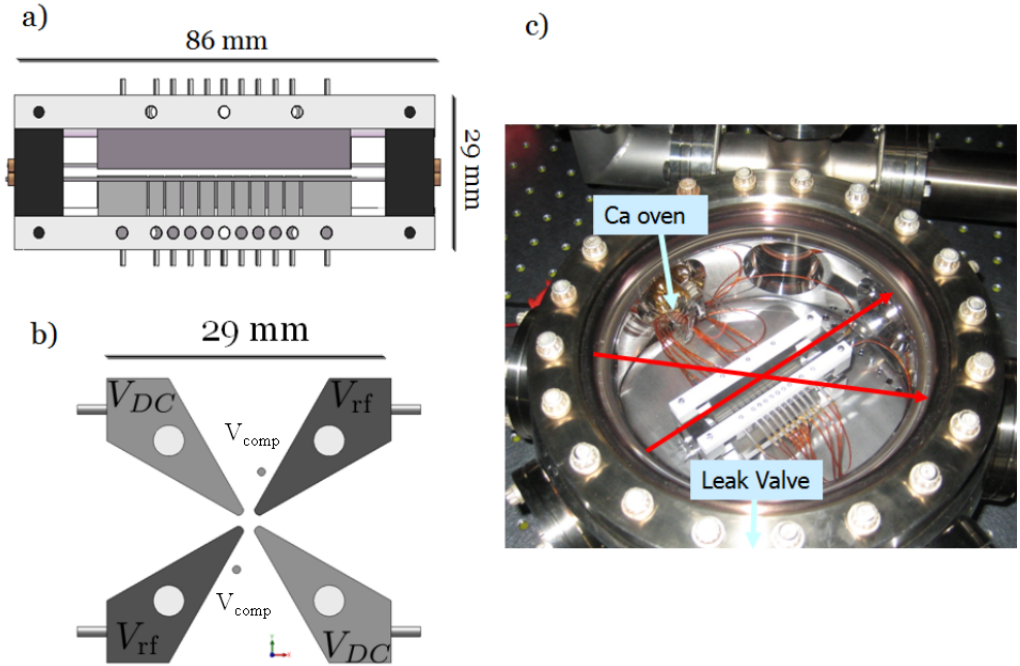


Figure 12: (a) side and (b) axial CAD drawing of the linear ion trap electrode structure (c) Image of ion trap and vacuum chamber

In this set-up, we image the ions by sending 30 % of the signal to a CCD (SBIG Astronomical Instruments ST-3200) and the remaining signal to a photon counter (Hamamatsu H10682 with a dark count rate of 30 counts/second) . All fluorescence measurements are obtained using the photon counter, and after considering all losses we determine a collection efficiency of 0.04 % for the photon counter.

3.4 Conclusion

In this chapter, basic information about our experimental setup, laser system, and atomic ion were introduced in detail. The experiments described in the following chapters reference this chapter and specific sections to distinguish which setup is used. The atomic trap is used in Chapter 4 to perform sympathetic heating spectroscopy, and the molecular trap is used in Chapter 5 to perform resolved sideband spectroscopy on the optical qubit transition.

CHAPTER IV

SYMPATHETIC HEATING SPECTROSCOPY OF CALCIUM ISOTOPES

This chapter is based on

Craig R. Clark, James E. Goeders, Yatis K. Dodia, C. Ricardo Viteri, and
Kenneth R. Brown, Phys. Rev. A, **81**, 043428 (2010).

4.1 Introduction

Laser-cooled ions in linear Paul traps are an ideal tool for studying gas phase atomic and molecular ions at very low temperatures. The large trapping depth (on the order of eV) and the wide mass acceptance range allow the simultaneous trapping of different ion species. An ion that can be laser cooled can be used to sympathetically cool another species through the Coulombic interaction between the ions [78, 79, 114, 81, 115, 116, 80, 117]. Sympathetic cooling brings the motion of all trapped ions to the equilibrium temperature of the laser-cooled ions [118] in a time proportional to the secular frequency of the trap [119, 120]. Controlled ensembles of cold atomic and molecular ions have the potential for many applications, including: quantum information processing [23, 24], ultra-high-resolution spectroscopy [24, 34, 35, 36, 37], optical clocks [38, 39], nano deposition of dopant atoms in semiconductors [121], and studies of molecular properties and chemical reactions [43, 45, 46, 47, 48, 44, 49, 50, 51, 52, 53].

At low temperatures the trapped ions form an ordered structure known as a Coulomb crystal. This presents an opportunity to heat the crystal with one ion

and detect that heating with another. Laser-cooled fluorescence mass spectrometry (LCFMS) [78] uses a probe voltage at the secular frequency of the target ion to heat the crystal. The fluorescence drops as the cooling ions are sympathetically heated and Doppler shifted with respect to the cooling laser. The charge-to-mass ratio of the target ion can then be determined. This method has been applied to detect the photofragmentation of molecular ions in a Coulomb crystal [122, 52, 53, 123].

Resonance-enhanced multiphoton dissociation, in combination with LCFMS, can be used to gain high-resolution spectral information as demonstrated with a crystal of HD^+ and Be^+ ions [122]. First, a vibrational overtone line was excited in HD^+ with an infrared diode laser locked to a stable frequency comb. An UV laser then transferred the excited population to a dissociative state. The HD^+ population decay can then be monitored by observing the Be^+ fluorescence. The resulting spectral line had a width of 40 MHz, dominated by Doppler shifts due to the micromotion inherent in large crystals in a linear quadrupole ion trap. Recently, the same rotational state selective dissociation spectroscopy technique has been utilized to map the state populations of translationally and vibrationally cold molecular ions and achieve a high degree of rotational cooling [123, 55, 56].

Narrower linewidths can be achieved by limiting the ions to a linear chain. Quantum logic spectroscopy (QLS) transfers information between two trapped ions, a logic ion and a spectroscopy ion, through the quantized vibrational motion of the crystal. The logic ion serves as a quantum sensor for detecting transitions in the spectroscopy ion [24]. The reported absolute frequency measurements on single trapped ions using QLS have been performed on narrow transitions [38, 39] where the secular frequency of the ions in the trap exceeded the transition linewidth. In this strong-binding limit [102], the absorption spectrum consists of a carrier and a number of motional

sidebands separated by the secular frequency. Initialization in QLS experiments requires cooling of the vibrational modes of the crystal to the ground state, which is achieved by addressing the motional sidebands [62].

There are a wide variety of interesting transitions that cannot be studied with QLS due to their large linewidths. High-precision spectroscopy outside the strong-binding limit is challenging since the spectroscopy laser induces detuning-dependent heating and cooling which distorts the line profile. Recently, experiments in the weak binding limit have been performed using low-intensity spectroscopy laser beams on a chain of sympathetically cooled ions [36, 37, 34]. The sympathetic cooling removes the heating limitation by counteracting the back action of the interrogating lasers. High resolution is achieved by calibrating the probe laser to an absolute frequency by referencing it to a frequency comb or using the comb light directly [35]. In this case, the ion fluorescence is measured directly as the constantly sympathetically cooled ion absorbs the minimal heating due to the low intensity lasers.

In this work, the frequency-dependent heating of a spectroscopy ion is measured by observing the fluorescence of a second ion (control ion) as the system is recooled. We refer to this method as sympathetic heating spectroscopy (SHS). The method is demonstrated on two isotopes of calcium: $^{40}\text{Ca}^+$, the control ion, and $^{44}\text{Ca}^+$, the spectroscopy ion. Even a low scattering rate of photons from the spectroscopy ion can create a significant stochastic optical force that builds up quickly with the laser interaction time (t_{heat}), and dramatically changes the trajectory of both ions. This results in a large Doppler shift of the control ion which can be observed in the re-cooling process. Laser induced fluorescence (LIF) experiments using similar very low laser intensities will require long photon counting times to acquire line profiles with decent signal to noise. Potentially, SHS can become an effective tool to study dipole transitions that are weak or fall in regions of the electromagnetic spectrum where the sensitivity of detectors is marginal or non-existent.

4.2 *Experiment*

4.2.1 Experimental setup

The experiments in this chapter are performed in the atomic trap described in Sec. 3.3.1. The Doppler recooling method [103, 104] was used to measure the trap heating. For a single ion, no heating was observed for dark times up to 20 s.

The experiment requires the loading of one $^{40}\text{Ca}^+$ and one $^{44}\text{Ca}^+$. This is accomplished using resonance-enhanced two-photon ionization [124, 125, 108] as described Sec. 3.1 with appropriate laser frequencies for Doppler cooling/heating as shown in Table 1.

The absolute frequency calibration involves measuring the fluorescence spectra for each ion (Figure 13) and fitting to a three-level system, which allows for coherent population trapping when $\Delta_{397} = \Delta_{866}$ (blue dot-dashed line) [96]. The only adjustable parameters are the frequency center of the $S_{1/2}$ - $P_{1/2}$ and $D_{3/2}$ - $P_{1/2}$ transitions. The resulting uncertainties in the absolute frequencies are 13 MHz for the $S_{1/2}$ - $P_{1/2}$ transition and 20 MHz in the $D_{3/2}$ - $P_{1/2}$ transition.

4.2.2 Experimental procedure

Sympathetic Heating Spectroscopy (SHS) detects the scattering of photons from a spectroscopy ion by observing the heating and recooling of a control ion (Figure 14). Initially, the two ions are trapped (Figure 14(a)), and the spectroscopy ion is sympathetically cooled by a laser-cooled control ion (Figure 14(b)). By turning off the laser-cooling on the control ion and applying a near-resonant laser to the spectroscopy ion, the two-ion system will be heated (Figure 14(c)) for a time t_{heat} . The resulting laser heating is measured by blocking the spectroscopy laser and monitoring the fluorescence of the control ion as it recools (Figure 14(d)).

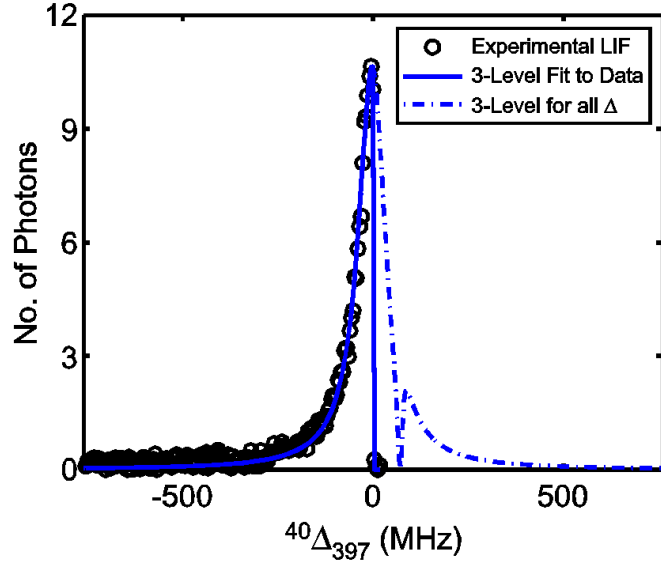


Figure 13: Emission spectrum of the $S_{1/2}$ - $P_{1/2}$ line of a calcium ion. Each data point (circles) is the number of photons acquired in 3 ms for each 397 nm laser detuning, $^{40}\Delta_{397}$ (averaged over 100 experiments). The solid blue line is a fit to the data using Equation (9) of Ref. [96] which theoretically describes the scattering rate for a three level system. The fitting function is evaluated over the range of $^{40}\Delta_{397}$ where fluorescence is observed. The blue dotted line shows the complete theoretical scattering profile across negative and positive detunings (assuming a motionless ion) when $^{40}\Delta_{866} = 20$ MHz, $^{40}s_{866} = 1000$ and $^{40}s_{397} = 8$.

This technique is demonstrated using two isotopes of Ca^+ . In the experiments, the $^{40}\text{Ca}^+$ serves as the control ion and the $^{44}\text{Ca}^+$ as the spectroscopy ion. The $^{40}\text{Ca}^+$ lasers are detuned $^{40}\Delta_{866} = 20$ MHz and $^{40}\Delta_{397} = -30$ MHz from resonance with intensities fixed to yield saturation values of $^{40}s_{866} = 1000$ and $^{40}s_{397} = 8$. In the absence of ions in the trap, the photon counter reads ~ 500 photons/second of background scattering at these laser intensities. The $^{44}\text{Ca}^+$ repumper laser has a fixed detuning $^{44}\Delta_{866} = 20$ MHz, while the $^{44}\Delta_{397}$ is varied to obtain spectra for a range of laser intensities.

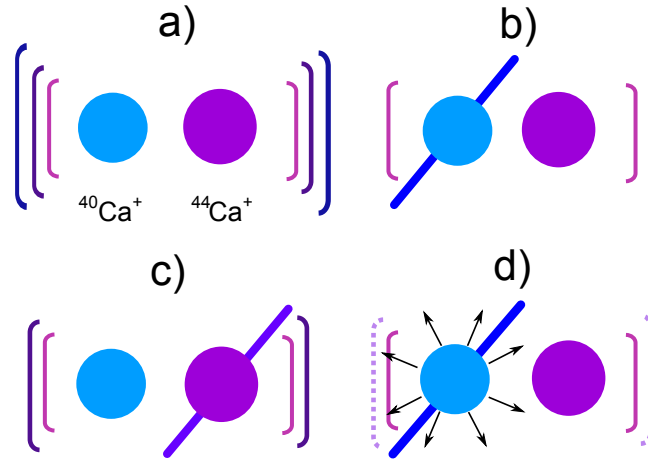


Figure 14: Procedure for Sympathetic Heating Spectroscopy. The solid circles represent the two ions, the brackets represent the magnitude of vibrational energy in the Coulomb crystal, and the diagonal line represents an applied laser beam. (a) First, the spectroscopy ($^{44}\text{Ca}^+$) and control ($^{40}\text{Ca}^+$) ions are trapped. (b) The Coulomb crystal is then laser cooled via the control ion. (c) By simultaneously switching off the cooling laser and turning on the induced heating laser, the Coulomb crystal heats for a fixed interaction time (t_{heat}). (d) Finally, the magnitude of heating is observed by measuring the fluorescence of the control ion as the crystal recools.

Doppler recooling curves are obtained for a range of t_{heat} , laser intensities, and detunings. Two representative curves are shown in Figure 15 illustrating the return of the $^{40}\text{Ca}^+$ fluorescence to steady state as the ions are cooled. In comparison, a third curve shows that without spectroscopy lasers there is no visible heating at $t_{\text{heat}} = 250$ ms. Each of the three curves is an average of 20 individual experiments and the data points measure the number of photons collected in a time t_{bin} . Due to a limited

number of available measurement bins (100 per experiment), the first 70 points are taken consecutively, and the last 30 points are taken every other time bin. This gives us the ability to observe the dynamic return to steady-state fluorescence at short times with a higher resolution. Depending on the experimentally observed fluorescence, t_{bin} is chosen to be between 3 and 8 ms to ensure that most of the trajectories reach a steady-state fluorescence. Recooling lasers remain on for an additional 500 ms (t_{int}) to ensure that the system is initialized.

The heating and recoiling is stochastic, and the individual experiments show a variety of behaviors for the same laser parameters (Figure 16). To simplify the measurement, we report the percent of experiments where there is noticeable heating at short times, P_{heat} . To calculate P_{heat} , the average number of photons in the first three data points is compared to a threshold value, $T = \langle \Gamma_c \rangle t_{\text{bin}} - 2\sigma$, where $\langle \Gamma_c \rangle$ is the steady-state scattering rate and σ is the standard deviation of the Poissonian distribution. If the signal is below the threshold, the experiment is marked as heating. False positives for cases without heating occur less than 2.5% of the time. An example of applying this threshold to experimental data is shown in Figure 17. A clear distinction between heating and no heating is observed.

SHS is compared to the expected fluorescence for a cold ion,

$$I_{\text{LIF}} = \langle \Gamma_s \rangle t_{\text{meas}} \quad (35)$$

where Γ_s is the steady state scattering rate of the spectroscopy ion ($^{44}\text{Ca}^+$) calculated using Equation (9) of Ref. [96], and scaled by our experimental collection efficiency. In SHS, no signal is collected during t_{heat} and t_{int} , but for LIF, photons can be collected the whole time, thus $t_{\text{meas}} = t_{\text{heat}} + 130 \cdot t_{\text{bin}} + t_{\text{int}}$. In practice, many experiments should be averaged to obtain a fluorescence spectrum with a high signal to noise ratio.

An SHS signal is expected when $^{44}\Delta_{397} > 0$, which is the opposite of the standard fluorescence spectra (Figure 13) where fluorescence is detected when $^{44}\Delta_{397} < 0$. In

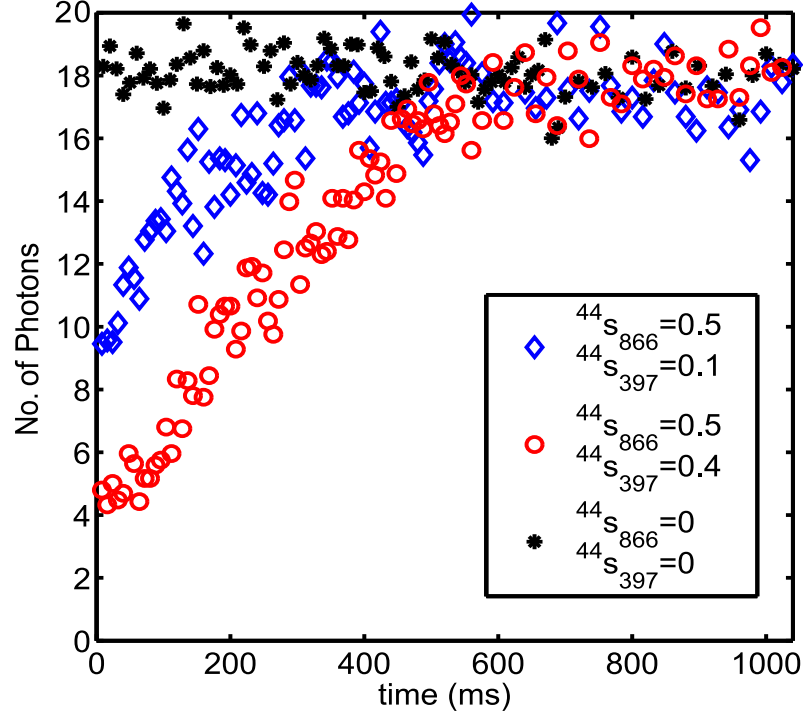


Figure 15: Comparison of Doppler recoiling fluorescence for three laser-induced heating parameters. In two heating situations, lasers are kept at $^{44}\Delta_{866} \approx 20$ MHz, $^{44}\Delta_{397} \approx 40$ MHz, and $^{44}s_{866} = 0.5$. Blue diamonds and red circles show recoiling after laser induced heating is applied on the spectroscopy ion with intensities proportional to $^{44}s_{397} = 0.1$ and $^{44}s_{397} = 0.4$, respectively, and for a period of $t_{\text{heat}} = 250$ ms. The black points show no deviation from steady-state fluorescence after turning off all lasers for the same period of time. Each time dependent curve is the average of 20 fluorescence trajectories. The ordinate shows the mean number of photons detected in 8 ms.

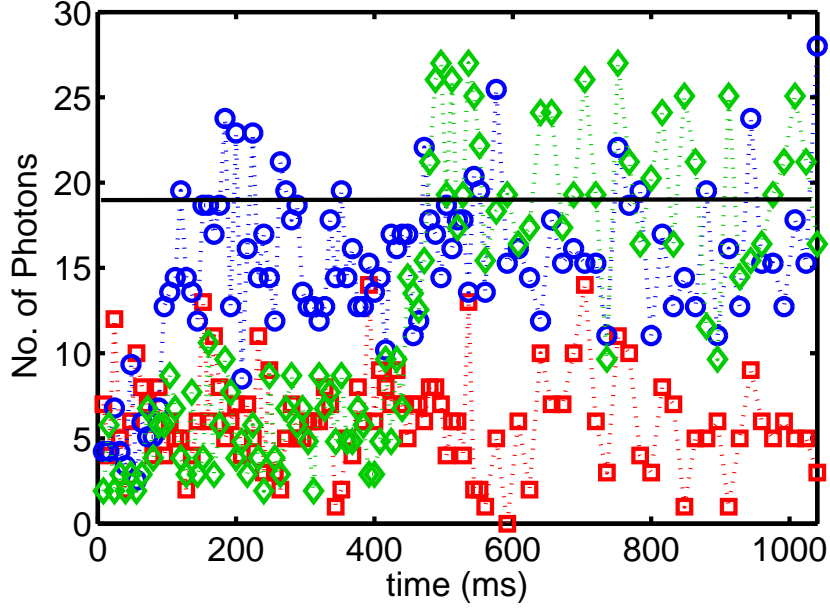


Figure 16: Example of three single Doppler recoiling fluorescence trajectories after heating of the Coulomb crystal for the average shown in Figure 15 by the red circles. The black line represents the average steady state fluorescence over all 20 experiments. The ordinate shows the number of photons detected in 8 ms. Dotted lines are to guide the eye.

the standard measurement, the laser cools the ion and reduces the Doppler shift to below the natural linewidth. As a result, the observed fluorescence can be described assuming the ion is motionless. For SHS, the ion is heated by the scattered photons and the resulting Doppler shift dramatically changes the scattering rate. How the total heating depends on the interaction time and the laser intensities is difficult to calculate. Experiments examining the limits of detecting this heating are now described.

4.2.3 Effect of laser powers on SHS

The photon scattering rate and laser heating are most strongly affected by the power of the 397 nm laser. Figure 18(a) shows the variation in the SHS spectra with 397 nm laser power. The spectra has a wide range of detunings yielding equivalent signals. The maximum signal is detected with $^{44}\Delta_{397}$ between +10 and +70 MHz. The spectra

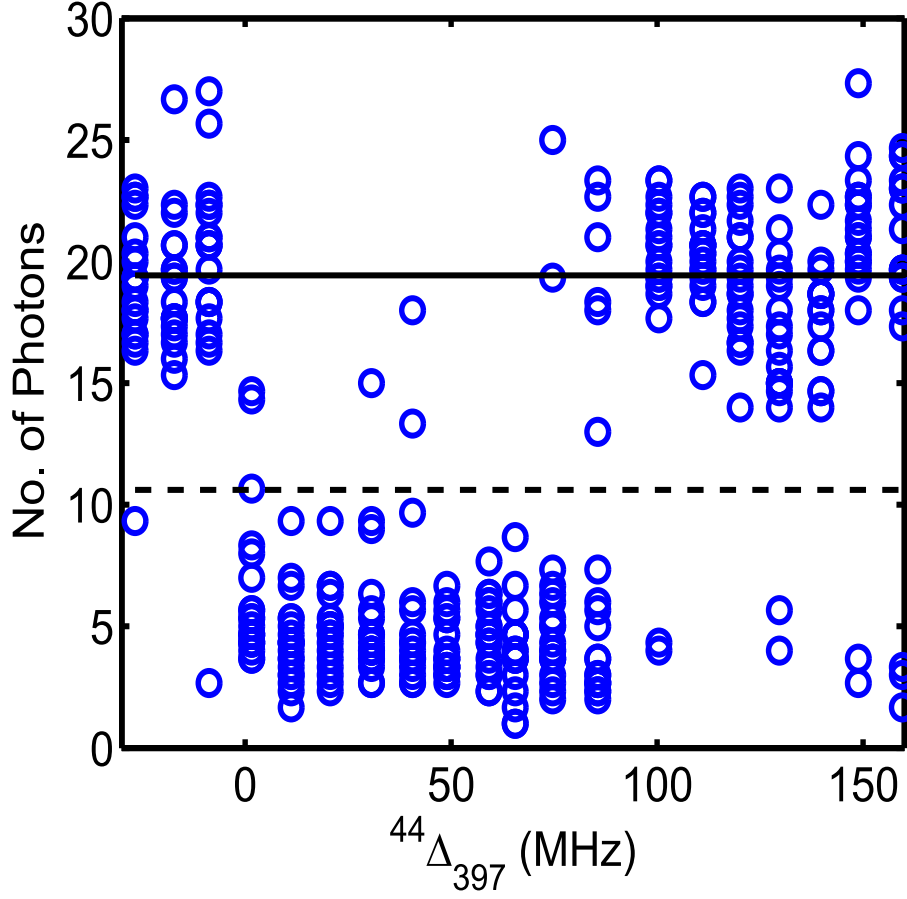


Figure 17: Average of the first 3 fluorescence points for 20 Doppler recoiling trajectories versus heating laser detunings. The ordinate shows the average number of photons detected in 8 ms. The solid black line shows the average steady-state fluorescence for a cold crystal. The dotted black line represents the threshold, which is 2σ from the average of the steady-state fluorescence and is used to determine whether heating is observed during the experiment (spectroscopy laser parameters: $^{44}\Delta_{866} = 20$ MHz, $^{44}s_{866} = 0.5$, and $^{44}s_{397} = 0.4$).

have a sharp rise at zero detuning, and the width of the peak reduces with laser power resembling the trend observed for the calculated LIF spectra in Figure 18(b). For certain laser intensities and detunings, the three-level system shows fine features arising from both resonance with dressed states and coherent population trapping [126]. Following Ref. [96], the calculations assume lasers without linewidths and a motionless ion.

A difficulty in the measurement of atomic and molecular spectra by fluorescence arises from the existence of metastable states. In Ca^+ , the effective lifetime of the metastable $D_{3/2}$ state can be controlled by the intensity of the 866 nm laser. Example SHS spectra are shown in Figure 19(a) for varying $^{44}\text{s}_{866}$. A less pronounced effect on peak width is observed compared to changing $^{44}\text{s}_{397}$, which is the same trend observed in the predicted LIF spectra shown in Figure 19(b). SHS spectra show laser induced heating more than 50% of the time at $^{44}\Delta_{397}$ between +5 and +65 MHz for all of the experimental repumper laser intensities.

4.2.4 Effect of t_{heat} on SHS

In order to determine the limits of observable heating, the laser powers were decreased and the heating time extended. The heating time plays a large role in the accumulative heating mechanism, as shown in Figure 20. The P_{heat} line profiles not only increase in height, but also broaden. For long heating times the red edge of the peak is within 10 MHz of the $S_{1/2}$ - $P_{1/2}$ transition (blue circles and red squares). This is not the case as the heating time is reduced (green diamonds). In future work, we plan to connect the peak of the accumulated heating spectra to the transition peak center and linewidth.

The heating rate of the trap limits the amount of laser induced heat that can be detected. For a single ion, no heating is measured up to 20 seconds. For two ions, a small amount of heating is observable at 1 second corresponding to a $P_{\text{heat}} \approx 10 - 30$

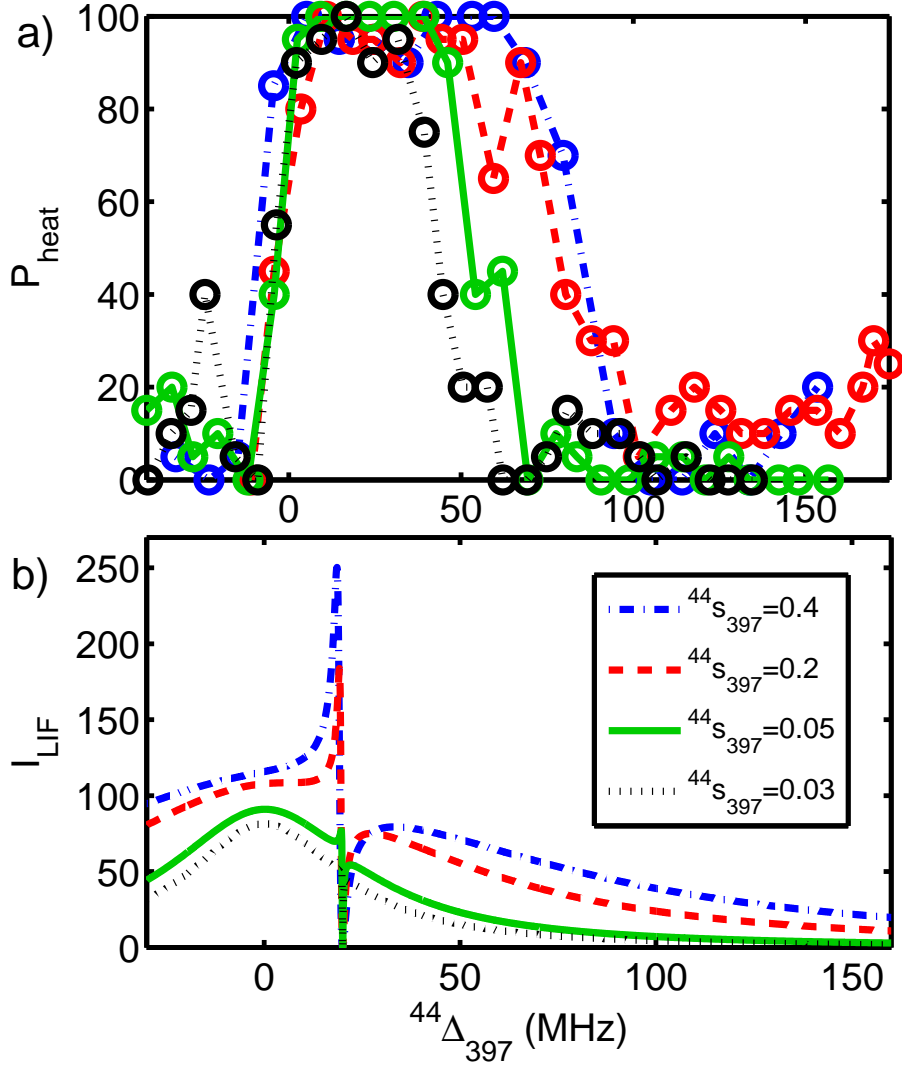
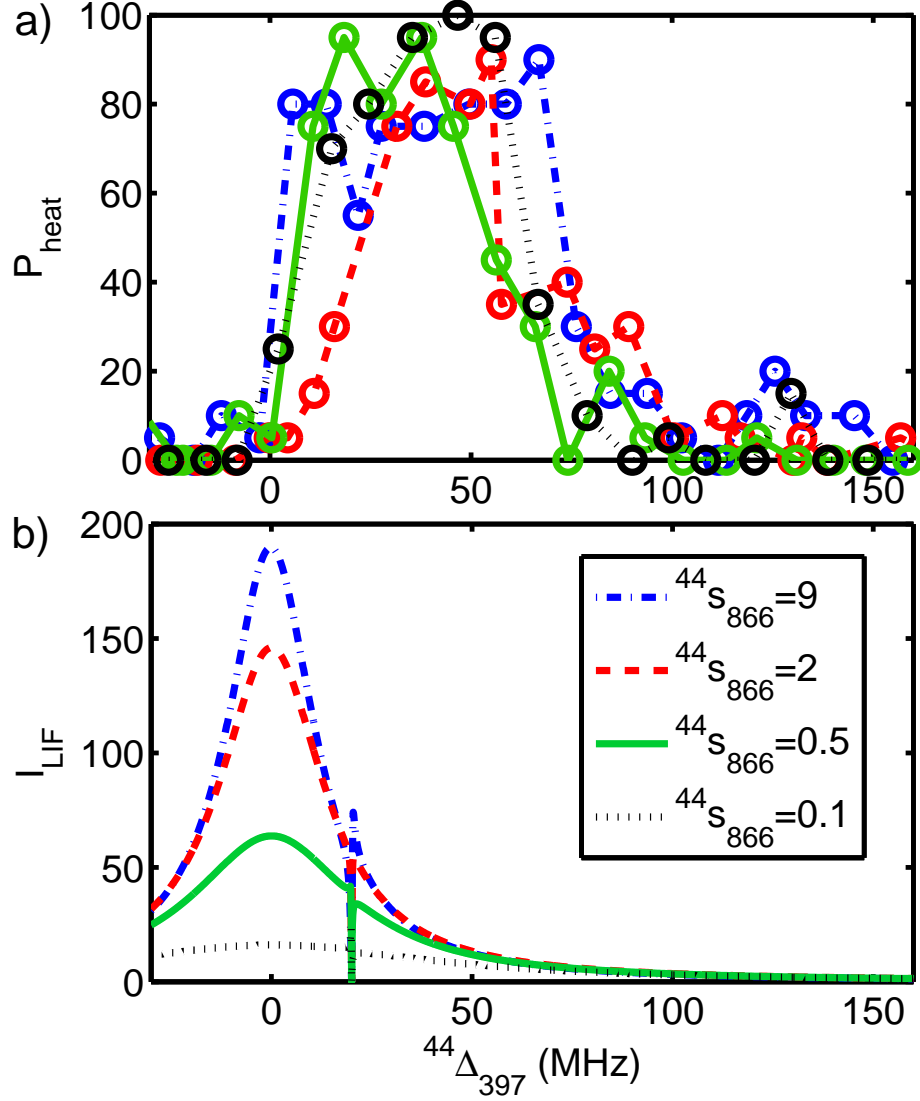


Figure 18: (a) The effect of varying the power of the heating laser, $^{44}s_{397}$, on the SHS spectra. The repumper laser is held constant at $^{44}\Delta_{866} = 20$ MHz with an intensity proportional to $^{44}s_{866} = 0.5$. Percentages are based on 20 experiments for each $^{44}\Delta_{397}$ with $t_{\text{bin}} = 8$ ms and $t_{\text{heat}} = 250$ ms. SHS peaks are clearly saturated, and broadening is correlated with the intensity of the 397 heating laser. Lines connecting experimental data are to guide the eye. (b) Simulated I_{LIF} using the same experimental parameters and $t_{\text{meas}} = 1.79$ s. A monotonic broadening of the profile is seen with increasing $^{44}s_{397}$ at the chosen set of repumper experimental parameters.



s

Figure 19: The effect of varying the power of the heating repumper laser, $^{44}s_{866}$, at constant detuning ($^{44}\Delta_{866} = 20$ MHz), on the SHS spectra. Percentages are based on 20 experiments for each $^{44}\Delta_{397}$, which is held at a constant $^{44}s_{397}$ of 0.03 ($t_{\text{bin}} = 5$ ms and $t_{\text{heat}} = 250$ ms). Lines connecting experimental data are to guide the eye. (b) Simulated I_{LIF} using the same experimental parameters and $t_{\text{meas}} = 1.4$ s. The intensity of the repumper laser does not appear to have an effect on the linewidth when using a very low 397 saturation.

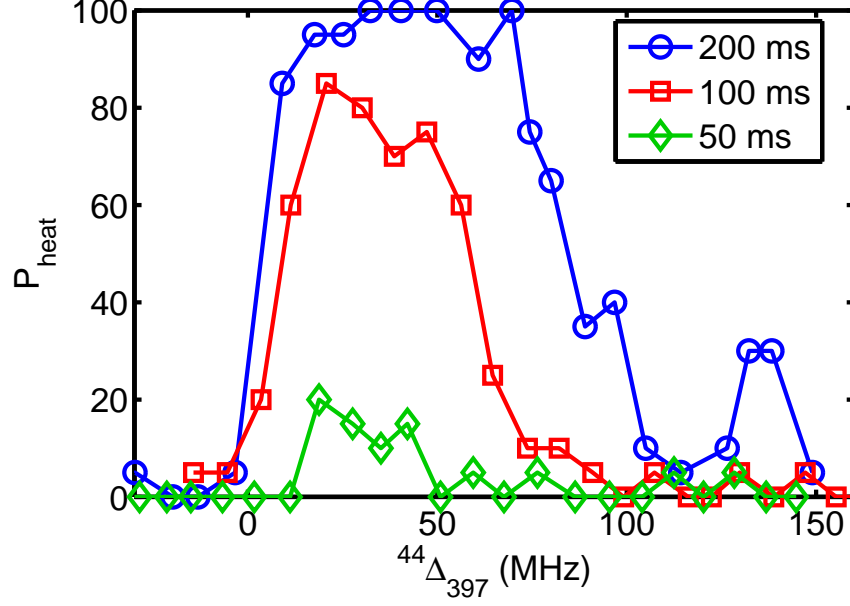


Figure 20: The effect of varying t_{heat} on SHS spectra. The intensity of the 397 spectroscopy laser is proportional to $^{44}s_{397} = 0.03$, and the heating repumper laser is tuned to $^{44}\Delta_{866} = 25$ MHz with a saturation value fixed at $^{44}s_{866} = 0.5$. Lines shown are to guide the eye.

and a temperature of approximately 7 K. Figure 21(a) shows that for very low laser powers ($^{44}s_{397}=0.01$ and $^{44}s_{866} = 1 \times 10^{-3}$), the P_{heat} spectrum has a signal to noise ratio of ~ 2 . The predicted LIF spectrum at these conditions is shown in Figure 21(b), together with a simulation of the photon counting noise associated with the dark counts of the device employed in these experiments. The number of scattered photons (I_{LIF}) is at least 9 times smaller than the photon shot noise. For $t_{\text{meas}} = 2$ s and averaging over 20 experiments, an $I_{\text{LIF}} > 4.5$ would be required to distinguish the laser induced fluorescence from noise in the detector with high confidence. One way to overcome the shot noise is to average over more than 7000 experiments. Alternatively, an increase in the collection efficiency will reduce the time required to obtain a LIF spectra. For SHS, the same detection improvement would enhance our ability to distinguish laser induced heating from trap heating.

A SHS signal is observed when the calculated optimal fluorescence would result in at most 1500 photons per second being scattered into a solid angle of 4π . This is very dim compared to the millions of photons per second typically scattered by alkaline earth ions. Experiments with extremely low heating powers, corresponding to a maximum fluorescence of a few hundred photons from the spectroscopy ion, resulted in indistinguishable signal from the case without heating lasers.

4.3 Conclusion

Sympathetic heating spectroscopy is a sensitive way to detect spectral lines in ions. In the experiment, a few scattered photons from the spectroscopy ion are transformed into a large deviation from steady-state fluorescence on the control ion. Although application to low-scattering rate transitions is natural, this technique would be most useful for transitions at the frequency limit of detectors.

The current work uses a simple metric, P_{heat} , to measure the heating in a two ion Coulomb crystal. This reveals the approximate line position but does not provide a clear method for determining the natural linewidth. The resolution of the spectrum is limited by the accumulative stochastic heating mechanism. A better understanding of the distribution of ion energies after heating and during the recoiling process may allow for the extraction of the transition dipole moment. Future work will include developing a Monte Carlo simulation that accounts for the effect of stochastic scattering of photons on the ion motion.

Furthermore, this work suggests a middle ground between QLS and SHS where the atomic sidebands are used to determine the temperature. This method will allow for the detection of even lower scattering rates with the limit being the absorption of a single photon as demonstrated by QLS [24]. Either this intermediate technique, or perhaps an improved SHS, would be able to resolve the peak centers of the Fe^+ lines

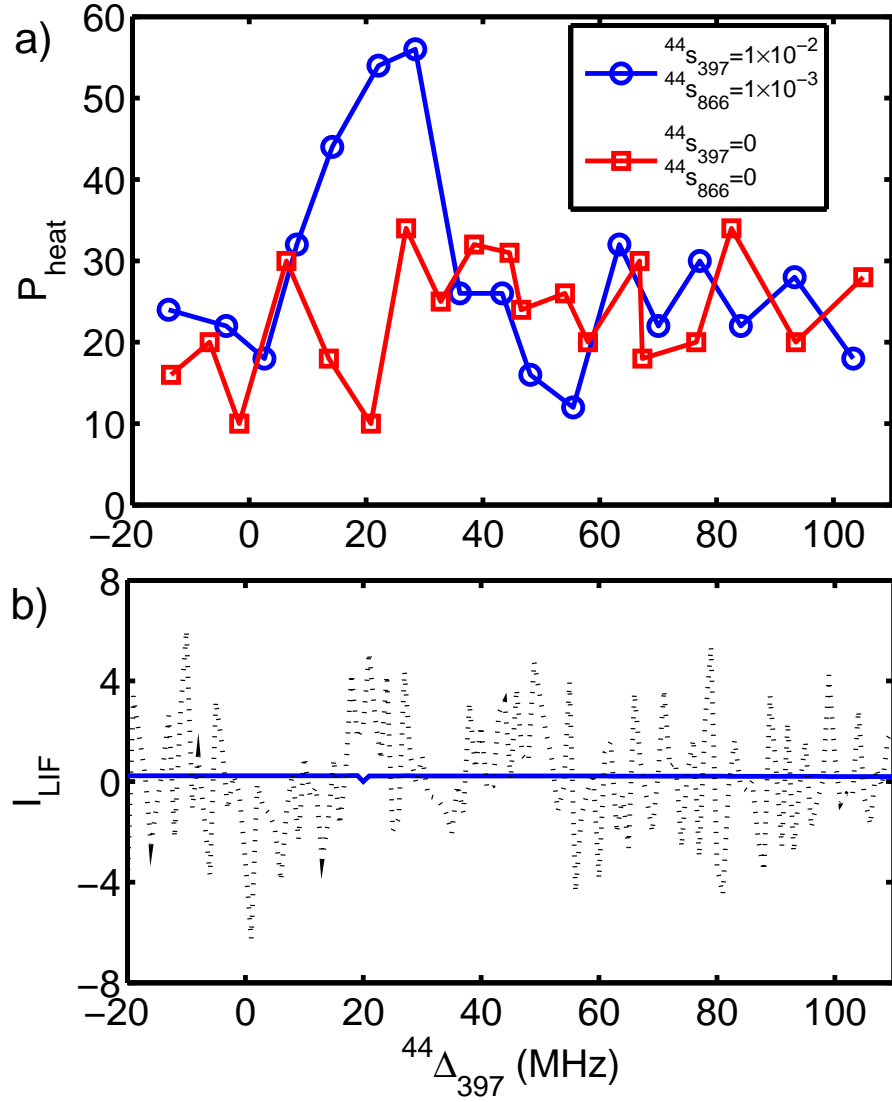


Figure 21: Comparison of a low power SHS spectra with simulated LIF signal. (a) The blue circles show a SHS spectra for $^{44}s_{397}=0.01$ and $^{44}s_{866}=1 \times 10^{-3}$ with $t_{\text{heat}}=1$ s, $t_{\text{bin}}=3$ ms, and $^{44}\Delta_{866}=20$ MHz (averaged over 20 experiments). The background P_{heat} measurements without heating lasers are shown by the red squares. Lines are to guide the eye. (b) The predicted LIF spectrum with a $t_{\text{meas}}=1.89$ s is shown in blue for comparison. The dotted black line is a simulation of the shot noise corresponding to the dark counts of the experimental device (50 counts/sec).

between 234-260 nm for comparison with high-redshift astronomical data [127]. An immediate improvement to SHS can be obtained by simply increasing the collection efficiency.

Based on these observations for a two ion Coulomb crystal, it is possible to detect the heat induced by less than 1500 scattered photons. Recent results showing significant photon scattering from SrF using two lasers to address the (0,0) and (0,1) vibrational bands of an electronic transition, together with sidebands from an electro-optic modulator (EOM) to address hyperfine structure [57], suggest that a clever choice of molecular ion can lead to similar rates. We envision an experiment in which a control loop optimizes intensities, laser frequency, and the position of EOM sidebands to maximize the radiative force that heats the Coulomb crystal. The parameter results obtained by the control loop will encode information about the internal structure of the molecular ion.

CHAPTER V

SPECTROSCOPY ON THE $S_{1/2}$ - $D_{5/2}$ OPTICAL QUBIT TRANSITION

5.1 *Introduction*

Mixtures of trapped molecular and laser-cooled atomic ions are a promising system for the study of molecular ion reactivity and spectroscopy [44, 87]. The strong optical transition of atomic ions allows for rapid cooling to millikelvin temperatures, and co-trapped molecular ions are sympathetically cooled to similar temperatures through the Coulombic interaction. Due to the wide mass acceptance of a linear Paul trap, a broad array of molecular ions have been sympathetically cooled ranging in size from HD^+ [122] to C_{60}^+ [116].

At low temperatures, the mixture forms an ordered structure known as a Coulomb crystal. The fluorescence of the laser-cooled atomic ions can be observed by a camera and the molecular ions can be inferred from the dark regions of the image. For systems where the molecular ions are known, the position of the imaged atomic ions can be compared to molecular dynamics simulations to observe reactions [43] and perform spectroscopy [85].

The fluorescence of the atomic ions is very sensitive to Doppler shifts and can be used to measure the temperature or kinetic energy of the system [104, 128]. This can also be used to detect the presence of molecular ions by exciting the motion of the trapped ions by an electric field and observing the change in total fluorescence. This method, known as laser-cooled fluorescence mass spectrometry (LCFMS) [78], can be used to follow reactions; e.g., the multi-step photodestruction of aniline cation

($\text{C}_6\text{H}_5\text{NH}_2^+$) [52]. The technique has also been combined with resonant enhanced multi-photon dissociation to accurately measure vibrational lines with sub-MHz precision [122].

For a chain of ions, the axial motion of the ions can best be described by normal modes. In the limit of two ions, LCFMS has been used to non-destructively identify a single molecular ion with a single known atomic ion by exciting the center-of-mass (COM) mode [114]. The axial normal modes have also been measured by exciting the ion motion and then Fourier transforming the autocorrelation of the fluorescence [129].

Here we use resolved sideband spectroscopy of an atomic reporter ion ($^{40}\text{Ca}^+$) to measure the normal mode frequencies of a two ion crystal to determine the mass of an unknown target ion. To calibrate our system, we examine even isotopes of Ca^+ , which we can load by selective photoionization and independently identify by spectroscopy. The method is then tested on an odd isotope of calcium, $^{43}\text{Ca}^+$, and two molecular ions, $^{40}\text{CaH}^+$ and $^{40}\text{CaO}^+$. The resolved sideband spectroscopy not only identifies the molecular ion, but serves as a first step towards high-precision molecular ion quantum logic spectroscopy [24, 130].

In this chapter we present results using the quadrupole $S_{1/2}$ - $D_{5/2}$ transition of calcium for various experiments. We start by presenting some preliminary results associated with performing resolved sideband spectroscopy of Ca^+ . Sec. 5.3 presents novel work for optically detecting dark trapped ions using the $S_{1/2}$ - $D_{5/2}$ transition.

5.2 Resolved sideband spectroscopy of Ca^+

5.2.1 Experimental

All experiments are performed in the molecular trap described in Sec. 3.3.2. Each experiment begins by loading a $^{40}\text{Ca}^+$. The $^{40}\text{Ca}^+$ ion is Doppler cooled by driving

the $S_{1/2}$ - $P_{1/2}$ transition at 397 nm and repumping from the metastable $D_{3/2}$ state with an 866 nm laser shown in Figure 10 [131]. Once cooled, the narrow $S_{1/2}$ - $D_{5/2}$ quadrupole transition and its motional sidebands are probed using a 729 nm laser [132]. The transition frequencies are listed in Table 1.

Sideband spectroscopy of the $S_{1/2}$ - $D_{5/2}$ transition is performed in a pulsed fashion and is described in Ref [132]. The following steps describe the pulse procedure:

1. **Doppler Cooling-** The ion is initialized to the ground electronic state, $S_{1/2}$, and Doppler cooled on the $S_{1/2}$ - $P_{1/2}$ dipole transition.
2. **Spin Polarization-** The ion is spin polarized to the $S_{1/2}^{m_j=-1/2}$ level by tuning the 729 nm laser to excite the $S_{1/2}^{m_j=1/2}$ - $D_{5/2}^{m_j=-3/2}$. The $D_{5/2}^{m_j=-3/2}$ state is depopulated by driving $D_{5/2}^{m_j=-3/2}$ - $P_{3/2}^{m_j=-1/2}$ using an 854 nm laser. This process is repeated k times to ensure the $S_{1/2}^{m_j=-1/2}$ state is populated (Figure 23). The 729 nm laser is pulsed for $t_{729} = 25 - 50\mu s$ and the 854 nm laser is pulsed for $t_{854} = 1\mu s$.
3. **Sideband Cooling-** The 729 nm laser is tuned to the lower motional sideband. The 854 nm laser is again used to depopulated the $D_{5/2}^{m_j=-5/2}$ state by repumping to the $P_{3/2}^{m_j=-3/2}$. Experimentally the 854 nm laser intensity is adjusted for optimum cooling results. If several normal modes of motion are to be cooled to the ground state, the tuning of the cooling laser has to be sequentially alternated between the different sidebands. This is achieved using an AOM to shift the laser frequency. This processes is repeated n times to sufficiently remove all motional quanta. The 729 nm laser is pulsed for $t_{729} = 25 - 50\mu s$ and the 854 nm laser is pulsed for $t_{854} = 1\mu s$. It is should be noted that the t_{729} is increased by 50-100 ns after each cooling cycle.

4. **Detection**- The Doppler cooling lasers at 397 nm and 866 nm are switched on and the fluorescence of the ion is monitored for $t_{meas}=1000-3000 \mu s$. Discrimination between the ion being in the $S_{1/2}$ or $D_{5/2}$ level is done by comparing the number of photon counts with a threshold value. The shelving rate is then plotted as a percentage of the experiments which fall below the threshold. The threshold is determined by comparing the distribution of photons counts with the ion dark versus bright.

The entire experiment takes 20 ms and Figure 22 shows the pulse sequence. By repeating the whole sequence 100 times, the shelved D state occupation is measured.

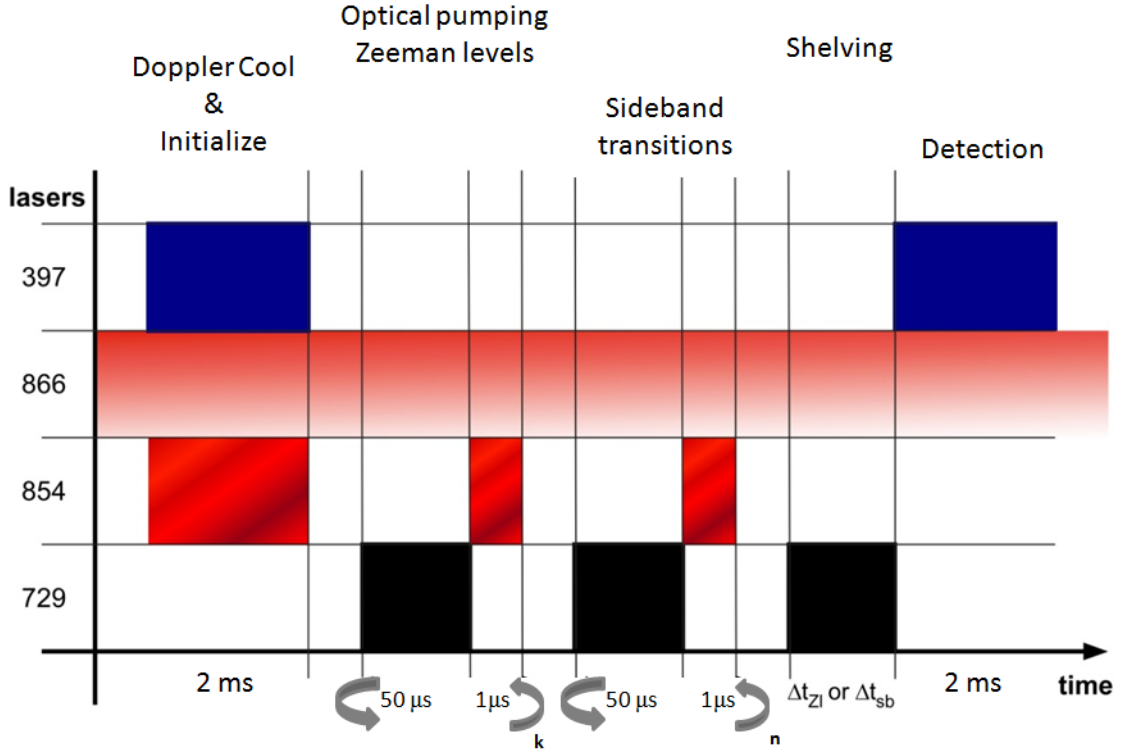


Figure 22: Typical pulse sequence for spectroscopy of the $S_{1/2}$ - $D_{5/2}$ transition.

5.2.2 Zeeman effect on $S_{1/2}$ - $D_{5/2}$ transition

One way of having quantum control of Ca^+ is by using the Zeeman sublevels of the $S_{1/2}$ - $D_{5/2}$ transition of calcium. In the presence of an external magnetic field, the

Table 3: Landé g factors for calcium

	$S_{1/2}$	$P_{1/2}$	$P_{3/2}$	$D_{3/2}$	$D_{5/2}$
g_j	2	$2/3$	$4/3$	$4/5$	$6/5$

degeneracy is lifted resulting in two separated $S_{1/2}$ sublevels and six $D_{5/2}$ sublevels (Figure 23) and splitting of this energy level is described by

$$\Delta E = g_j \mu_B B m_j \quad (36)$$

where μ_B is Bohr's magneton and g_j is the Landé factor. Table 3 is a list of the Landé factors for each of the levels in calcium and can be used to determine the energy splitting of the Zeeman levels.

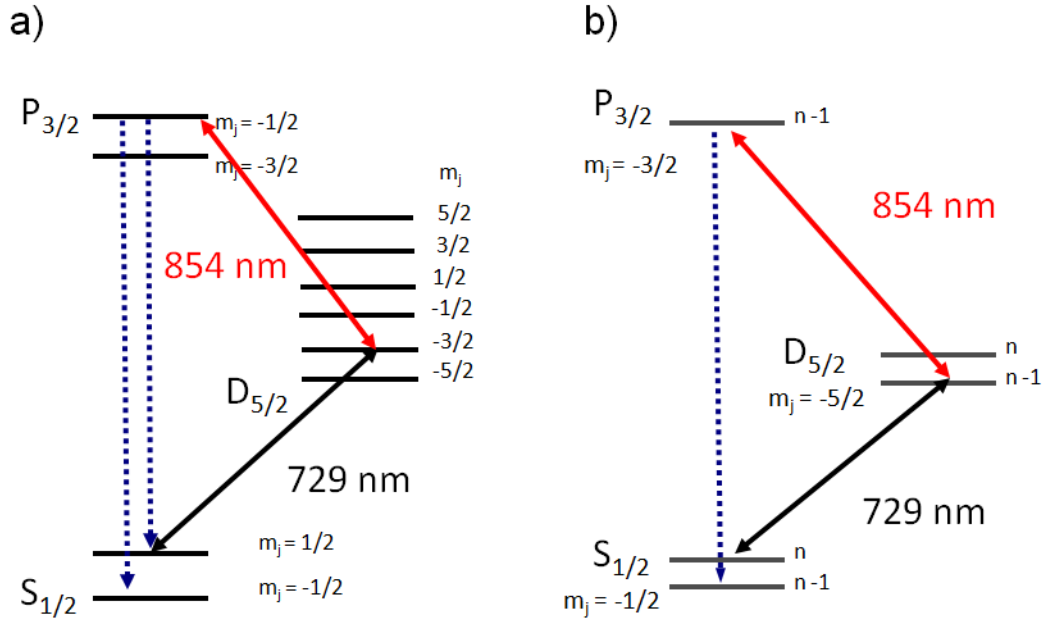


Figure 23: (a) Energy diagram of $^{40}\text{Ca}^+$ including Zeeman sublevels, and the excitation scheme demonstrating spin polarization. (b) Energy diagram include the dressed motional states after spin polarization, and the excitation scheme demonstrating sideband cooling.

In a non-zero magnetic field the Zeeman spectrum of the $S_{1/2}$ - $D_{5/2}$ transition would show all ten peaks with amplitudes proportional to the square of the Clebsch-Gordan factors. In our case, we choose to use the $S_{1/2}^{m_j=-1/2}$ - $D_{5/2}^{m_j=-5/2}$ transition for sideband

cooling and couple to the upper $P_{3/2}^{m_j=-3/2}$ level for quick decay and maximum cooling before the ion is lost from the cooling cycle. It should be noted that the selection rule for the quadrupole transition can be forced to be $\Delta m_j = \pm 2$ by fixing the polarization, $\vec{\epsilon}$, of the beam to be perpendicular to the \vec{B} field which is perpendicular to the wavevector, \vec{k} ($\vec{\epsilon} \perp \vec{B} \perp \vec{k}$). This allows for only four Zeeman sublevels to be excited. Figure 24 is an example Zeeman spectrum of the $S_{1/2}$ - $D_{5/2}$ transition obtained from our lab. It can be seen that $\vec{\epsilon}$ is not optimized because eight Zeeman lines are still visible.

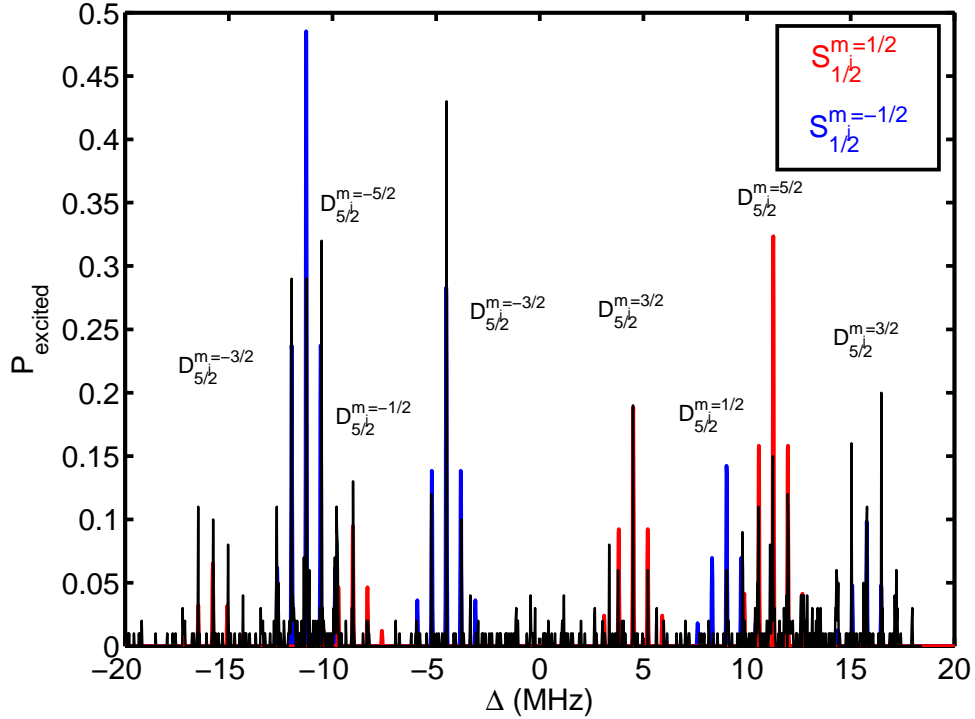


Figure 24: Zeeman spectrum of $S_{1/2}$ - $D_{5/2}$ with $\vec{B} = 3.6$ gauss $t_{729}=50 \mu\text{s}$, $t_{meas}=1000 \mu\text{s}$, $\nu_{ax} = 700$ kHz, and $\nu_{rad} = 1.4$ MHz. (black) data (red) fit to the $S_{1/2}^{m_j=1/2}$ - $D_{5/2}$ transitions (blue) fit to the $S_{1/2}^{m_j=-1/2}$ - $D_{5/2}$ transitions

As mentioned, we will focus on the $S_{1/2}^{m_j=-1/2}$ - $D_{5/2}^{m_j=-5/2}$ transition and the population in this state is maximized by spin polarizing the system into the $S_{1/2}^{m_j=-1/2}$ level. This is achieved by optically pumping the $S_{1/2}^{m_j=1/2}$ - $D_{5/2}^{m_j=-3/2}$ transition shown

in Figure 23, and ensures that before the experiment is started the spin population is initialized in the $S_{1/2}^{m_j=-1/2}$ state. Figure 25 shows spectra of the motional sidebands of the $S_{1/2}^{m_j=-1/2}$ - $D_{5/2}^{m_j=-5/2}$ transition with and without spin polarizing the state.

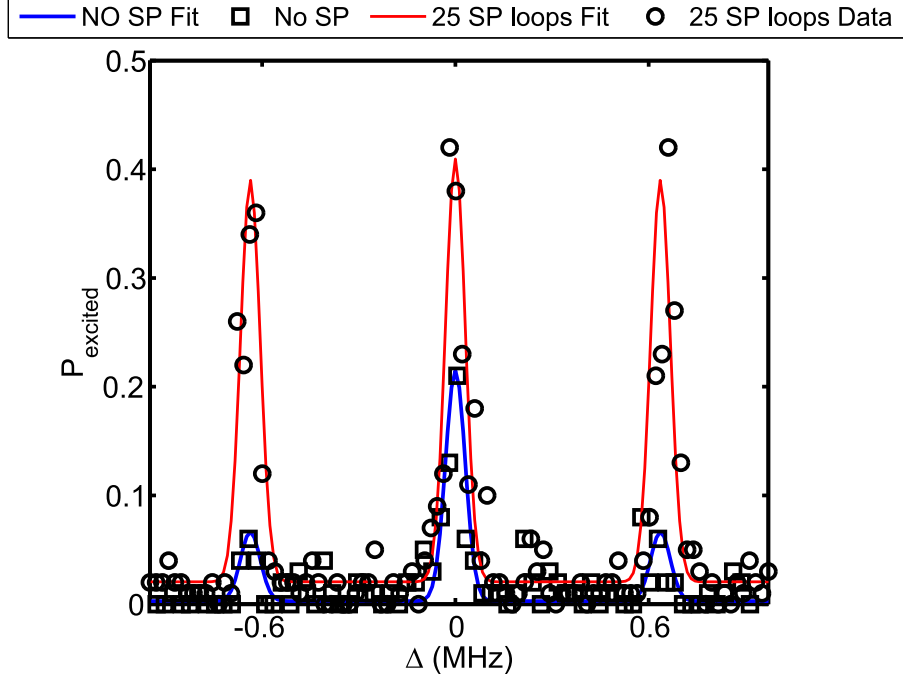


Figure 25: Sideband spectra of the $S_{1/2}^{m_j=-1/2}$ - $D_{5/2}^{m_j=-5/2}$ transition before and after optical pumping the $S_{1/2}^{m_j=1/2}$ - $D_{5/2}^{m_j=-3/2}$ transition. $t_{729}=50 \mu\text{s}$, $t_{meas}=2000 \mu\text{s}$. The blue line corresponds to the fit of the black squares which was with the Spin Polarization (SP) loops set to zero. The red line is the fit of black circles after 25 SP loops. Each peak was fit to a Gaussian.

5.2.3 Sideband measurement, cooling and coherent dynamics

To measure the resolved motional sidebands of the $S_{1/2}^{m_j=-1/2}$ - $D_{5/2}^{m_j=-5/2}$ transition we scan a double-passed AOM with 1 kHz steps. Figure 26 is an example of a sideband spectrum of the $S_{1/2}^{m_j=-1/2}$ - $D_{5/2}^{m_j=-5/2}$ transition without spin polarizing or sideband cooling. It should be noted that this spectrum is Fourier limited and to measure narrow linewidth requires reducing the laser power and exciting for a longer time (t_{729}). One motivation for measuring narrow lines is to measure the slow drift of the laser frequency. Figure 27 is a plot of the carrier transition over the course of

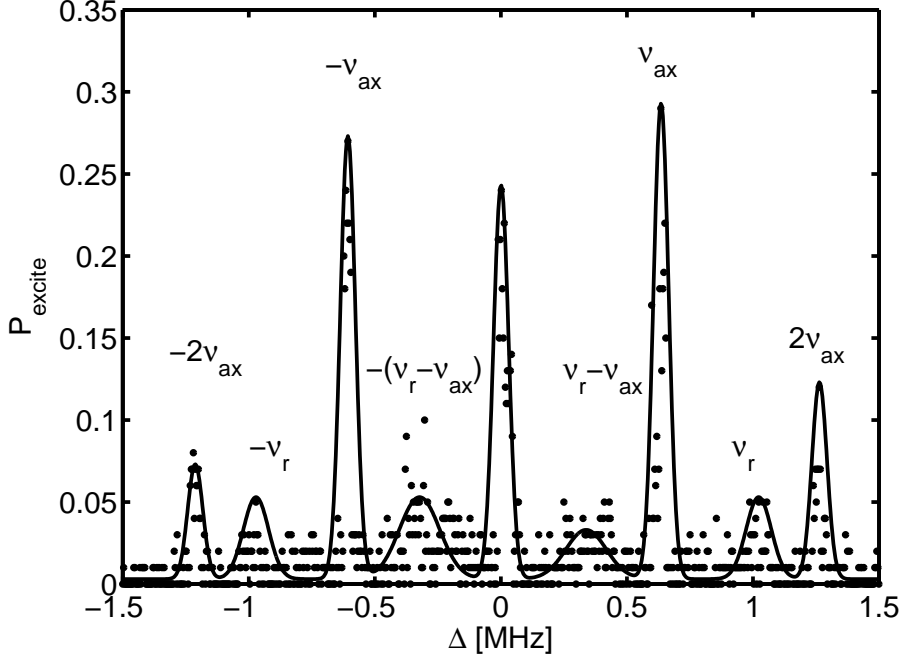


Figure 26: Resolved sideband spectrum of $S_{1/2}^{m_j=-1/2}-D_{5/2}^{m_j=-5/2}$ ($t_{729}=46 \mu\text{s}$, $t_{meas}=2000 \mu\text{s}$, $\nu_{ax} = 600 \text{ kHz}$ and $\nu_r = 1 \text{ MHz}$).

seven hours and it shows that the laser frequency drifts 10 kHz over four hours. It was determined that over the course of one experiment, correction of the frequency drift is unnecessary but is achievable using software to shift the AOM frequency. Measuring narrow spectral lines sets an upper bound to the linewidth of the excitation laser and allows an estimate of the short-term stability of the magnetic field and the trap frequency. We determined that the upper bound of the laser linewidth is 10 kHz.

It has been shown that the motional sidebands can be measured, and after sideband cooling the ion can be put into a pure state ($\langle n \rangle = 0$ state) [99]. Following the pulse sequence in Figure 22, and addressing the lower motional sideband as shown in Figure 23, the ion can be cooled below the Doppler limit. The ground state occupation is determined by probing absorption on the lower and upper motional sidebands

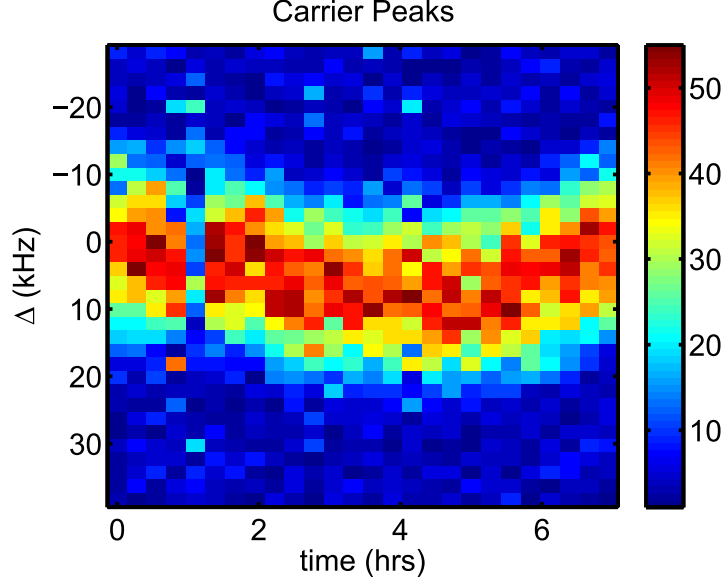


Figure 27: Carrier $S_{1/2}^{m_j=-1/2}$ - $D_{5/2}^{m_j=-5/2}$ transition over a 7 hour period to map the drift of the laser. It appears that the frequency drifts 10 kHz over four hours ($t_{729}=46 \mu s$, $t_{meas}=2000 \mu s$). The color scale shows the shelving rate.

immediately after cooling pulses. Figure 28 shows an example of the first order axial motional sidebands and carrier before and after sideband cooling. The motional sideband occupation number was extracted by observing the motional dephasing of the carrier Rabi transition (Figure 29) after Doppler and sideband cooling. These experiments were fit using

$$\Omega_{carrier} = \Omega(1 - \eta^2 n) \quad (37)$$

where Ω is the overall coupling strength and η is the Lamb-Dicke parameter, and assuming the occupation number is a Boltzmann distribution, which explains the decoherence of our system. For a detailed derivation of coherent dynamics of the carrier and lower and upper motional sidebands see Ref. [99]. It was determined that after Doppler cooling, the ion was still at a much higher occupation number than expected from Doppler cooling. It is assumed that due to power broadening of the $S_{1/2}$ - $P_{1/2}$ transition, the Doppler limit was not achieved. It has been suggested that if

a magnetic field is greater than 4 gauss the $S_{1/2}$ - $P_{1/2}$ transition will also be broadened resulting in less efficient Doppler cooling [99]. For an axial trap frequency of 700 kHz, one would expect to have $\langle n \rangle = 16$, but from fitting the coherent dynamics it was determined that $\langle n \rangle = 40$, and after sideband cooling $\langle n \rangle = 8$, which is below the Doppler limit. We expect that with an increase in the laser intensity the ion could be cooled to the motional ground state. For the experiments presented, only $325 \mu W$ (beam waist = $70 \mu m$) of 729 nm laser power was available, which limits the maximum number of sideband cooling cycles that can be performed before the trap heating rate becomes comparable to the cooling rate ($\approx \eta \Omega$).

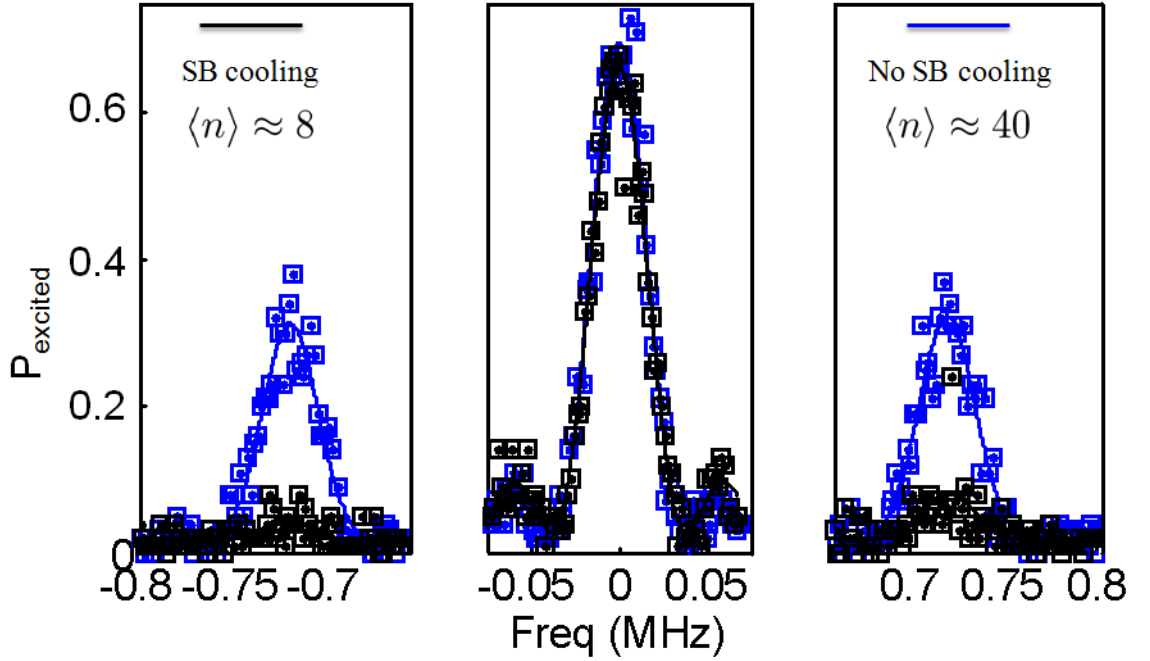


Figure 28: First order axial motional sideband of the $S_{1/2}^{m_j=-1/2}$ - $D_{5/2}^{m_j=-5/2}$ transition. (Blue) After Doppler cooling (Black) After 100 sideband cooling cycles ($t_{729}=50 \mu s$, $t_{meas}=2000 \mu s$, $\nu_{ax}=700$ kHz)

If more than one vibrational mode is to be cooled, the cooling lasers have to be cycled between each of the lower motional sidebands. This has yet to be achieved in our lab, but it has been demonstrated by many groups. The literature shows that it is

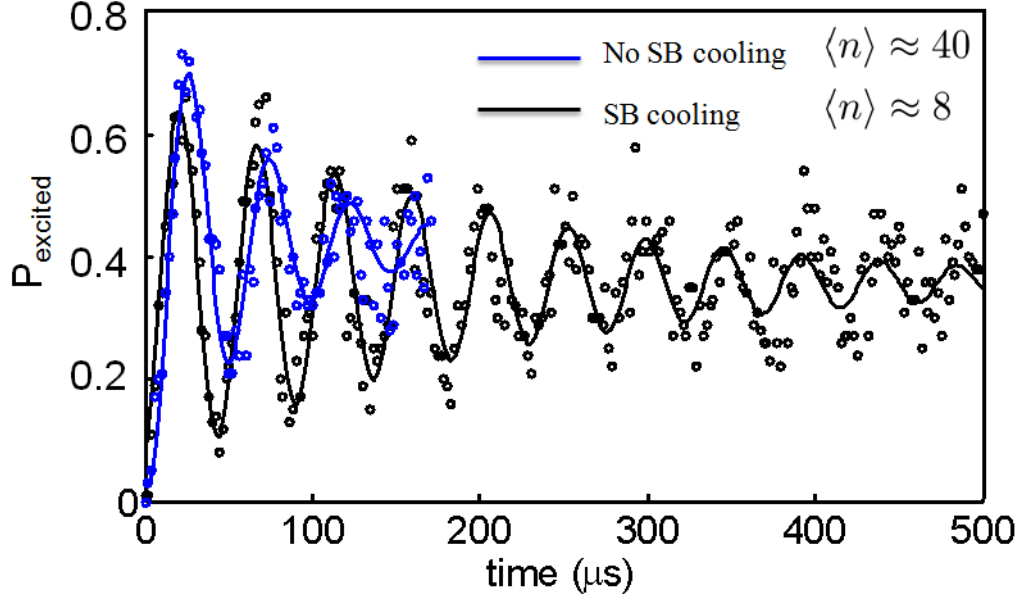


Figure 29: Carrier Rabi dynamics of $S_{1/2}^{m_j=-1/2}$ - $D_{5/2}^{m_j=-5/2}$ transition. (Blue) After Doppler cooling. Coherence time of $60 \mu s$ (Black) After 100 sideband cooling cycles. Coherence time of $230 \mu s$ $t_{729}=50 \mu s$, $t_{meas}=2000 \mu s$, $\nu_{ax}=700$ kHz

more efficient to cycle between modes instead of cooling one motional mode completely and then jumping to the next [99]. This is to avoid re-heating of the first motional mode, which was already cooled. Our results could be improved with some simple experimental improvements. These include improving the Doppler precooling so the population in the motional modes is closer to the Doppler limit. Also, increasing the intensity of the 729 nm laser by reducing the beam waist or increasing the optical power would lead to an increase in the Rabi frequency, which leads to more optical pumping cycles before a loss of coherence.

5.3 Resolved sideband mass spectrometry

5.3.1 Experimental

With the basics of measuring the sideband spectrum of calcium presented, we can discuss the detection of a second, unknown ion via the coupled motion of the two ion

Coulomb crystal. As shown in the Chapter 2, the mass of an ion in a trap can be determined by the secular harmonic motion of the ion. When two ions are trapped the mass can still be determined by comparing the axial normal mode frequencies of the two ion system via

$$\nu_{\pm}^2 = [(1 + \mu) \pm \sqrt{1 - \mu + \mu^2}] \nu_1^2, \quad (38)$$

where μ is the mass ratio of $^{40}\text{Ca}^+$ to the unknown ion, ν_1 is the axial secular frequency of a single $^{40}\text{Ca}^+$, and ν_- and ν_+ are the center-of-mass (COM) mode and breathing mode (BM), respectively. [114].

The target ions investigated are four isotopes of calcium: $^{42}\text{Ca}^+$, $^{43}\text{Ca}^+$, $^{44}\text{Ca}^+$, and $^{48}\text{Ca}^+$, and two molecular ions: $^{40}\text{CaH}^+$ and $^{40}\text{Ca}^{16}\text{O}^+$. For the molecular ion experiments, two $^{40}\text{Ca}^+$ ions are loaded into the trap and Doppler cooled. Hydrogen or oxygen is introduced into the chamber using a manual leak valve (Kurt J. Lesker VZLVM267). The background pressure is increased to 1×10^{-8} torr until one of the two ions reacts without shifting the position of the bright ion [114]. The leak valve is then shut and the experiment is started when the chamber has returned to its base pressure. Figure 30 is a CCD image depicting the process of loading calcium and then reacting to form a molecular ion.

5.3.2 Resolved sideband mass spectrometry

Figure 31 shows the resolved sideband spectrum of the $S_{1/2}^{m_j=1/2}$ - $D_{5/2}^{m_j=5/2}$ line of two $^{40}\text{Ca}^+$ ions. For each AOM frequency step, the shelving experiment is performed 100 times to determine a population. The total spectrum is taken 10 times and the average is reported. The sidebands can be identified as the center-of-mass mode

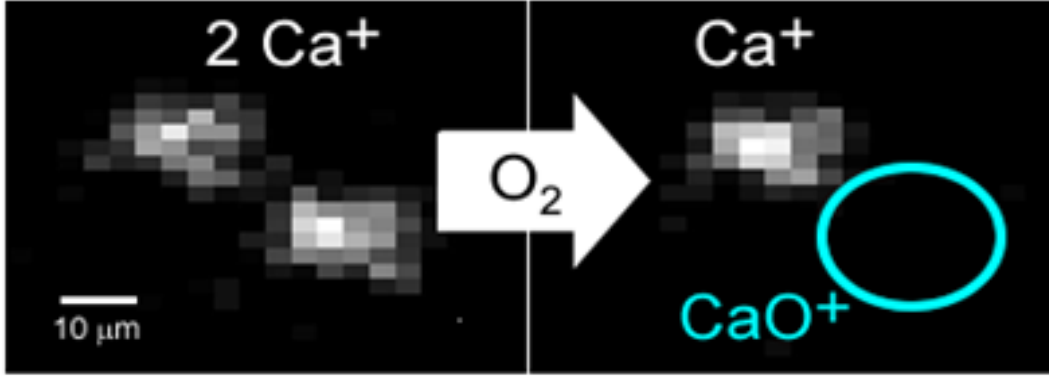


Figure 30: CCD image of calcium and calcium oxide ions

(COM), the radial mode (R), and the breathing mode (BM). Harmonics of these modes and combinations can also be identified.

To determine the mass, we choose to use the frequencies of the COM/BM modes. This determination requires the accurate measurement of the COM/BM modes for two $^{40}\text{Ca}^+$ and then for the $^{40}\text{Ca}^+ - X^+$ system. This was done by independently fitting the carrier and the positive and negative first-order sidebands of the the COM/BM modes to Gaussians. The difference between the center and the sidebands was used to calculate the COM/BM frequencies. Figure 32 shows the first-order red COM sideband for $^{40}\text{Ca}^+$ with all seven target ions. This figure clearly shows that as the mass of the target ion increases the secular frequency decreases.

From the measured sideband frequencies, Equation 38 is used to calculate the mass of the target ion. Values were calculated for both red and blue sidebands independently, and then averaged. All values were found to be consistent with one another. These results were then compared to the values found in Ref. [133] and are included in Tables 4 and 5. Good agreement is seen for the ions within 4 amu of $^{40}\text{Ca}^+$. It is hypothesized that the sharp decrease in accuracy for the two ions outside of this range stems from the addition of a stray DC electric field. If a stray field pushed the ion off the rf null which is out of the plane of view of the imaging optics the method

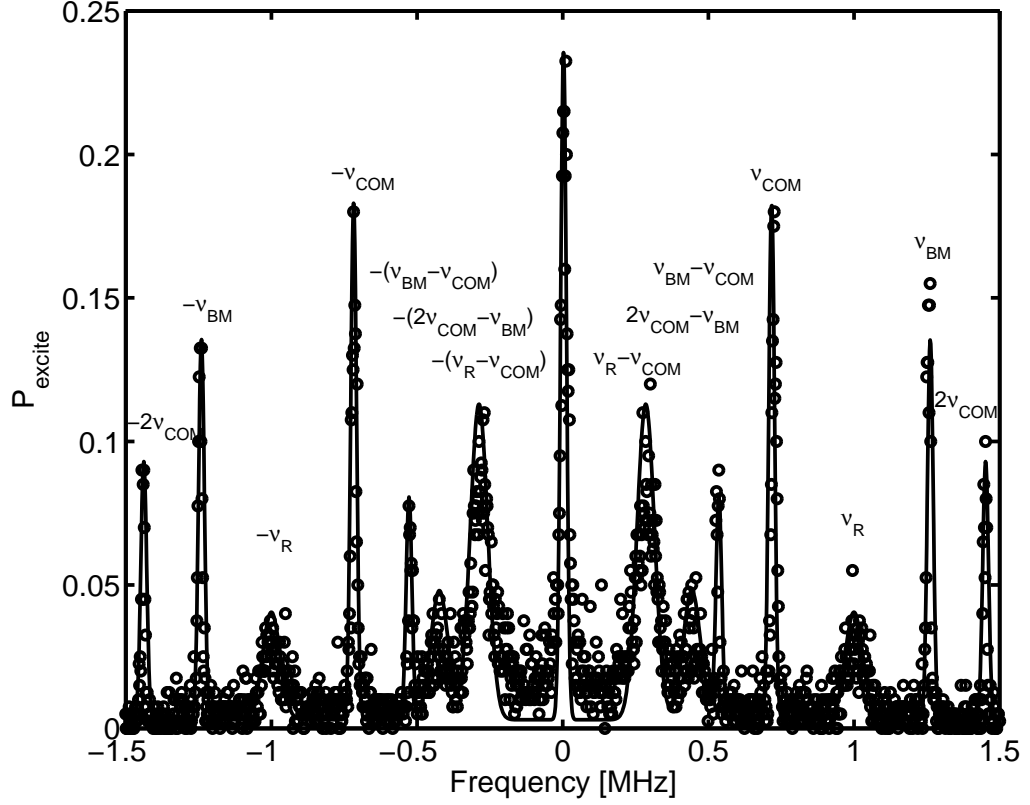


Figure 31: Frequency scan of two laser cooled $^{40}\text{Ca}^+$ ions with identified peaks. In addition to the carrier a series of sideband peaks are visible corresponding to the center-of-mass mode (ν_{COM}), the radial mode (ν_{R}), the breathing mode (ν_{BOM}), and combinations of these modes ($t_{729}=200\ \mu\text{s}$, $t_{\text{meas}}=3000\ \mu\text{s}$).

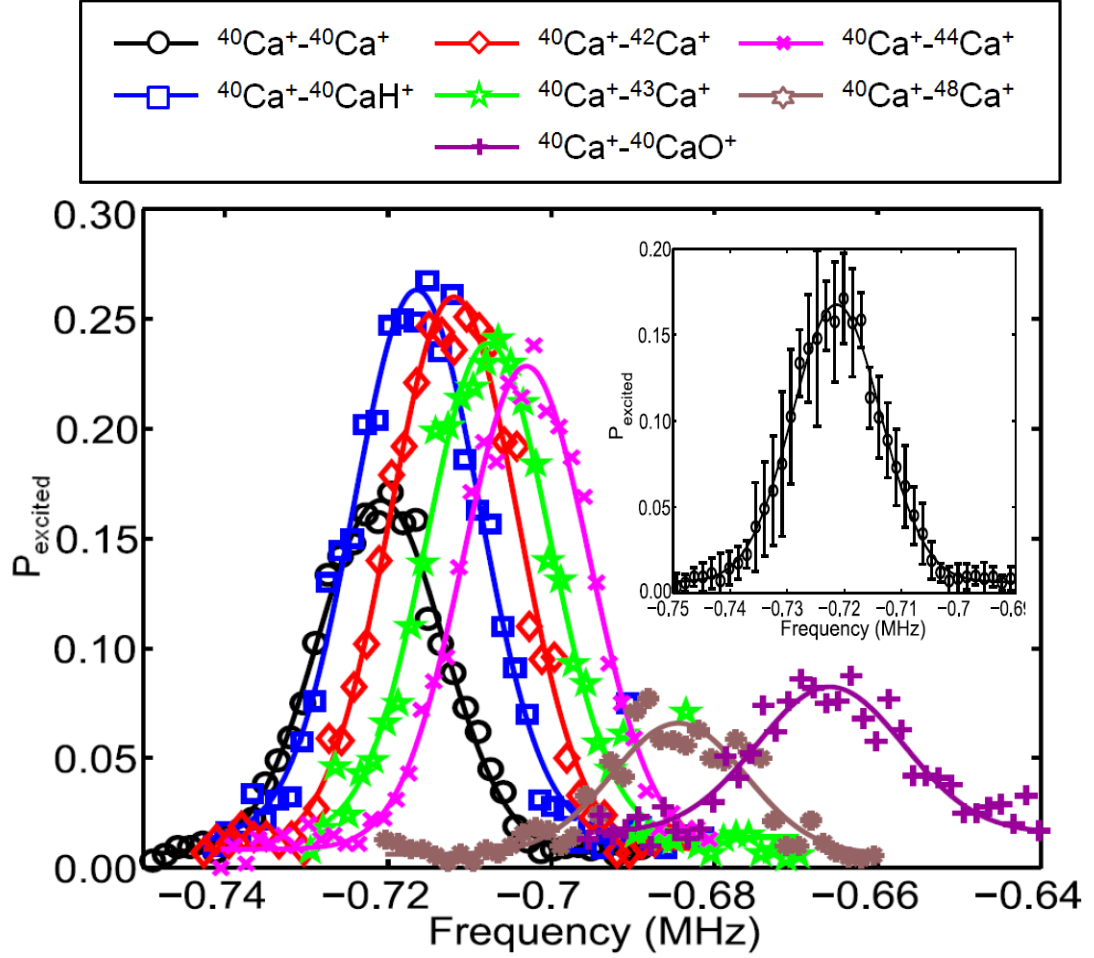


Figure 32: Center-of-mass frequency scan of the first order red sideband of a laser cooled $^{40}\text{Ca}^+$ with one of the following second ions: $^{40}\text{Ca}^+$, $^{40}\text{CaH}^+$, $^{42}\text{Ca}^+$, $^{43}\text{Ca}^+$, $^{44}\text{Ca}^+$, $^{48}\text{Ca}^+$, $^{40}\text{CaO}^+$ ($t_{729}=200$, $t_{\text{meas}}=3000$)

Table 4: Comparison of theoretical and experimental measured secular frequencies

Ion	Calculated COM Sec. Freq.(MHz)	Measured COM Sec. Freq.(MHz)	Calculated BM Sec. Freq.(MHz)	Measured BM Sec. Freq.(MHz)
$^{40}\text{Ca}^+$	0.7212	0.7212(3)	1.2492	1.2481(8)
$^{40}\text{CaH}^+$	0.7167	0.7167(4)	1.2415	1.241(1)
$^{42}\text{Ca}^+$	0.7122	0.7122(8)	1.2344	1.2359(8)
$^{43}\text{Ca}^+$	0.7078	0.7077(5)	1.2276	1.235(1)
$^{44}\text{Ca}^+$	0.7034	0.7032(5)	1.2212	1.229(1)
$^{48}\text{Ca}^+$	0.6863	0.6846(7)	1.1984	1.24(2)
$^{40}\text{CaO}^+$	0.6539	0.661(6)	1.1643	1.240(6)

Table 5: Comparison of theoretical and experimental measured masses without considering the stray field

Ion	CRC mass (amu)	Experimental Mass (amu)	$\frac{\Delta\mu}{\mu}$
$^{40}\text{Ca}^+$	39.963	39.96(+5/-6)	**
$^{40}\text{CaH}^+$	40.970	40.98(+10/-9)	-1.21×10^{-4}
$^{42}\text{Ca}^+$	41.959	41.98(+16/-17)	-5.41×10^{-4}
$^{43}\text{Ca}^+$	42.959	42.99(+11/-9)	-6.18×10^{-4}
$^{44}\text{Ca}^+$	43.955	44.02(+11/-11)	-1.49×10^{-3}
$^{48}\text{Ca}^+$	47.953	48.36(+15/-17)	-8.48×10^{-3}
$^{40}\text{CaO}^+$	55.958	52.98(+64/-65)	5.63×10^{-2}

in Ref. [92] is unusable for detecting micromotion, requiring a more sophisticated method observing the motional sidebands. This method of compensation is described in Ref. [23] but has yet to be achieved in our setup.

As the mass gets larger, the relative strength of the coupling to the stray field mixes the radial and axial modes, changing the expected normal mode frequencies. Figure 33 is a plot of the measured COM/BM frequencies along with the expected frequencies using Equation 38 and the value fit to an additional stray DC field. According to the fit there is an additional field of approximately 77.5 mV/mm. We can also see in Table 6 that including the stray field dramatically improves the uncertainty in the experimental mass, especially for the higher mass values.

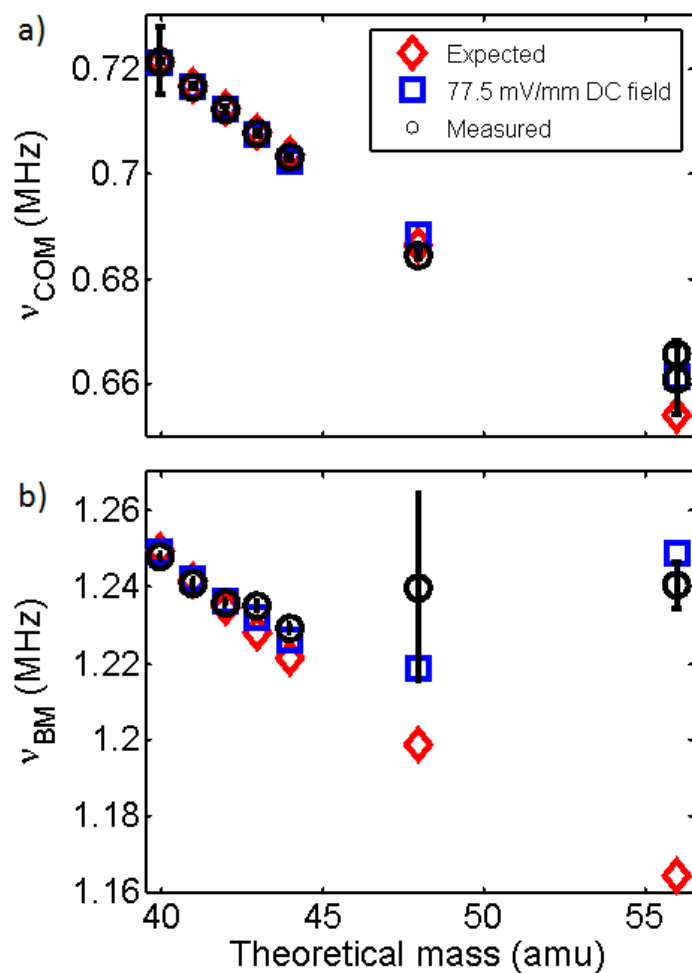


Figure 33: Experimental secular frequency (black) compared with the expected secular frequency from Equation 38 (red) and the addition of a 77.5 mV/mm DC stray field (blue). (a) COM (b) BM

Table 6: Comparison of theoretical and experimental measured masses considering the stray field

Ion	CRC mass (amu)	Experimental Mass (amu)	$\frac{\Delta\mu}{\mu}$
$^{40}\text{Ca}^+$	39.963	39.96(+5/-6)	**
$^{40}\text{CaH}^+$	40.970	40.97(+10/-8)	1.02×10^{-5}
$^{42}\text{Ca}^+$	41.959	41.96(+19/-18)	-3.29×10^{-5}
$^{43}\text{Ca}^+$	42.959	42.95(+11/-8)	2.04×10^{-4}
$^{44}\text{Ca}^+$	43.955	43.83(+8/-4)	2.86×10^{-3}
$^{48}\text{Ca}^+$	47.953	48.25(+19/-9)	-6.37×10^{-3}
$^{40}\text{CaO}^+$	55.958	55.96(+64/-65)	-4.46×10^{-5}

Based on these results, I would conclude that with additional compensation using the method outlined in Ref. [23] we will have developed a very accurate optical mass spectrometry technique easily resolving a one amu mass difference. This method could be used for confirmation of the mass of an expected molecular ion before performing spectroscopy. It should also be stated that the symmetric error in the secular frequency measurements leads to an asymmetric error in the mass (Tables 5 and 6) due to the nonlinear relationship of the mass to secular frequency, which can be seen in Equation 38.

5.4 Conclusion

In this chapter we have demonstrated the use of the $S_{1/2}$ - $D_{5/2}$ optical qubit transition to measure the Zeeman spectrum and motional sidebands of calcium. Using these techniques, we are able to cool the ion's motion below the Doppler limit, and with a few improvements to the experimental setup, we should be able to cool to the motional ground state, $T \approx 10 \mu\text{K}$. Such improvements include increasing the intensity of the 729 nm laser, stabilizing the magnetic field, and improving the lock stability.

This chapter has also introduced a new optical technique that uses the motional sidebands to measure the charge to mass ratio of singly charged calcium isotopes, CaH^+ , and CaO^+ . We have determined that with the current experimental setup, we

can measure changes of 1 amu, despite the trap not being compensated. Again, with some simple experimental improvements this technique could be a sensitive probe of molecular mass.

Combining the improvements to both the cooling and the compensation, we expect to sympathetically ground state cool a molecular ion. If achieved, this would lead to a translational kinetic energy of a molecular ion in the μK regime. Also, we hope to study even smaller mass ratios. The mass difference between $^{40}\text{CaD}^+$ and $^{42}\text{Ca}^+$ is 0.01807 amu, which in our setup equates to an approximately 80 Hz shift. We are not currently able to see this small of a shift, but since the $S_{1/2}$ - $D_{5/2}$ transition is on the order of a single Hertz it is achievable with improvements to our laser lock, and magnetic field stabilization. Sideband cooling could also improve this result, making resolved sideband mass spectrometry comparable to other high resolution mass spectrometry techniques. Additionally, these techniques are the initial steps necessary to perform quantum logic spectroscopy and SHS on molecular ions.

CHAPTER VI

RESOURCE REQUIREMENTS FOR FAULT-TOLERANT QUANTUM SIMULATION: THE TRANSVERSE ISING MODEL GROUND STATE

This chapter is based on

Craig R. Clark, Tzvetan S. Metodi, Samuel D. Gasster, and Kenneth R. Brown
Phys. Rev. A, **79**, 062314 (2009).

6.1 *Introduction*

The calculation of the basic properties of quantum systems (eigenstates and eigenvalues) remains a challenging problem for computational science. One of the most significant issues is the exponential scaling of the computational resource requirements with the number of particles and degrees of freedom, which for even a small number of particles (~ 100) exceeds the capabilities of current computer systems. In 1982 R. Feynman addressed this problem by proposing that it may be possible to use one quantum system as the basis for the simulation of another [64]. This was the early promise of quantum simulation, and one of the original motivations for quantum computing. Since that time, many researchers have investigated different approaches to quantum simulation [134, 135, 136, 137, 138, 139]. For example, D. Abrams and S. Lloyd have proposed a quantum algorithm for the efficient computation of eigenvalues and eigenvectors using a quantum computer [136]. Many of the investigations into quantum simulation have assumed ideal performance from the underlying components resulting in optimistic estimates for the quantum computer

resource requirements (number of qubits and time to completion). It is well known, however, that in order to address the effects of decoherence and other sources of faults and errors in the implementation of qubits and gates it is necessary to incorporate fault-tolerant quantum error correction into an estimate of the resource requirements.

In this paper we estimate the resource requirements for a quantum simulation of the ground state energy for the 1-D quantum Transverse Ising Model, specifically incorporating the impact of fault-tolerant quantum error correction. We apply the general approach of D. Abrams and S. Lloyd [135, 136], and compute estimates for the total number of physical qubits and computational time as a function of the number of particles (N) and required numerical precision (M) in the estimate of the ground state energy.

We have chosen to study the resource requirements for computing the ground state energy for the 1-D quantum TIM since this model is well studied in the literature and has an analytical solution [140, 141, 142]. The relevant details of the TIM are summarized in Sec. 6.2. In Sec. 6.3, we map the calculation of the TIM ground state energy onto a quantum phase estimation circuit that includes the effects of fault-tolerant quantum error correction. The required unitary transformations are decomposed into one qubit gates and two-qubit controlled-not gates using gate identities and the Trotter formula. The one-qubit gates are approximated by a set of gates which can be executed fault-tolerantly using the Solovay-Kitaev theorem [143]. In Sec. 6.3.3, the quantum circuit is mapped onto the Quantum Logic Array (QLA) architecture model, previously described by Metodi, *et al.*[144]. Our final results, utilizing the QLA architecture, are given in Sec. 6.3.4 and a discussion of how improving the state of the art in the underlying technology affects the performance for executing the TIM problem. In Sec. 6.4, we extend our resource estimate from 1-D to higher dimensions. In Sec. V, we compare our present results for the TIM quantum

simulation with a previous analysis of the resource requirements for Shor’s factoring algorithm [60, 144]. Finally, our conclusions are presented in Sec. 6.6.

The QLA was originally developed based on the performance capabilities of ion trap qubit technology and consists of a set of interconnected traps. The architecture model may be applied to any two-dimensional array of qubits where the qubits are physically moved between locations on a time scale comparable to, or longer than, the time to execute a single qubit gate operation.

6.2 *Transverse Ising model*

The 1-D Transverse Ising Model is one of the simplest models exhibiting a quantum phase transition at zero temperature [140, 145, 146, 141]. The calculation of the ground state energy of the TIM varies from analytically solvable in the linear case [140] to computationally inefficient for frustrated 2-D lattices [147]. For example, the calculation of the magnetic behavior of frustrated Ising antiferromagnets requires computationally intensive Monte-Carlo simulations [148]. Given the difficulty of the generic problem and the centrality of the TIM to studies of quantum phase transitions and quantum annealing, the TIM is a good benchmark model for quantum computation studies.

The Transverse Ising Model consists of N -spin-1/2 particles with nearest-neighbor spin-spin interactions along the z -axis in the presence of an external magnetic field along the x -axis. The Hamiltonian, H_I , for this system is:

$$H_I = \sum_i \Gamma \sigma_i^x + \sum_{\langle i,j \rangle} J_{ij} \sigma_i^z \sigma_j^z, \quad (39)$$

where J is the spin-spin interaction energy, Γ is the energy of a spin in the external magnetic field, and $\langle i,j \rangle$ implies a sum only over nearest-neighbors [141]. σ_i^x and σ_i^z are the Pauli spin operators for the i th spin, and we set $\hbar = 1$ throughout this paper.

In present work we focus on the 1-D linear chain TIM of N -spins with constant Ising interaction energy $J_{ij} = -J$. The ground state of the system is determined by the ratio of $g = \Gamma/J$. For the large magnetic field case, $g \gg 1$ the system is paramagnetic with all the spins aligned along the \hat{x} axis, and in the limit of small magnetic field, $g \ll 1$, the system has two degenerate ferromagnetic ground states, parallel and anti-parallel to the \hat{z} axis. In the intermediate range of magnetic field strength the linear 1-D TIM exhibits a quantum phase transition at $g = 1$ [141].

The TIM Hamiltonian in Equation 39, for the 1-D case with constant coupling can be rewritten as:

$$H_I = -J \left(\sum_{j=1}^N g X_j + \sum_{j=1}^{N-1} Z_j Z_{j+1} \right) \quad (40)$$

where the Pauli spin operators, σ_j^x and σ_j^z , are replaced with their corresponding matrix operators X_j and Z_j . For the 1-D TIM, the ground state energy can be calculated analytically in the limit of large N [140]. In the case of a finite number of spins with non-uniform spin-spin interactions (J not constant), it is possible to efficiently simulate the TIM using either the Monte-Carlo method [149] or the density matrix renormalization group approach [142]. The challenge for classical computers comes from the 2-D TIM on a frustrated lattice where the simulation scales exponentially with N . Applying the quantum phase estimation circuit to calculate the ground state energy of the TIM requires physical qubit resources, which scale polynomially with N , and the number of computational time steps is also polynomial in N . In addition, just as the complexity of the problem is independent of the lattice dimension and layout when applying classical brute force diagonalization, the amount of resources required to apply the quantum phase estimation circuit is largely independent of the dimensionality of the TIM Hamiltonian.

6.3 TIM quantum simulation resource estimates

Our approach to estimating the resource requirements for the TIM ground-state energy calculation with Hamiltonian H_I involves two steps. First, we follow the approach of D. Abrams and S. Lloyd and map the problem of computing the eigenvalues of the TIM Hamiltonian in Equation 40 onto a phase estimation quantum circuit [135, 136]. Second, we decompose each operation in the phase estimation circuit into a set of universal gates that can be implemented fault-tolerantly within the context of the QLA architecture. This allows us an accurate estimate of the resources in a fault-tolerant environment.

6.3.1 Phase estimation circuit

The phase estimation algorithm calculates an M -bit estimate of the phase ϕ of the eigenvalue $e^{-i2\pi\phi}$ of the time evolution unitary operator $U(\tau) = e^{-iH_I\tau}$ for fixed τ given an eigenvector of H_I . $\phi < 1$ and can be represented by the binary fraction $0.x_1 \dots x_M$ [135, 136]. The energy eigenvalue $E = \frac{2\pi\phi}{\tau}$ when $E\tau < 2\pi$. Calculation of the ground state energy $|E_g|$ requires that $\tau < 2\pi/|E_g|$. For the 1-D TIM, the magnitude of the ground-state energy $|E_g|$ is bounded by $NJ(1+g)$ [140]. In the region near the phase transition $g \approx 1$, we choose $\tau = (10JN)^{-1}$.

The quantum circuit for implementing the phase estimation algorithm is shown in Figure 34. The circuit consists of two quantum registers: an N -qubit input quantum register prepared in an initial quantum state $|\Psi\rangle$, and an output quantum register consisting of a single qubit recycled M times [150, 151]. Each of the N qubits in the input register corresponds to one of the N spin-1/2 particles in the TIM model [152]. At the beginning of each of the M steps in the algorithm, the output qubit is prepared into the state $\frac{1}{\sqrt{2}}(|0\rangle + |1\rangle)$ using a Hadamard (H) gate. The H gate is

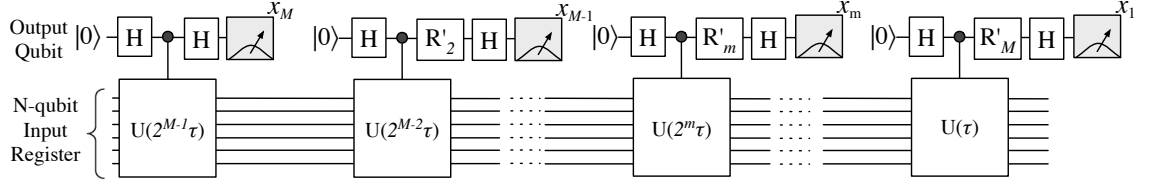


Figure 34: The circuit for implementing the phase estimation algorithm using one continuously recycled control qubit.

followed by a controlled power of $U(\tau)$, denoted with $U(2^m\tau)$, applied on the input register, where $0 \leq m \leq M - 1$.

Letting j denote to the j th step in the circuit, each time the output qubit is measured (meter symbols) the result is in the m th bit in the estimate of ϕ , following the rotation of the output qubit via the gate:

$$R_j = |0\rangle\langle 0| + \exp\left(i\pi \sum_{m=M+2-j}^M \frac{2^{M+1}x_m}{2^{m+j}}\right) |1\rangle\langle 1| \quad (41)$$

where the gate R_j corresponds to the application of the Quantum Fourier Transform on the output qubit at each step [150, 151]. The result after each of the M measurements is an M -bit binary string $\{x_1x_2 \dots x_M\}$, which corresponds the M -bit approximation of ϕ given by $0.x_1 \dots x_M$. Using this estimate of ϕ , the corresponding energy eigenvalue $E = \frac{2\pi\phi}{\tau}$ will be the ground-state energy E_g with probability equal to $|\langle \Psi | \Psi_g \rangle|^2$ [135], where $|\Psi_g\rangle$ is the ground eigenstate of H_I .

To maximize the probability of success $|\langle \Psi | \Psi_g \rangle|^2$, the initial quantum state $|\Psi\rangle$ should be an approximation of the ground state $|\Psi_g\rangle$. For arbitrary Hamiltonians the preparation of an approximation to $|\Psi_g\rangle$ is generally computationally difficult [153, 154]. For certain cases, the preparation can be accomplished using classical approximation techniques to calculate an estimated wavefunction or adiabatic quantum state preparation techniques [152, 138]. If the state can be prepared adiabatically, the resource requirements for preparing $|\Psi\rangle$ are comparable in complexity to the resource requirements for implementing the circuit for the phase estimation algorithm shown in Figure 34 [152]. For this reason, we focus our analysis on estimating the number

of computational time steps and qubits required to implement the circuit, assuming that the input register has been already prepared in the N -qubit quantum state $|\Psi\rangle$.

6.3.2 Decomposition of quantum circuit into fault-tolerant gates

Figure 34 in Sec. 6.3.1 shows the TIM circuit at a high-level, involving $N + 1$ unitary operators. In this section, each unitary operation of the circuit is decomposed into a set of basic one and two qubit gates which can be implemented fault-tolerantly using the QLA architecture. The set of basic gates used is

$$\{X, Z, H, T, S, \text{CNOT}, \text{MEASURE}\} \quad (42)$$

where **MEASURE** is a single qubit measurement in the \hat{z} basis, **CNOT** denotes the two-qubit controlled-NOT gate, and T and S gates are single-qubit rotations around the \hat{z} -axis by $\pi/4$ and $\pi/2$ radians respectively. The high-level circuit operations which require decomposition are the controlled- $U(2^m\tau)$ gates and each R_j gate.

The Controlled- $U(2^m\tau)$ gate can be decomposed using the second-order Trotter formula [155, 156]. First, H_I is broken into two terms: $H_X = \sum_{j=0}^N gX_j$, representing the transverse magnetic field, and $H_{ZZ} = \sum_{j=0}^{N-1} Z_j Z_{j+1}$, representing the Ising interactions. By considering the related unitary operators

$$U_x(2\tau) = \prod_{j=1}^N \exp(-ig\tau X_j) \quad (43)$$

$$U_{zz}(2\tau) = \prod_{j=1}^{N-1} \exp(-i\tau Z_j Z_{j+1}), \quad (44)$$

and setting $g = 1$ (as discussed in Sec. 6.2), we can construct the Trotter approximation of $U(2^m\tau)$, denoted by $\tilde{U}(2^m\tau)$ as:

$$\begin{aligned} U(2^m\tau) &= [U_x(\theta) U_{zz}(2\theta) U_x(\theta)]^k + \epsilon_T \\ &= \tilde{U}(2^m\tau) + \epsilon_T, \end{aligned} \quad (45)$$

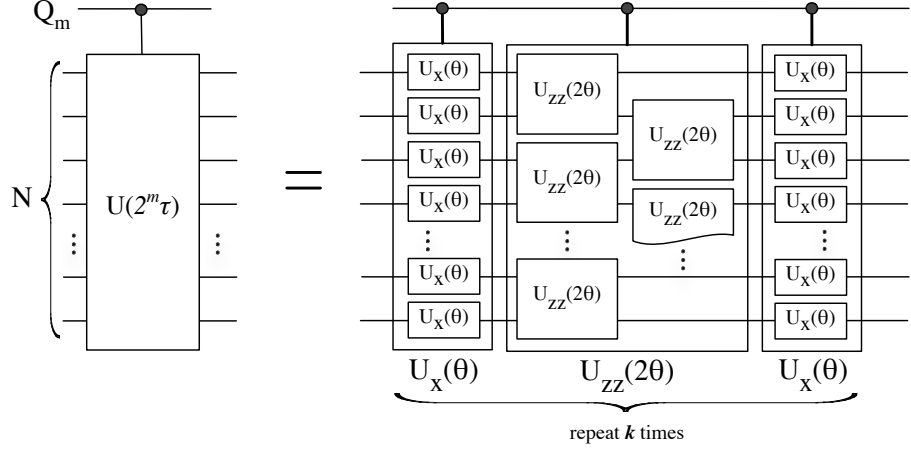


Figure 35: Circuit for the controlled unitary operation $U(2^m\tau)$ approximated using the Trotter formula.

where $\theta = (2^m\tau/k)$ and ϵ_T is the Trotter approximation error, which scales as $\mathcal{O}\left(\frac{(2^m\tau)^3}{k^2}\right)$ [155]. The Trotter approximation error can be made arbitrarily small by increasing the integer Trotter parameter k . Since the controlled- $U(2^m\tau)$ corresponds to the $(M - m)$ th bit, ϵ_T must be less than $1/2^{M-m}$, which is the precision of the $(M - m)$ th measured bit in the binary fraction for the phase ϕ . Thus, when approximating $U(2^m\tau)$, k is increased until ϵ_T is less than $1/2^{M-m}$. For a given M , we estimate a numerical value for the Trotter parameter $k(m = 0) = k_0$ as a function of $N \leq 10$, with the constraint that $\epsilon_T < 1/2^M$. We thus find that for fixed M , k_0 scales as $1/N$. We extrapolate k_0 for larger N based on a power-law fit of $N \leq 10$. For $m > 0$, we set $k = 2^m k_0$, which will satisfy the error bound based on the scaling of ϵ_T with k .

The circuit corresponding to the Trotter approximation of $U(2^m\tau)$ is shown in Figure 35, where it can be seen that the controlled- $U(2^m\tau)$ is composed of two controlled- $U_x(\theta)$ operations and a controlled- $U_{zz}(\theta)$ operation, repeated k times and controlled on the m th instance of the output qubit denoted with Q_m . Expanding the circuit in Figure 35, we can express $\tilde{U}(2^m\tau)$ as:

$$\tilde{U}(2^m\tau) = U_x(\theta) [U_{zz}(2\theta)U_x(2\theta)]^{k-1} U_{zz}(2\theta) U_x(\theta), \quad (46)$$

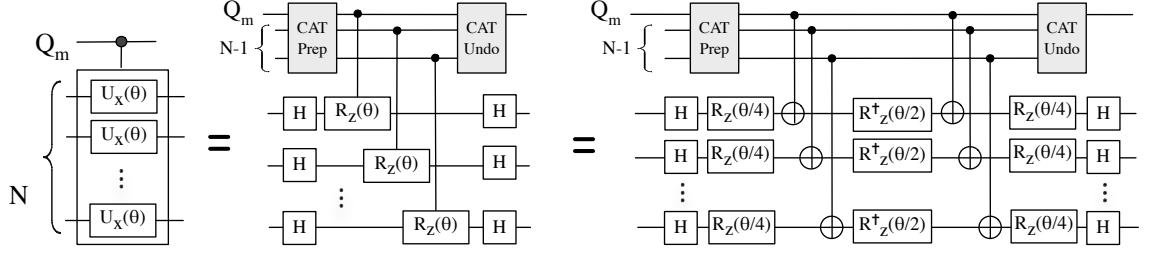


Figure 36: The decomposition of the controlled unitary operation $U_x(\theta)$ into single-qubit R_z gates and CNOT gates.

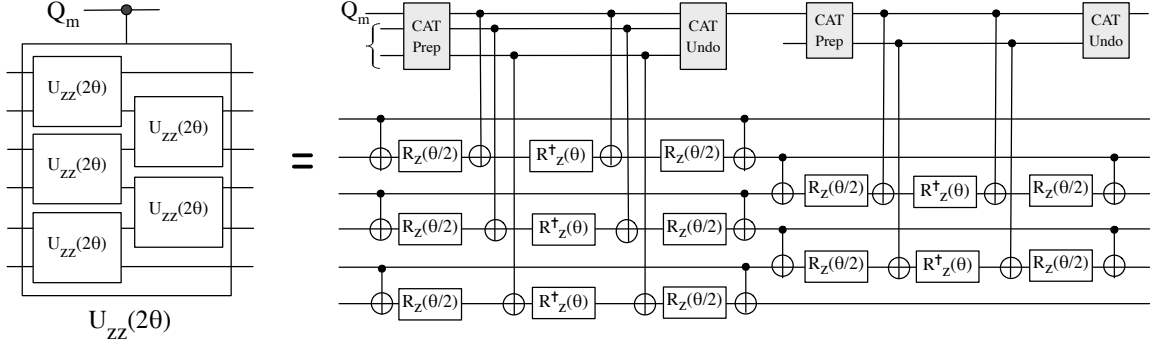


Figure 37: The decomposition of the controlled unitary operation $U_{zz}(2\theta)$ gate into single-qubit R_z gates and CNOT gates.

which shows that, approximating $U(2^m\tau)$ will require the sequential implementation of k controlled- $U_{zz}(2\theta)$ gates, $(k-1)$ controlled- $U_x(2\theta)$ gates, and two instances of controlled- $U_x(\theta)$ gates, all controlled on the m th instance of the output qubit.

The quantum circuits for the decomposition of the controlled- $U_x(2\theta)$ and controlled- $U_{zz}(2\theta)$ gates are shown in Figure 36 and 37, respectively. The gates are decomposed into rotations about the \hat{z} -axis, $R_z(\theta) = \exp(-i\frac{\theta}{2}Z)$ and CNOT gates. $(N-1)$ additional qubits are used to prepare an N -qubit cat state in order to parallelize each of the N $R_z(\theta)$ gates. The preparation of an N -qubit cat state requires $(N-1)$ CNOT gates, which can be implemented in $\mathcal{O}(N)$ time steps in parallel with the $R_z(\theta/4)$ gates in Figure 36 and in parallel with the $R_z(\theta/2)$ gates in Figure 37.

The three single-qubit R_z gates ($R_z(\theta)$, $R_z(\theta/2)$, and $R_z(\theta/4)$) can be approximated using $\mathcal{O}(\log^{3.97}(1/\epsilon_{sk}))$ basics gates (H, T, S) by the Solovay-Kitaev theorem

[143, 157]. The Solovay-Kitaev error (ϵ_{sk}) is equivalent to a small rotation applied to the qubit. The algorithm of Dawson and Nielsen [157] is used to compute the sequence of H , T , and S gates required to approximate each of the three R_z gates for $\theta = \frac{2^m \tau}{k}$. We define S_R as the length of the longest of these three sequences. For $M=30$, for example, we find that $S_R = 4 \times 10^5$, requiring a sixth order Solovay-Kitaev approximation [157]. The results of this calculation show that the Solovay-Kitaev error $\epsilon_{sk} < \frac{\epsilon_T}{k}$, in order that the total error, ϵ_T is less than the required precision ($1/2^{M-m}$), when we approximate $U(2^m \tau)$. As a result S_R scales as $\mathcal{O}(\log^{3.97}(k/\epsilon_T)) = \mathcal{O}(M^{3.97})$.

We now have a complete decomposition of the controlled- $U(2^m \tau)$ into the basic gates given in Equation 42. As a function of S_R , the number of time steps required to implement controlled- $U_x(\theta)$ and $U_{zz}(\theta)$ is equal to $(3S_R + 4)$, and $(6S_R + 7)$, respectively. Following Equation 46, the number of time steps required to implement the entire controlled- $U(2^m \tau)$ is $k(9S_R + 11) + 3S_R + 4$, where $k = 2^m k_0$. Each R_j gate in Figure 34 is equivalent to at most a rotation by $R_z(\theta)$ and requires less than S_R gates.

Putting all of the above together, the total number of time steps (K) required to implement the TIM circuit as a function of S_R , k_0 , and M is given by:

$$\begin{aligned} K &= \sum_{m=0}^{M-1} [2^m k_0 (9S_R + 11) + 3S_R + 4 + S_R] \\ &= \mathcal{O}(2^M) \times S_R. \end{aligned} \tag{47}$$

Since S_R scales as $\mathcal{O}(M^{3.97})$, the total number of time steps is dominated by the exponential dependence on the precision (M). The number of qubits Q required to implement the circuit is $2N$, since N qubits are needed for the input register $|\Psi\rangle$, one qubit is needed for the output register, and $N - 1$ qubits are needed for the cat state.

In the next section we include fault-tolerant QEC into our circuit model and determine the resulting resource requirements, K and Q . We also provide an estimate on how long it could take to implement the TIM problem in real-time by taking into

account the underlying physical implementation of each gate and qubit in the context of the QLA architecture.

6.3.3 Mapping onto the QLA architecture

Incorporating quantum error correction and fault-tolerance [158, 159, 160, 161] into the TIM circuit design will impact the resource requirements in two ways. First, each of the qubits becomes a *logical qubit*, that is encoded into a state using a number of lower-level qubits. Second, each gate becomes a *logical gate*, realized via a circuit composed of lower-level gates applied on the lower-level qubits that make-up a logical qubit. Each lower-level qubit may itself be a logical qubit all the way down to the physical level. Thus, quantum error correction and fault-tolerance increases the number of physical time steps and qubits required to implement each basic gate and may even require additional logical qubits, depending on how each gate is implemented fault-tolerantly and the choice of error correcting code. The resource requirements necessary to implement encoded logical qubits and gates will depend on the performance parameters of the underlying physical technology, the type of error correcting code used, and the level of reliability required per logical operation. The physical technology performance parameters that are taken into account in the design of the QLA architecture are the physical gate implementation reliability, time to execute a physical gate, and the time it takes for the state of the physical qubits to decohere.

The QLA architecture [144] is a tile-based, homogeneous quantum computer architecture based on ion trap technology, employing 2-D surface electrode trap structures [61, 162, 163]. Each tile represents a single computational unit capable of storing two logical qubits and executing fault-tolerantly any logical gate from the basic gate set given in Equation 42. One of the key features of the QLA architecture is the teleportation-based logical interconnect which enables logical qubit exchange between

any two computational tiles. The interconnect uses the entanglement-swapping protocol [164] to enable logical qubit communication without adding any overhead to the number of time required to implement a quantum circuit [144].

The QLA was originally designed to factor 1024-bit integers [144]. This requirement resulted in the need to employ the second order concatenated Steane $[[7, 1, 3]]$ quantum error correcting code [165]. Second order concatenation means that each logical qubit is a level 2 qubit, composed of 7 level 1 logical qubits each encoded into the state of 7 physical ion-trap qubits.

To estimate the reliability for executing each of the basic-gates fault-tolerantly, a lower-bound of 3.1×10^{-6} for the fault-tolerant threshold of the $[[7, 1, 3]]$ code. This value was derived by Metodi, *et al.* [166], by analysis of the ion-trap-based geometrical layout of each logical qubit tile. The $[[7, 1, 3]]$ code threshold value used in the current research differs from the previously published estimate of 1.8×10^{-5} [167] due to our more detailed account of the operations specific to the ion trap technology in the implementation of each logical qubit [166]. These threshold results are combined with Gottesman's method for including qubit movement [168] to estimate the reliability for each logical operation at levels 1 and 2.

Since each qubit in the $[[7, 1, 3]]$ code moves an average of 10 steps during error correction [166], we find that each level 1 gate has a failure probability of 3.2×10^{-10} and each level 2 gate has a failure probability of 3.5×10^{-14} . In our failure probability estimates, we have assumed optimistic physical ion trap gate error probabilities of 10^{-7} per physical operation, consistent with recent ion-trap literature [169]. We also determine the physical resources required for each logical qubit. Each level 1 qubit requires 21 ion-trap qubits (7 data qubits and 14 ancilla to facilitate error correction) and each level 2 qubit requires 21 level 1 qubits. Given that the duration of each physical operation on an ion-trap device is currently on the order $10 \mu\text{s}$ [170, 171],

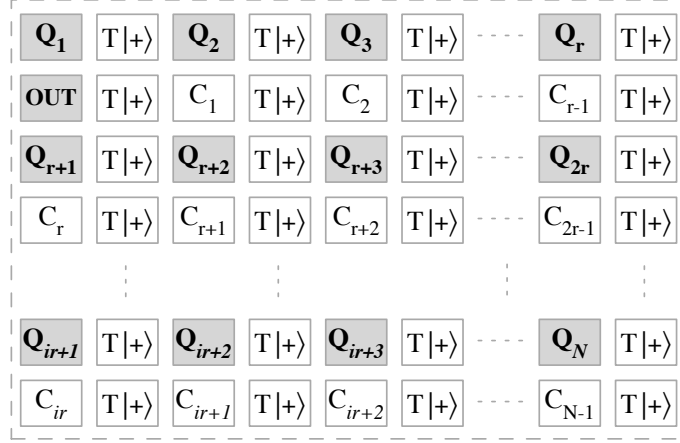


Figure 38: QLA architecture for the TIM problem

the time required to complete a single error correction step is approximately 1.6 ms at level 1 and 0.26 seconds at level 2.

The number of logical qubits Q directly maps to the number of computational tiles required by the QLA, allowing us to estimate the size of the physical system. Similarly, the number of time steps K maps directly to the time required to implement the application since the duration of a single time step in the QLA architecture is defined as the time required to perform error correction, as discussed in Ref. [144]. We define an aggregated metric KQ called the problem size equal to $K \times Q$, which is an upper bound on the total number of logical gates executed during the computation [172]. The inverse of the problem size, $1/KQ$, is the maximum failure probability allowed in the execution of a logical gate [172], which ensures that the algorithm completes execution at least 36% of the time. Taking into consideration the failure probabilities per logical gate, the maximum problem size KQ which can be implemented in the QLA architecture is 3.1×10^9 at level 1 error correction, 3×10^{13} at level 2, and 2.8×10^{20} at level 3. Level 3 error correction is not described in the design of the QLA architecture, however, its implementation is possible since a level 3 qubit is simply a collection of level 2 qubits and the architecture design does not change. The estimated failure probability for each level 3 logical gate is 3.6×10^{-21} .

The parameters K and Q for the TIM problem were estimated in Sec. 6.3.2, where Q was found to be $2N$ and K is $\mathcal{O}(2^M) \times S_R$. The fault-tolerant implementation of the T gate, however, requires an auxiliary logical qubit prepared into the state $T|+\rangle$ for one time step followed by four time steps composed of H , CNOT, S , and MEASURE gates [173], causing the value of K and Q to increase. Since many of the gates in the Solovay-Kitaev sequences approximating the R_z gates are T gates, when calculating K using Equation 47, the value of S_R must take into consideration the increased number of cycles for each T gate. All other basic gates are implemented transversally and require only one time step.

The resulting functional layout for the QLA architecture for the TIM problem is shown in Figure 38. The architecture consists of $4N$ logical qubit tiles. The tiles labeled with Q_1 through Q_N are the data tiles which hold the logical qubits used in the N -qubit input register $|\Psi\rangle$ and the “OUT” tile is for the output register. The tiles labeled with C_1 through C_{N-1} are the $N - 1$ qubit tiles for the cat state. The $T|+\rangle$ tiles are for the preparation of the auxiliary states in the event that T gates are applied on any of the data qubits. All tiles are specifically arranged as shown in Figure 38 in order to minimize the communication required for each logical CNOT gate between the control and target qubits. For example, when preparing the cat state using all C_i tiles and the “OUT” tile, CNOT gates are required only between the “OUT” tile, C_1 , and C_r . Similarly, C_1 interacts via a CNOT gate only with C_2 , while C_2 interacts only with Q_3 , during the cat state preparation.

6.3.4 Resource estimates for the 1-D TIM problem

The resource requirements for implementing the 1-D TIM problem using the QLA architecture are given in Figure 39, where we show a logarithmic plot of the number of time steps K (calculated using Equation 47) as a function of the energy precision $M \leq 20$, assuming $N = 100$. The figure clearly shows K ’s exponential dependence

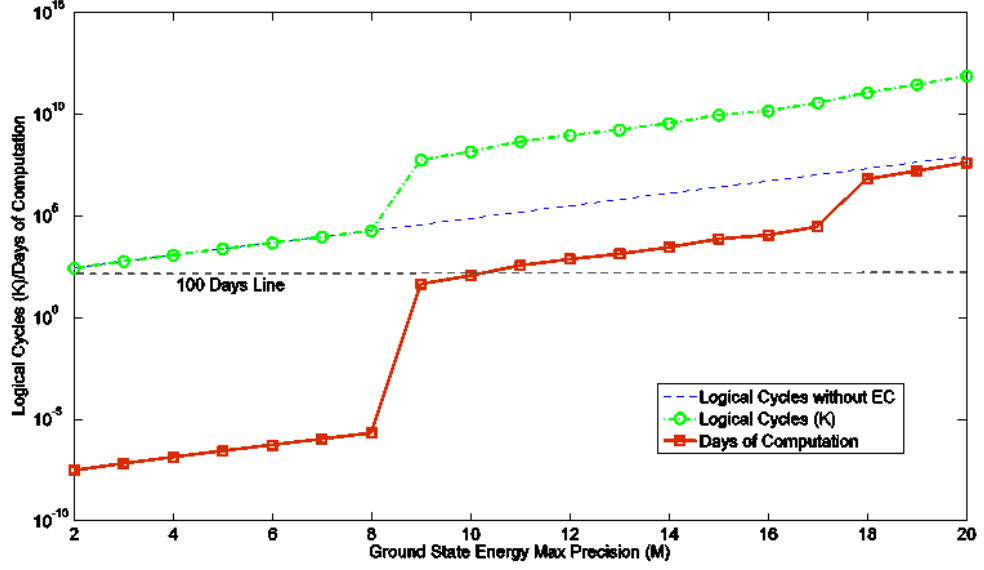


Figure 39: Numerical calculations for the number of logical cycles K (solid line) and days of computation necessary assuming $N = 100$ spin TIM problem as a function of the desired maximum precision $M \leq 20$.

on M . The dependence of K on the number of spins (N) is negligible and appears only in the k_0 term in Equation 47 as $\mathcal{O}(1/N)$, as discussed in Sec. 6.3.2. In fact, since $Q = 4N$, we expect very little increase in the value of the total problem size KQ as N increases.

We see that for $M \leq 8$ no error correction is required. This is because the required reliability per gate of $1/KQ$ is still below the physical ion-trap gate reliability of 1×10^{-7} . Without error correction, the architecture is composed entirely of physical qubits and all gates are physical gates. This means that each single-qubit R_z gate can be implemented directly without the need to approximate it using the Solvay-Kitaev theorem, resulting in $S_R = 1$ in Equation 47, and the total number of qubits becomes $2N$ instead of $4N$. For $M \geq 9$ error correction is required, resulting in a sudden jump in the number of timesteps at $M = 9$, with an additional scaling factor of $\mathcal{O}(M^4)$ in K due to S_R 's dependence on M . In fact, K increases so quickly that at $M = 9$ that level 2 error correction is required instead of level 1. At $M \geq 18$ level 3 error

correction is required and while there is no increase in K , each time step is much longer, so there is a jump in the number of days of computation. The Solovay-Kitaev order [157] for $M = 9$ is three and increases to order five for $M = 20$.

6.3.5 Discussion of the resource estimates

Our resource estimates for the 1-D TIM problem indicate that multiple levels of error correction, even for modest precision requirements, results in long computational times. As shown in Figure 39, it takes longer than 100 days, even for $M = 7$, when level 2 error correction is required. When level 3 error correction is required the estimated time is greater than 7.5×10^3 years.

The number of logical cycles K , which grows exponentially with M , contributes to the long computational times. However, the primary factor contributing to the long computational time is the time it takes to implement a single logical gate using error correction. Presently, it is difficult to see how one might reduce the value of K short of implementing a different approach for solving quantum simulation problems. On the other hand, the logical gate time can be improved by implementing small changes in three parameters: decreasing the physical gate time t_p , increasing the threshold failure probability p_{th} , and decreasing the underlying physical failure probability p_0 .

The effect of these three parameters on the overall computational time for the 1-D TIM problem is shown in Figure 40. The figure shows how the total time, in days, for $M = 18$ varies as we improve each of the three parameters by a factor of 2 during each of the 10 iterations shown. The starting values for each parameter in the figure are 3.1×10^{-6} for p_{th} , 10^{-7} for p_0 and $10 \mu s$ for t_p . Decreasing the physical failure probability and increasing the threshold values by a factor of 2 during each iteration causes the number of days to decrease quadratically whenever lower error correction level is required, otherwise the number of days remains constant from one iteration to the next. A single change in the error correction level from level 3 to level 2 occurs

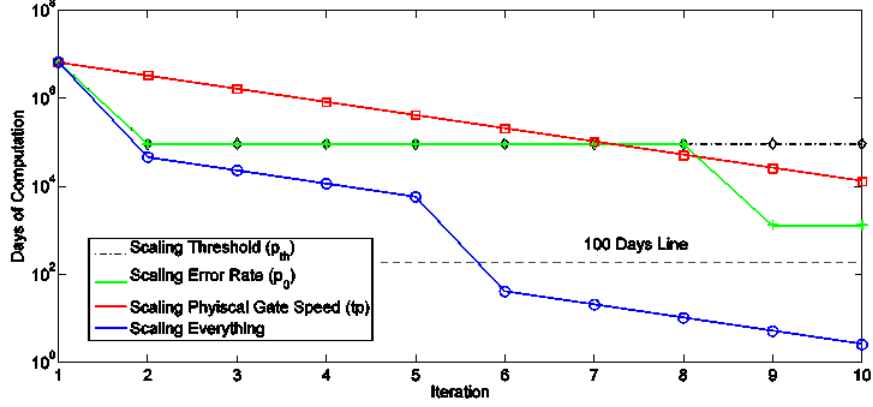


Figure 40: The total computation time in days as we vary the physical cycle time t_p (square markers), physical failure probability p_0 (starred markers), threshold failure probability p_{th} (diamond markers), and all together (circular markers) by a factor of two over 10 iterations.

by increasing p_{th} by a factor of 2 but there is no gain from additional increases in the threshold alone. Decreasing only p_0 by a factor of 512 yields a reduction of two levels of error correction.

From this analysis, we see that in order to reach a computational time on the order of 100 days with only level 1 error correction, we need to achieve parameter values of $p_{th} = 1 \times 10^{-4}$, $p_0 = 3 \times 10^{-9}$, and $t_p = 300$ ns, or better. This provides goals for the improvement in the device technologies necessary for quantum simulation. It should also be noted that these parameters are not completely independent and improvements in one of them may result in improvements in the others. For example, improving the physical failure probability may lead to better threshold failure probability by allowing some of the underlying operations to be weighted against one another. Similarly, improving the threshold failure probability may require choosing a more efficient quantum error correcting code which could have a fundamentally shorter logical time.

6.4 *Generalizing to higher spatial dimensions*

The 1-D TIM ground state energy can be efficiently computed using classical computing resources by taking advantage of the linear geometry of the spin configuration and significantly reducing the effective state space to a polynomial in N [142]. A 2-D TIM with ferromagnetic and antiferromagnetic Ising couplings can be difficult to solve due to spin frustration. Many reductions to this problem still yield an exponential number of states with near degenerate energy [147]. As a result, the problem size scales exponentially with the size of the lattice. In contrast, the implementation of the quantum phase estimation circuit in Figure 34 is independent of the values of Γ_i and J_{ij} and is weakly dependent on the geometry of the N spin system. This suggests that, given an approximation of the ground state, the TIM ground state energy can be calculated for systems with random couplings [174] or higher dimensions with similar computational resources. Consider, for example, the calculation of the ground state energy for the 2-D Villain's model [175] using the phase estimation circuit.

Villain's model is a 2-D square lattice Ising model with N^2 spin sites in which the rows have all ferromagnetic coupling and the columns alternate between ferromagnetic and antiferromagnetic. Each of the N^2 sites in Villain's model are represented by N^2 qubits in a $N \times N$ grid. The only change to the circuit for the phase estimation algorithm is the application of U_{zz} Ising interaction, which must be decomposed into two successive steps. First the rows of spin states are treated as the 1-D TIM problem in parallel, followed by the columns. Since the U_{zz} operations within each step are done in parallel, we still require $N/2$ additional qubits for the cat-states. Given that the remaining operations, including the Quantum Fourier Transform implementation, remain the same, the increase in the number of time steps to implement an N^2 -spin 2-D TIM problem, compared to the 1-D TIM problem, is by less than a factor of two.

Similarly, the increase in the resource requirements between a 1-D and a 3-D TIM problem will be by less than a factor of three.

6.5 *Comparison with factoring*

Since the QLA architecture was initially evaluated in the context of Shor’s quantum factoring algorithm [60], it would be interesting to consider how the resource requirements for implementing the TIM problem compare to those for implementing the factoring algorithm. In this section, we compare the implementation of the two applications on the QLA architecture and highlight some important differences between each application.

Even though both applications employ the phase estimation algorithm, there are several important differences. First, the precision requirements are different. For Shor’s quantum factoring algorithm, the precision M must scale linearly with the size N of the N -bit number being factored [60], where $N \geq 1024$ for modern cryptosystems. For quantum simulations, the desired precision is independent of the system size N , and the required M is small compared to factoring. The second difference lies in the implementation cost of the repeated powers of the controlled- $U(\tau)$ gates for each application. In Shor’s algorithm, the gate is defined as $U(\tau)|x\rangle = |ax \bmod N\rangle$. Higher order powers of the unitary can be generated efficiently via modular exponentiation [60]. The result is that the implementation of $U(2^m\tau)$ requires $2m$ times the number of gates used for $U(\tau)$. For generic quantum simulation problems, the implementation cost of $U(2^m\tau)$ equals 2^m times the cost of $U(\tau)$, because of the Trotter parameter k . The implementation of the control unitary gates for quantum simulation is not as efficient as that for the modular exponentiation unitary gates. The third difference lies in the preparation of the initial N -qubit state $|\Psi\rangle$. The preparation of $|\Psi\rangle$ for the TIM problem by adiabatic evolution is comparable in resource

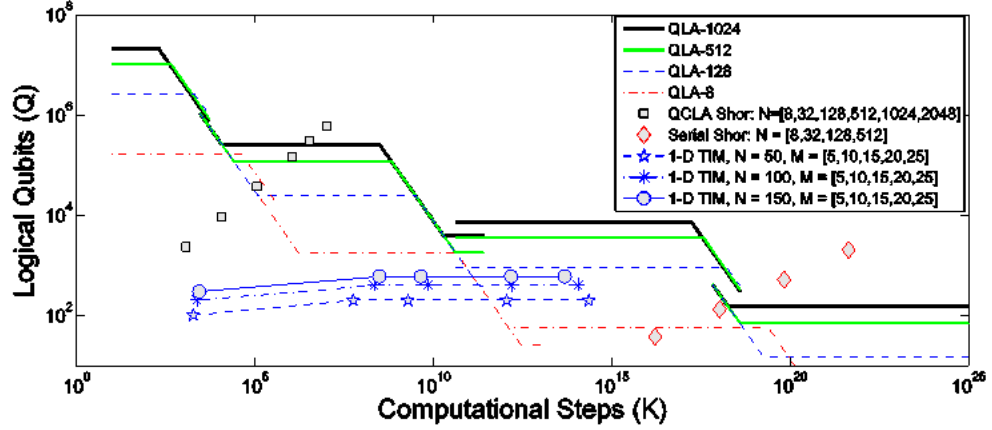


Figure 41: Performance characteristics of different QLA-based quantum computers in KQ space with fixed amount of physical resources. The binary precision for the Ising problem of $M = \{5, 10, 15, 20, 25\}$ corresponds to decimal precision of $\{1, 3, 4, 6, 7\}$ digits, respectively.

requirements to the phase estimation circuit. For Shor’s quantum factoring algorithm $|\Psi\rangle = |1\rangle$ in the computational basis and is easily prepared.

Finally, factoring integers large enough to be relevant for modern cryptanalysis requires several orders of magnitude more logical qubits than the scale of quantum simulation problems considered in this paper. At minimum, the factoring of an N -bit number requires $2N + 3$ qubits, using the same one-control qubit circuit given in Figure 34 [176]. As shown later in this section, choosing to use only the minimum number of qubits required for factoring leads to very high error correction overhead. A more reasonable implementation of the factoring algorithm requires $\mathcal{O}(N^2)$ number of logical qubits, which corresponds to millions of logical qubits for factoring a 1024-bit number. Quantum simulation problems require significantly less computational space and the problems considered in this paper require less than 500 logical qubits.

We examine how these differences affect the relative size of the QLA architecture required to implement each application. In particular, Figure 41 shows the performance of QLA-based quantum computers in KQ space with fixed physical resources.

Each horizontal line corresponds to the KQ limit for a QLA-based architecture modeled for factoring a 1024-bit number (top-most horizontal dashed line), a 512-bit number, a 128-bit number, and an 8-bit number, respectively. The physical resources for each QLA- N quantum computer (where $N = \{1024, 512, 128, 8\}$ bits) are determined by how many logical qubits at level 2 error correction are required to implement the Quantum Carry Look-ahead Adder (QCLA) factoring circuit [177, 144], which requires $\mathcal{O}(N^2)$ logical qubits and $\mathcal{O}(N \log^2 N)$ logical cycles. The plateaus in each QLA- N line of Figure 41 represent using all of the qubits at a specific level of encoding, with the top-most right-hand plateau representing level 1. Where the lines are sloped, the model is that only a certain number of the lower level encoded qubits can be used. Once this reaches the number of qubits that can be encoded at the next level, the quantum computer is switched from encoding level L to $L + 1$ by using all the available level L qubits.

A QLA- N quantum computer is capable of executing an application using level L encoded qubits if the application instance is mapped underneath the line representing the computer at level L in Figure 41. Factoring a 1024-bit number, for example, falls directly on the level 2 portion of the QLA-1024 line (see the square markers). Anything above that line cannot be implemented with the QLA-1024 computer. Similarly, factoring a 128-bit number maps under the QLA-128 line, but can be accomplished using level 1 qubits. The TIM problem is mapped onto Figure 41 for $N = 50, 100, 150$ and several binary precision instances: $M = \{5, 10, 15, 20, 25\}$. As expected, factoring requires many more logical qubits, however, both applications require similar levels of error correction. A decimal precision of up to 4 digits of accuracy ($M = 15$) can be reached by using a quantum computer capable of factoring an 8-bit number at level 2 error correction, however higher precision quickly requires level 3 error correction.

The resources for implementing quantum factoring with one-control-qubit were calculated following the circuit in Figure 34, where the unitary gates are replaced

with the unitary gates corresponding to modular exponentiation, as discussed in Ref. [176]. The results are shown with the diamond-shaped markers in Figure 41. While this particular implementation is the least expensive factoring network in terms of logical qubits, the high precision requirement of $M = O(N)$ makes this network very expensive in terms of time steps. In fact, the number of time steps required pushes the reliability requirements into level 4 error correction for factoring even modestly-sized numbers.

6.6 Conclusion

In this paper, the TIM quantum simulation circuit was decomposed into fault-tolerant operations and we estimated the circuit's resource requirements and number of logical cycles K as a function of the desired precision M in the estimate of the ground state energy. Our resource estimates were based on the QLA architecture and underlying technology parameters of trapped ions allowing us to estimate both K , as a function of the level of the error correction level, and the total length of the computation in real-time.

Our results indicate that even for small precision requirements K is large enough to require error correction. The growth of K is due to its linear dependence on the Trotter parameter k , which scales exponentially with the maximum desired precision M . In order for K to scale polynomially with the precision, new quantum simulation algorithms are required or systems must be chosen where the phase estimation algorithm can be implemented without the Trotter formula. The linear dependence of the number of time steps on k is due to the fact that U_x and the U_{zz} do not commute. However, there are some physical systems, whose Hamiltonians are composed of commuting terms, such as the nontransversal classical Ising model, which has a solution to the partition function in two dimensions but is NP-Complete for higher dimensions[178]. In those cases, Trotterization is unnecessary. In future work, we

intend to generalize the calculations of the resource requirements to other physical systems and consider different ways to implement the phase estimation algorithm that limit its dependence on the Trotter formula.

CHAPTER VII

CONCLUSION AND OUTLOOK

My thesis work has focused on demonstrating the necessary preliminary steps needed to perform a single molecule, non-destructive spectroscopy technique, which is the long term goal of our group. A proof of concept experiment was performed using atomic ions to demonstrate the Sympathetic Heating Spectroscopy (SHS) technique, which is described in Chapter 4. The technique is an incoherent analogue of quantum logic spectroscopy, and works by transferring information from a spectroscopy ion ($^{44}\text{Ca}^+$) to a control ion ($^{40}\text{Ca}^+$), where measurements can be performed using fluorescence spectroscopy. We demonstrated that the spectrum of $^{44}\text{Ca}^+$ could be measured when as few as 1500 photons were scattered into 4π , modulating the fluorescence signal of the control ion. It is not yet clear if this method would be sensitive enough to study molecular ions due to the rotational and vibrational degrees of freedom in molecules, which will limit the number of scattered photons.

Two other experimental issues that must be addressed before performing molecular ion spectroscopy are the detection/identification of dark molecular ions and sympathetic cooling of a molecular ion to the ground state. The first of these issues may be addressed by performing a new type of mass spectrometry, which relies on optical detection of the motional sideband of the trapped atomic ion. In this scheme, the molecular and atomic ions are coupled through the normal modes of their motion, and the mode structure is superimposed on the $S_{1/2}$ - $D_{5/2}$ optical qubit transition of calcium. The normal modes are a function of the mass, and the unknown ion is identified based on the sideband shift, as described in Chapter 5. Since the molecule is coupled to the atom through the normal modes, sideband cooling the atom

should sympathetically cool the molecule. Results demonstrating sideband cooling of an atomic ion were presented in Chapter 5 along with the necessary improvements needed to translationally ground state cool a molecular ion. With the ability to cool the molecular ion to the ground state, it is possible to perform quantum-SHS using the resolved sidebands to detect the spectrum. These preliminary results solve some of the experimental issues for the performance of SHS with a molecular ion. The greatest challenge when performing molecular ion spectroscopy is scattering sufficient photons to measure a spectrum. Our group, in collaboration with B. Odom’s group at Northwestern University and D. Sherill’s group at the Georgia Institute of Technology, has worked on theoretical calculations for identifying molecules to test SHS [59]. These molecules may also be good candidates for direct laser cooling of molecular ions, which has never been achieved [59].

7.1 *Future direction*

This work has focused on developing techniques to study molecular ions. Other groups have also started to use trapped atomic ions to sympathetically cool molecular ions. Most of the previous work has focused on using large Coulomb crystals of hundreds to thousands of atomic and molecular ions to perform applications in mass spectrometry, chemistry, and spectroscopy, which suggests that using these techniques are of scientific interest. For the molecular physicists and physical chemists using these techniques, the true potential is unknown because we are still in the development stages.

Reactive scattering experiments at lower temperatures (μ K) could lead to molecular ion quantum logic experiments. Our lab is currently pursuing sympathetically ground state cooling a molecular ion as a means to perform quantum logic experiments. Another area of interest is the ability to produce a translationally cold molecular ion while also having control of the internal (rovibrational) degrees of freedom.

This is necessary for performing state-selective low-temperature reactive-collision studies [87]. A few groups have demonstrated the ability to control the rotational and vibrational degrees of freedom using optical pumping techniques, essentially performing laser rotational cooling [55, 56]. Alternatively, rovibrational state selectivity can be achieved by using state-selective photoionization. Resonance-enhanced multi-photon-ionization techniques are highly selective of the final state of the ion, and pulsed field ionization can be even more selective [85, 86]. These techniques could be coupled to experiments using sympathetically cooled, trapped molecular ions to perform many experiments in a new temperature regime.

For frequency-metrology experiments with molecular ions it is important to use a non-destructive technique to perform multiple measurements on the same ion. It has been our focus to lay the ground work for this type of experimental protocol that has been demonstrated at NIST using atomic species [38, 39, 42]. It has proven to be very challenging to sympathetically ground state cool a molecular ion and to repeatedly prepare the molecular ion into the same internal quantum state. Although this type of experiment is difficult, it may be within reach for our lab in the near future. These types of frequency-metrology experiments with molecular ions will also allow quantum theoretical chemists to test new methods leading to more accurate computation of molecular systems. Additionally, these types of metrology experiments have been proposed to test variations in the ratio of the electron and proton masses [179, 180].

I have mentioned a few directions this field is moving in and it should be noted that there are many possible applications of using cold molecular ions to further understand physics and chemistry. Ultracold atoms have made a dramatic impact in science from the conformation of the Bose-Einstein Condensate to the use of ultracold atoms for quantum computation. Ultracold atoms have also had a large impact on society with the development of accurate atomic clocks, which are used in global

positioning systems. It is exciting to theorize what impact the new field of ultracold chemistry will have on both science and technology.

REFERENCES

- [1] G. R. Harrison, "The History of Spectroscopy, A Perspective", <http://web.mit.edu/spectroscopy/history/spec-history.html>, October 2011.
- [2] P. Atkins and J. de Paula, *Physical Chemistry*, Oxford University Press, 7 edition, 2003.
- [3] P. Atkins and R. Friedman, *Molecular Quantum Mechanics*, Oxford University Press, 4 edition, 2005.
- [4] A. Einstein, "On the quantum theory of radiation", *Z. Phys.*, vol. 18, pp. 121, 1917.
- [5] M. Bertolotti, *Masers and Lasers: A historical approach*, Adam Hilger Ltd, Techno House, 1983.
- [6] J. P. Gordon, H. J. Zeiger, and C. H. Townes, "The maser new type of microwave amplifier, frequency standard, and spectrometer", *Phys. Rev.*, vol. 99, pp. 1264, 1955.
- [7] T. H. Maiman, "Maser behavior: Temperature and concentration effects", *J. Appl. Phys.*, vol. 31, pp. 222, 1960.
- [8] A. Javan, W. R. Bennett Jr., and D. R. Herriott, "Population inversion and continuous optical maser oscillation in a gas discharge containing a he-ne mixture", *Phys. Rev. Lett.*, vol. 6, pp. 106, 1961.
- [9] W. E. Bell, "Visible laser transitions in Hg^+ ", *Appl. Phys. Lett.*, vol. 4, pp. 34, 1964.
- [10] C. K. N. Patel, "Continuous-wave laser action on vibrational-rotational transitions of CO_2 ", *Phys. Rev.*, vol. 136, pp. A1187, 1964.
- [11] C. K. N. Patel, "Interpretation of CO_2 optical maser experiments", *Phys. Rev. Lett.*, vol. 12, pp. 588, 1964.
- [12] C. K. N. Patel, "Selective excitation through vibrational energy transfer and optical maser action in $\text{N}_2\text{-CO}_2$ ", *Phys. Rev. Lett.*, vol. 13, pp. 617, 1964.
- [13] N. G. Basov, V. A. Danilychev, Y. M. Popov, and D. D. Khodkevich, "Laser operating in the vacuum region of the spectrum by excitation of liquid xenon with an electron beam", *JETP Lett.*, vol. 12, pp. 329, 1970.

- [14] H. A. Koehler, H. A. Ferderber, D. L. Redhead, and P. J. Ebert, “Stimulated vuv emission in high pressure xenon excited by high current relativistic electron beams”, *Appl. Phys. Lett.*, vol. 21, pp. 198, 1972.
- [15] F. P. Schafer, W. Schmidt, and K. Marth, “New dye lasers covering the visible spectrum”, *Phys. Lett. A*, vol. 24, pp. 280, 1967.
- [16] P. P. Sorokin, J. R. Lankard, E. C. Hammond, and V. L. Moruzzi, “Laser-pumped stimulated emission from organic dyes: experimental studies and analytical comparisons”, *IBM J. Res. Develop.*, vol. 11, pp. 130, 1967.
- [17] B. B. McFarland, “Laser second harmonic induced stimulated emission of organic dyes”, *Appl. Phys. Lett.*, vol. 10, pp. 208, 1967.
- [18] R. N. Hall, G. E. Fenner, J. O. Kingsley, T. J. Solty, and R. O. Carlson, “Coherent light emission from GaAs junctions”, *Phys. Rev. Lett.*, vol. 9, pp. 366, 1962.
- [19] M. I. Nathan, W. P. Dumke, G. Burns, F.H. Drill Jr., and G. Lasher, “Semiconductor maser of GaAs”, *Appl. Phys. Lett.*, vol. 1, pp. 91, 1962.
- [20] D. Wineland and H. Dehmelt, “Proposed 10^{14} delta upsilon less than upsilon laser fluorescence spectroscopy on Tl⁺ mono-ion oscillator III”, *Bulletin of the American Physical Society*, vol. 20, pp. 637, 1975.
- [21] T. W. Hansch and A. L. Schawlow, “Cooling of gases by laser radiation”, *Optics Communications*, vol. 13, pp. 68, 1975.
- [22] W. D. Phillips, “Laser cooling and trapping of neutral atoms”, *Rev. Mod. Phys.*, vol. 70, no. 3, pp. 721, 1998.
- [23] M. D. Barrett, B. DeMarco, T. Schaetz, V. Meyer, D. Leibfried, J. Britton, J. Chiaverini, W. M. Itano, B. Jelenkovic, J. D. Jost, C. Langer, T. Rosenband, and D. J. Wineland, “Sympathetic cooling of Be-9(+) and Mg-24(+) for quantum logic”, *Phys. Rev. A*, vol. 68, no. 4, pp. 042302, 2003.
- [24] P. O. Schmidt, T. Rosenband, C. Langer, W. M. Itano, J. C. Bergquist, and D. J. Wineland, “Spectroscopy using quantum logic”, *Science*, vol. 309, no. 5735, pp. 749, 2005.
- [25] J. Benhelm, G. Kirchmair, C. F. Roos, , and R. Blatt, “Towards fault-tolerant quantum computing with trapped ions”, *Nature Physics*, vol. 4, pp. 463, 2008.
- [26] T. Monz, K. Kim, W. Hansel, M. Riebe, A. S. Villar, P. Schindler, M. Hennrich M. Chwalla, and R. Blatt, “Realization of the quantum toffoli gate with trapped ions”, *Phys. Rev. Lett.*, vol. 102, pp. 040501, 2009.
- [27] D. Hanneke, J. P. Home, J. D. Jost, J. M. Amini, D. Leibfried, and D. J. Wineland, “Realization of a programmable two-qubit quantum processor”, *Nature Physics*, vol. 6, pp. 13, 2010.

- [28] M. D. Barrett, J. Chiaverini, T. Schaetz, J. Britton, W. M. Itano, J. D. Jost, E. Knill, C. Langer, D. Leibfried, R. Ozeri, and D. J. Wineland, “Deterministic quantum teleportation of atomic qubits”, *Nature*, vol. 429, pp. 737, 2004.
- [29] M. Riebe, H. Haoner, C. F. Roos, W. Hansel, J. Benhelm, G. P. T. Lancaster, T. W. Korber, C. Becher, F. Schmidt-Kaler, D. F. V. James, and R. Blatt, “Deterministic quantum teleportation with atoms”, *Nature*, vol. 429, pp. 734, 2004.
- [30] R. Zhao, Y. O. Dudin, S. D. Jenkins, C. J. Campbell, D. N. Matsukevich, T. A. B. Kennedy, and A. Kuzmich, “Long-lived quantum memory”, *Nature Physics*, vol. 5, pp. 100, 2009.
- [31] V. Gerginov, K. Calkins, C. E. Tanner, J. J. McFerran, S. Diddams, A. Bartels, and L. Hollberg, “Optical frequency measurements of $6s\ S-2(1/2)-6p\ P-2(1/2)$ (D-1) transitions in Cs-133 and their impact on the fine-structure constant”, *Phys. Rev. A*, vol. 73, 2006.
- [32] P. Clade, E. de Mirandes, M. Cadoret, S. Guellati-Khelifa, C. Schwob, F. Nez, L. Julien, and F. Biraben, “Determination of the fine structure constant based on Bloch oscillations of ultracold atoms in a vertical optical lattice”, *Phys. Rev. Lett.*, vol. 96, pp. 033001, 2006.
- [33] S. Blatt, A. D. Ludlow, G. K. Campbell, J. W. Thomsen, T. Zelevinsky, M. M. Boyd, J. Ye, X. Baillard, M. Fouché, R. Le Targat, A. Brusch, P. Lemonde, M. Takamoto, F.-L. Hong, H. Katori, and V. V. Flambaum, “New limits on coupling of fundamental constants to gravity using 87Sr optical lattice clocks”, *Phys. Rev. Lett.*, vol. 100, pp. 140801, 2008.
- [34] V. Batteiger, S. Knünz, M. Herrmann, G. Saathoff, H. A. Schuessler, B. Bernhardt, T. Wilken, R. Holzwarth, T. W. Hänsch, and Th. Udem, “Precision spectroscopy of the $3s-3p$ fine-structure doublet in Mg^+ ”, *Phys. Rev. A*, vol. 80, no. 2, pp. 022503, 2009.
- [35] A. L. Wolf, S. A. van den Berg, W. Ubachs, and K. S. E. Eikema, “Direct frequency comb spectroscopy of trapped ions”, *Phys. Rev. Lett.*, vol. 102, no. 22, pp. 223901, 2009.
- [36] A. L. Wolf, S. A. van den Berg, C. Gohle, E. J. Salumbides, W. Ubachs, and K. S. E. Eikema, “Frequency metrology on the $4s\ S\ 1/2\ 2-4p\ P\ 1/2\ 2$ transition in Ca^{+40} for a comparison with quasar data”, *Phys. Rev. A*, vol. 78, no. 3, pp. 032511, 2008.
- [37] M. Herrmann, V. Batteiger, S. Knünz, G. Saathoff, Th. Udem, and T. W. Hänsch, “Frequency metrology on single trapped ions in the weak binding limit: the $3s(1/2)-3p(3/2)$ transition in $\text{Mg-24}(+)$ ”, *Phys. Rev. Lett.*, vol. 102, no. 1, pp. 013006, 2009.

- [38] T. Rosenband, P. O. Schmidt, D. B. Hume, W. M. Itano, T. M. Fortier, J. E. Stalnaker, K. Kim, S. A. Diddams, J. C. J. Koelemeij, J. C. Bergquist, and D. J. Wineland, “Observation of the S-1(0)-(3)P0 clock transition in Al-27(+)”, *Phys. Rev. Lett.*, vol. 98, no. 22, pp. 220801, 2007.
- [39] T. Rosenband, D. B. Hume, P. O. Schmidt, C. W. Chou, A. Brusch, L. Lorini, W. H. Oskay, R. E. Drullinger, T. M. Fortier, J. E. Stalnaker, S. A. Diddams, W. C. Swann, N. R. Newbury, W. M. Itano, D. J. Wineland, and J. C. Bergquist, “Frequency ratio of Al+ and Hg+ single-ion optical clocks; metrology at the 17th decimal place”, *Science*, vol. 319, no. 5871, pp. 1808, 2008.
- [40] K. Matsubara, K. Hayasaka, Y. Li, H. Ito, S. Nagano, M. Kajit, and M. Hosokawa, “Frequency measurement of the optical clock transition of $^{40}\text{Ca}^+$ ions with an uncertainty of 10^{-14} level”, *Applied Physics Express*, vol. 1, pp. 067011, 2008.
- [41] C. J. Campbell, A. V. Steele, L. R. Churchill, M. V. DePalatis, D. E. Naylor, D. N. Matsukevich, A. Kuzmich, and M. S. Chapman, “Multiply charged thorium crystals for nuclear laser spectroscopy”, *Phys. Rev. Lett.*, vol. 102, pp. 233004, 2009.
- [42] C. W. Chou, D. B. Hume, T. Rosenband, and D. J. Wineland, “Optical clocks and relativity”, *Science*, vol. 329, pp. 1630, 2010.
- [43] S. Willitsch, M. T. Bell, A. D. Gingell, S. R. Procter, and T. P. Softley, “Cold reactive collisions between laser-cooled ions and velocity-selected neutral molecules”, *Phys. Rev. Lett.*, vol. 100, no. 4, pp. 043203, 2008.
- [44] M. Drewsen, I. Jensen, J. Lindballe, N. Nissen, R. Martinussen, A. Mortensen, P. Staunum, and D. Voigt, “Ion coulomb crystals: a tool for studying ion processes”, *Int. J. Mass Spectrom.*, vol. 229, no. 1-2, pp. 83, 2003.
- [45] M. T. Bell and T. P. Softley, “Ultracold molecules and ultracold chemistry”, *Mol. Phys.*, vol. 107, no. 2, pp. 99, 2009.
- [46] L. D. Carr, D. DeMille, R. V. Krems, and J. Ye, “Cold and ultracold molecules—science, technology and applications”, *New J. Phys.*, vol. 11, pp. 055049, 2009.
- [47] M. T. Bell, A. D. Gingell, J. M. Oldham, T. P. Softley, and S. Willitsch, “Ion-molecule chemistry at very low temperatures—cold chemical reactions between coulomb-crystallized ions and velocity-selected neutral molecules”, *Phys. Scr.*, vol. 142, pp. 73, 2009.
- [48] K. Okada, M. Wada, L. Boesten, T. Nakamura, I. Katayama, and S. Ohtani, “Acceleration of the chemical reaction of trapped Ca^+ ions with H_2O molecules by laser excitation”, *J. Phys. B: At. Mol. Opt. Phys.*, vol. 36, no. 1, pp. 33, 2003.

- [49] B. Roth, P. Blythe, H. Wenz, H. Daerr, and S. Schiller, “Ion-neutral chemical reactions between ultracold localized ions and neutral molecules with single-particle resolution”, *Phys. Rev. A*, vol. 73, no. 4, pp. 042712, 2006.
- [50] B. Roth, P. Blythe, H. Daerr, L. Patacchini, and S. Schiller, “Production of ultracold diatomic and triatomic molecular ions of spectroscopic and astrophysical interest”, *J. Phys. B: At. Mol. Opt. Phys.*, vol. 39, no. 19, pp. S1241, 2006.
- [51] P. F. Sta anum, K. Hojbjerre, R. Wester, and M. Drewsen, “Probing isotope effects in chemical reactions using single ions”, *Phys. Rev. Lett.*, vol. 100, no. 24, pp. 243003, 2008.
- [52] K. Hojbjerre, D. Offenber g, C. Z. Bisgaard, H. Stapelfeldt, P. F. Sta anum, A. Mortensen, and M. Drewsen, “Consecutive photodissociation of a single complex molecular ion”, *Phys. Rev. A*, vol. 77, no. 3, pp. 030702, 2008.
- [53] D. Offenber g, C. Wellers, C. B. Zhang, B. Roth, and S. Schiller, “Measurement of small photodestruction rates of cold, charged biomolecules in an ion trap”, *J. Phys. B: At. Mol. Opt. Phys.*, vol. 42, no. 3, pp. 035101, 2009.
- [54] M. Kajita, “Sensitive measurement of $m(p)/m(e)$ variance using vibrational transition frequencies of cold molecules”, *New J. of Phys.*, vol. 11, pp. 055010, 2009.
- [55] P. F. Sta anum, K. Hojbjerre, P. S. Skyt, A. K. Hansen, and M. Drewsen, “Rotational laser cooling of vibrationally and translationally cold molecular ions”, *Nat. Phys.*, vol. 6, no. 4, pp. 271, 2010.
- [56] T. Schneider, B. Roth, H. Duncker, I. Ernsting, and S. Schiller, “All-optical preparation of molecular ions in the rovibrational ground state”, *Nat. Phys.*, vol. 6, no. 4, pp. 275, 2010.
- [57] E. S. Shuman, J. F. Barry, D. R. Glenn, and D. DeMille, “Radiative force from optical cycling on a diatomic molecule”, *Phys. Rev. Lett.*, vol. 103, no. 22, pp. 223001, 2009.
- [58] E. S. Shuman, J. F. Barry, and D. DeMille, “Laser cooling of a diatomic molecule”, *Nature*, vol. 467, pp. 820, 2010.
- [59] J. H. V. Nguyen, C. R. Viteri, E. G. Hohenstein, C. D. Sherrill, K. R. Brown, and B. Odom, “Challenges of laser-cooling molecular ions”, *New J. of Phys.*, vol. 13, pp. 063023, 2011.
- [60] P. W. Shor, “Polynomial-time algorithms for prime factorization and discrete logarithms on a quantum computer”, in *Proceedings of the 35th annual Symposium on Foundations of Computer Science*, Los Alamitos, CA, 1994, p. 124, IEEE.

- [61] J. I. Cirac and P. Zoller, “Quantum computations with cold trapped ions”, *Phys. Rev. Lett.*, vol. 74, pp. 4091, 1995.
- [62] C. Monroe, D. M. Meekhof, B. E. King, S. R. Jefferts, W. M. Itano, D. J. Wineland, and P. Gould, “Resolved-side-band raman cooling of bound atom to the 3D zero-point energy”, *Phys. Rev. Lett.*, vol. 75, no. 22, pp. 4011, 1995.
- [63] F. Schmidt-Kaler, H. Haffner, M. Riebe, S. Gulde, G. P. T. Lancaster, T. Deuschle, C. Becher, C. F. Roos, J. Eschner, and R. Blatt, “Realization of the cirac-zoller controlled-not quantum gate”, *Nature*, vol. 422, pp. 408, 2003.
- [64] R. Feynman, “Simulating physics with computers”, *International Journal of Theoretical Physics*, vol. 21, pp. 467, 1982.
- [65] I. Buluta and F. Nori, “Quantum simulators”, *Science*, vol. 326, no. 5949, pp. 108, 2009.
- [66] R. Islam, E. E. Edwards, K. Kim, S. Korenblit, C. Noh, H. Carmichael, G. D. Lin, L. M. Duan, C. C. Joseph Wang, J. K. Freericks, and C. Monroe, “Onset of a quantum phase transition with a trapped ion quantum simulator”, *Nature Communications*, vol. 2, pp. 377, 2011.
- [67] G. D. Lin, C. Monroe, , and L. M. Duan, “Sharp phase transitions in a small frustrated network of trapped ion spins”, *Phys. Rev. Lett.*, vol. 106, pp. 230402, 2011.
- [68] R. Gerritsma, G. Kirchmair, F. Zhringer, E. Solano, R. Blatt, and C. F. Roos, “Quantum simulation of the dirac equation”, *Nature*, vol. 463, pp. 68, 2010.
- [69] R. Gerritsma, B.P. Lanyon, G. Kirchmair, Zhringer, C. Hempel, J. Casanova, J.J. Garcia-Ripoll, E. Solano, R. Blatt, and C.F. Roos, “Quantum simulation of the klein paradox”, *Phys. Rev. Lett.*, vol. 106, pp. 060503, 2011.
- [70] L. Lamata, J. Casanova, R. Gerritsma, C. F. Roos, J. J. Garcia-Ripoll, and E. Solano, “Relativistic quantum mechanics with trapped ions”, *New J. Phys.*, vol. 13, pp. 095003, 2011.
- [71] H. S. Margolis, “Frequency metrology and clocks”, *Journal of Physics B-Atomic Molecular and optical Physics*, vol. 42, no. 15, 2009.
- [72] J. Koperski and E. S. Fry, “Molecules in the cold environment of supersonic free-jet beam: from spectroscopy of neutral-neutral interactions to a test of bell’s inequality”, *J. Phys. B: At. Mol. Opt. Phys.*, vol. 39, pp. S1125, 2006.
- [73] T. A. Miller, “Chemistry and chemical intermediates in supersonic free jet expansions”, *Science*, vol. 223, no. 4636, pp. 545, 1984.

- [74] Y. T. Lee, “Molecular beam studies of elementary chemical process”, *Science*, vol. 236, no. 4803, pp. 793, 1987.
- [75] D. Herschbach, “Molecular collisions, from warm to ultracold”, *Faraday Discuss.*, vol. 142, pp. 9, 2009.
- [76] R. V. Krems, W. C. Stwalley, and B. Friedrich, Eds., *Cold Molecules: Theory, Experiment, Applications*, CRC press, 2009.
- [77] F. Bretislav and J. M. Doylei, “Why are cold molecules so hot?”, *Chemphyschem*, vol. 10, no. 4, pp. 604, 2009.
- [78] T. Baba and I. Waki, “Cooling and mass-analysis of molecules using laser-cooled atoms”, *Jpn. J. Appl. Phys.*, vol. 35, no. 9A, pp. L1134–L1137, 1996.
- [79] K. Molhave and M. Drewsen, “Formation of translationally cold MgH^+ and MgD^+ molecules in an ion trap”, *Phys. Rev. A*, vol. 62, no. 1, pp. 011401, 2000.
- [80] A. Ostendorf, C. B. Zhang, M. A. Wilson, D. Offenberger, B. Roth, and S. Schiller, “Sympathetic cooling of complex molecular ions to millikelvin temperatures”, *Phys. Rev. Lett.*, vol. 97, no. 24, pp. 243005, 2006.
- [81] B. Roth, U. Frohlich, and S. Schiller, “Sympathetic cooling of $\text{He-4}(+)$ ions in a radio-frequency trap”, *Phys. Rev. Lett.*, vol. 94, no. 5, pp. 053001, 2005.
- [82] C. Wellers, A. Borodin, S. Vasilyev, D. Oenberg, and S. Schiller, “Resonant multi-photon IR dissociation spectroscopy of a trapped and sympathetically cooled biomolecular ion species”, 2011.
- [83] J. C. J. Koelemeij, B. Roth, and S. Schiller, “Blackbody thermometry with cold molecular ions and application to ion-based frequency standards”, *Phys. Rev. A*, vol. 76, no. 2, pp. 023413, 2007.
- [84] B. Roth, J. C. J. Koelemeij, H. Daerr, and S. Schiller, “Rovibrational spectroscopy of trapped molecular hydrogen ions at millikelvin temperatures”, *Phys. Rev. A*, vol. 74, no. 4, pp. 040501, 2006.
- [85] X. Tong, A. H. Winney, and S. Willitsch, “Sympathetic cooling of molecular ions in selected rotational and vibrational states produced by threshold photoionization”, *Phys. Rev. Lett.*, vol. 105, no. 14, 2010.
- [86] X. Tong, D. Wild, and S. Willitsch, “Collisional and radiative effects in the state-selective preparation of translationally cold molecular ions in ion traps”, *Phys. Rev. A*, vol. 83, no. 2, 2011.
- [87] S. Willitsch, M. T. Bell, A. D. Gingell, and T. P. Softley, “Chemical applications of laser- and sympathetically-cooled ions in ion traps”, *Phys. Chem. Chem. Phys.*, vol. 10, no. 48, pp. 7200, 2008.

- [88] L. R. Churchill, *Trapping Triply Ionized Thorium Isotopes*, PhD thesis, Georgia Institute of Technology, 2010.
- [89] P. K. Ghosh, *Ion Traps*, Oxford Press, 2007.
- [90] H. Haffner, C. F. Roos, and R. Blatt, “Quantum computing with trapped ions”, *Physics Reports-Review Section of Physics Letters*, vol. 469, no. 4, pp. 155, 2008.
- [91] H. J. Metcalf and P. van der Staten, *Laser Cooling and Trapping*, Springer-Verlag, 1999.
- [92] D. J. Berkeland, J. D. Miller, J. C. Bergquist, W. M. Itano, and D. J. Wineland, “Minimization of ion micromotion in paul trap”, *J. Appl. Phys.*, vol. 83, no. 10, pp. 5025, 1998.
- [93] P. J. Richerme, “Depletion, quantum jumps, and temperature measurements of 88Sr^+ ions in a linear paul trap”, 2006.
- [94] F. W. J. Olver, D. W. Lozier, and R. F. Boisvert, *NIST Handbook of Mathematical Functions*, Cambridge University Press, 2010.
- [95] A. V Steele, *Barium ion cavity QED and Triply Ionized Thorium ion trapping*, PhD thesis, Georgia Institute of Technology, 2008.
- [96] H. R. Gray, R. M. Whitley, and Jr. C. R. Stroud, “Coherent trapping of atomic populations”, *Opt. Lett.*, vol. 3, no. 6, pp. 218, 1978.
- [97] Y. Ralchenko, A. E. Kramida, J. Reader, and NIST ASD Team, “Nist atomic spectra database”, <http://physics.nist.gov/asd>, July 2011, National Institute of Standards and Technology.
- [98] H. Oberst, “Resonance fluorescence of single barium ions”, 1999.
- [99] C. F. Roos, *Controlling the quantum state of trapped ions*, PhD thesis, University of Innsbruck, 2000.
- [100] D. J. Wineland, C. Monroe, W. M. Itano, D. Leibfried, B. E. King, and D. M. Meekhof, “Experimental issues in coherent quantum-state manipulation of trapped atomic ions”.
- [101] F. Diedrich, J. C. Bergquist, Wayne M. Itano, and D. J. Wineland, “Laser cooling to the zero-point energy of motion”, *Phys. Rev. Lett.*, vol. 62, no. 4, pp. 403, 1989.
- [102] D. J. Wineland and W. M. Itano, “Laser cooling of atoms”, *Phys. Rev. A*, vol. 20, no. 4, pp. 1521, 1979.

- [103] R. J. Epstein, S. Seidelin, D. Leibfried, J. H. Wesenberg, J. J. Bollinger, J. M. Amini, R. B. Blakestad, J. Britton, J. P. Home, W. M. Itano, J. D. Jost, E. Knill, C. Langer, R. Ozeri, N. Shiga, and D. J. Wineland, “Simplified motional heating rate measurements of trapped ions”, *Phys. Rev. A*, vol. 76, no. 3, pp. 033411, 2007.
- [104] J. H. Wesenberg, R. J. Epstein, S. Leibfried, R. B. Blakestad, J. Britton, J. P. Home, W. M. Itano, J. D. Jost, E. Knill, C. Langer, R. Ozeri, S. Seidelin, and D. J. Wineland, “Fluorescence during doppler cooling of single trapped atom”, *Phys. Rev. A*, vol. 76, pp. 053416, 2007.
- [105] D. J. Larson, J. C. Bergquist, J. J. Bollinger, W. M. Itano, and D. J. Wineland, “Sympathetic cooling of trapped ions: A laser-cooled two-species nonneutral ion plasma”, *Phys. Rev. Lett.*, vol. 57, pp. 70, 1986.
- [106] J. M. Amini, J. Britton, D. Leibfried, and D. J. Wineland, “Microfabricated chip traps for ions”, *arXiv:0812.3907v1*, 2008.
- [107] Q. A. Turchette, D. Kielpinski, B. E. King, D. Leibfried, D. M. Meekhof, C. J. Myatt, M. A. Rowe, C. A. Sackett, C.S. Wood, W. M. Itano, C. Monroe, and D. J. Wineland, “Heating of trapped ions from the quantum ground state”, *Phys. Rev. A*, vol. 61, pp. 063418, 2000.
- [108] D. M. Lucas, A. Ramos, J. P. Home, M. J. McDonnell, S. Nakayama, J. P. Stacey, S. C. Webster, D. N. Stacey, and A. M. Steane, “Isotope-selective photoionization for calcium ion trapping”, *Phys. Rev. A*, vol. 69, no. 1, pp. 012711, 2004.
- [109] U. Tanaka, H. Matsunishi, I. Morita, and S. Urabe, “Isotope-selective trapping of rare calcium ions using high-power incoherent light sources for the second step of photo-ionization”, *Appl. Phys. B*, vol. 81, no. 6, pp. 795, 2005.
- [110] E. J. Salumbides, V. Maslinskas, I. M. Dildar, A. L. Wolf, E. J. van Duijn, K. S. E. Eikema, and W. Ubachs, “High-precision frequency measurement of the 423-nm Ca I line”, *Phys. Rev. A*, vol. 83, no. 1, pp. 012502, 2011.
- [111] T. Furukawa, J. Nishimura, U. Tanaka, and S. Urabe, “Design and characteristic measurement of miniature three-segment linear paul trap”, *Jpn. J. Appl. Phys.*, vol. 44, no. 10, pp. 7619, 2005.
- [112] D. R. Leibbrandt, J. Labaziewicz, V. Vuletic, and I. L. Chuang, “Cavity sideband cooling of a single trapped ion”, *Phys. Rev. Lett.*, vol. 103, pp. 103001, 2009.
- [113] K. R. Brown, C. R. Clark, J. E. Goeters, N. Khanyile, C. R. Viteri, and G. D. Vittorini, “Laser-cooled atomic ions as probes of molecular ions”, *SMILES*, 2010.

- [114] M. Drewsen, A. Mortensen, R. Martinussen, P. Sta anum, and J. L. Sorensen, “Nondestructive identification of cold and extremely localized single molecular ions”, *Phys. Rev. Lett.*, vol. 93, no. 24, pp. 243201, 2004.
- [115] P. Blythe, B. Roth, U. Frohlich, H. Wenz, and S. Schiller, “Production of ultracold trapped molecular hydrogen ions”, *Phys. Rev. Lett.*, vol. 95, no. 18, pp. 183002, 2005.
- [116] V. L. Ryjkov, X. Zhao, and H. A. Schuessler, “Sympathetic cooling of fullerene ions by laser-cooled Mg^+ ions in a linear rf trap”, *Phys. Rev. A*, vol. 74, no. 2, pp. 023401, 2006.
- [117] D. Offenber g, C. B. Zhang, C. Wellers, B. Roth, and S. Schiller, “Translational cooling and storage of protonated proteins in an ion trap at subkelvin temperatures”, *Phys. Rev. A*, vol. 78, no. 6, pp. 061401, 2008.
- [118] V. A. Alekseev, D. D. Krylova, and V. S. Letokhov, “Sympathetic cooling of 2 trapped ions”, *Phys. Scr.*, vol. 51, no. 3, pp. 368, 1995.
- [119] T. Papenbrock, A. N. Salgueiro, and H. A. Weidenmuller, “Rate equations for sympathetic cooling of trapped bosons or fermions”, *Phys. Rev. A*, vol. 65, no. 4, Part B, pp. 043601, 2002.
- [120] T. Baba and I. Waki, “Sympathetic cooling rate of gas-phase ions in a radio-frequency-quadrupole ion trap”, *Appl. Phys. B*, vol. 74, no. 4-5, pp. 375, 2002.
- [121] W. Schnitzler, N. M. Linke, R. Fickler, J. Meijer, F. Schmidt-Kaler, and K. Singer, “Deterministic ultracold ion source targeting the heisenberg limit”, *Phys. Rev. Lett.*, vol. 102, no. 7, pp. 070501, 2009.
- [122] J. C. J. Koelemeij, B. Roth, A. Wicht, I. Ernsting, and S. Schiller, “Vibrational spectroscopy of HD^+ with 2-ppb accuracy”, *Phys. Rev. Lett.*, vol. 98, no. 17, pp. 173002, 2007.
- [123] K. Hojbjerg, A. K. Hansen, P. S. Skyt, P. F. Sta anum, and M. Drewsen, “Rotational state resolved photodissociation spectroscopy of translationally and vibrationally cold MgH^+ ions: toward rotational cooling of molecular ions”, *New J. Phys.*, vol. 11, pp. 055026, 2009.
- [124] N. Kjaergaard, L. Hornekaer, A. M. Thommesen, Z. Videsen, and M. Drewsen, “Isotope selective loading of an ion trap using resonance-enhanced two-photon ionization”, *Appl. Phys. B*, vol. 71, no. 2, pp. 207, 2000.
- [125] S. Gulde, D. Rotter, P. Barton, F. Schmidt-Kaler, R. Blatt, and W. Hogervorst, “Simple and efficient photo-ionization loading of ions for precision ion-trapping experiments”, *Appl. Phys. B*, vol. 73, no. 8, pp. 861, 2001.
- [126] E. Arimondo, “Coherent population trapping in laser spectroscopy”, in *Progress in Optics*, vol. 35, pp. 257–354. Elsevier Science Publ B V, 1996.

- [127] J. K. Webb, V. V. Flambaum, C. W. Churchill, M. J. Drinkwater, and J. D. Barrow, “Search for time variation of the fine structure constant”, *Phys. Rev. Lett.*, vol. 82, no. 5, pp. 884, 1999.
- [128] C. R. Clark, J. E. Goeders, Y. K. Dodia, C. R. Viteri, and K. R. Brown, “Detection of single-ion spectra by Coulomb-crystal heating”, *Phys. Rev. A*, vol. 81, no. 4, pp. 043428, 2010.
- [129] K. Sheridan and M. Keller, “Weighing of trapped ion crystals and its applications”, *arXiv:1106.2771v2*.
- [130] P. O. Schmidt, T. Rosenband, J. Koelemeij, D. Hume, W. M. Itano, J. C. Bergquist, and D. J. Wineland, “Spectroscopy of atomic and molecular ions using quantum logic”, *Proc. Non-Neutral Plasma VI*, p. 305, 2006.
- [131] S. Urabe, H. Imajo, K. Hayasaka, and M. Watanabe, “Trapping of Ca^+ ions and optical detection”, *Jpn. J. Appl. Phys.*, vol. 30, pp. 1532, 1991.
- [132] H. C. Nägerl, Ch. Roos, D. Leibfried, H. Rohde, G. Thalhammer, J. Eschner, F. Schmidt-Kaler, and R. Blatt, “Investigating a qubit candidate: Spectroscopy on the $S_{1/2}$ to $D_{5/2}$ transition of a trapped calcium ion in a linear paul trap”, *Phys. Rev. A*, vol. 61, pp. 023405, Jan 2000.
- [133] D. R. Lide, *CRC Handbook of Chemistry and Physics, 88th Edition (CRC Handbook of Chemistry & Physics)*, CRC Press, 88 edition, 2007.
- [134] S. Lloyd, “Universal quantum simulators”, *Science*, vol. 273, pp. 1073, 1996.
- [135] D. Abrams and S. Lloyd, “Simulation of many-body fermi systems on a universal quantum computer”, *Phys. Rev. Lett.*, vol. 79, pp. 2586, 1997.
- [136] D. Abrams and S. Lloyd, “Quantum algorithm providing exponential speed increase for finding eigenvalues and eigenvectors”, *Phys. Rev. Lett.*, vol. 83, pp. 5162, 1999.
- [137] C. Zalka, “Simulating quantum systems on a quantum computer”, *Proc. R. Soc. Lond. A*, vol. 454, pp. 313, 1998.
- [138] A. Aspuru-Guzik, A. Dutoi, P. Love, and M. Head-Gordon, “Simulated quantum computation of molecular energies”, *Science*, vol. 309, pp. 1704, 2005.
- [139] I. Kassal, S. P. Jordan, P. J. Love, M. Mohseni, and A. Aspuru-Guzik, “Quantum algorithms for the simulation of chemical dynamics”, *Proceedings of the National Academy of Science*, vol. 105, pp. 1868, 2008.
- [140] P. Pfeuty, “The one-dimensional Ising model with a transverse field”, *Annals of Physics*, vol. 57, pp. 79, 1970.
- [141] S. Sachdev, *Quantum Phase Transitions*, Cambridge University Press, Cambridge, England, U.K., 1999.

- [142] A. Juozapavičius, S. Caprara, and A. Rosengren, “Quantum Ising model in a transverse random field: A density-matrix renormalization-group analysis”, *Phys. Rev. B*, vol. 56, no. 17, pp. 11097.
- [143] A. Y. Kitaev, A. H. Shen, and M. N. Vyalyi, *Classical and Quantum Computation*, vol. 47 of *Graduate Studies in Mathematics*, American Mathematical Society, Providence, 2002.
- [144] T. S. Metodi, D. D. Thaker, A. W. Cross, F. T. Chong, and I. L. Chuang, “A quantum logic array microarchitecture: Scalable quantum data movement and computation”, in *Proceedings of the 38th annual IEEE/ACM International Symposium on Microarchitecture*, Washington, DC, 2005, p. 305, IEEE Computer Society.
- [145] R. J. Elliott, P. Pfeuty, and C. Wood, “Ising model with a transverse field”, *Phys. Rev. Lett.*, vol. 25, pp. 7, 1970.
- [146] R. Jullien, P. Pfeuty, J. N. Fields, and S. Doniach, “Zero-temperature renormalization method for quantum systems. I. Ising model in a transverse field in one dimension”, *Phys. Rev. B*, vol. 18, no. 7, pp. 3568, 1978.
- [147] R. Moessner and S. L. Sondhi, “Ising and dimer models in two and three dimensions”, *Phys. Rev. B*, vol. 68, pp. 054405, 2003.
- [148] Y. Hu and A. Du, “Magnetization behavior and magnetic entropy change of frustrated Ising antiferromagnets on two and three dimensional lattices”, *J. Phys.:Condens. Matter*, vol. 20, pp. 125225, 2008.
- [149] M. Santos, “Short-time critical dynamics for the transverse Ising model”, *Phys. Rev. E*, vol. 61, no. 6, pp. 7204.
- [150] S. Parker and M. B. Plenio, “Efficient factorization with a single pure qubit and logn mixed qubits”, *Phys. Rev. Lett.*, vol. 85, pp. 3049, 2000.
- [151] R. Cleve, A. Ekert, C. Macchiavello, and M. Mosca, “Quantum algorithms revisited”, *Proc. R. Soc. Lon. A*, vol. 454, pp. 339, 1998.
- [152] K. R. Brown, R. J. Clark, and I. L. Chuang, “Limitations of quantum simulation examined by simulating a pairing hamiltonian using nuclear magnetic resonance”, *Phys. Rev. Lett.*, vol. 97, pp. 050504, 2006.
- [153] J. Kempe, A. Kitaev, and O. Regev, “The complexity of the local hamiltonian problem”, *SIAM Journal of Computing*, vol. 35, pp. 1070, 2006.
- [154] J. D. Biamonte and P. J. Love, “Realizable hamiltonians for universal adiabatic quantum computers”, *Phys. Rev. A*, vol. 78, no. 7, pp. 012352.
- [155] M. Suzuki, “General theory of high order decomposition of exponential operators and symplectic intergration”, *Phys. Lett. A*, vol. 165, pp. 387, 1992.

- [156] M. A. Nielsen and I. L. Chuang, *Quantum Computation and Quantum Information*, Cambridge University Press, Cambridge, UK, 2001.
- [157] C. M. Dawson and M. A. Nielsen, “The Solovay-Kitaev algorithm”, *Quant. Inf. Comp.*, vol. 6, pp. 81, 2005.
- [158] P. Shor, “Fault-tolerant quantum computation”, in *Proceedings of the 37th annual Symposium on the Foundations of Computer Science*, Los Alamitos, CA, 1996, pp. 56–65, IEEE.
- [159] D. Aharonov and M. Ben-Or, “Fault tolerant computation with constant error”, in *Proceedings of the 29th annual ACM Symposium on Theory of Computing*, New York, NY, USA, 1997, vol. 29, p. 176, ACM.
- [160] A. Y. Kitaev, “Quantum error correction with imperfect gates”, in *Proceedings of the 3rd International Conference of Quantum Communication and Measurement*, O. Hirota, A. S. Holevo, and C. M. Caves, Eds., New York, NY, 1997, p. 181, Plenum.
- [161] A. M. Steane, “Space, time, parallelism and noise requirements for reliable quantum computing”, *Fortschritte der Physik*, vol. 46, no. 4, pp. 443, 1999.
- [162] D. J. Wineland, M. Barrett, J. Britton, J. Chiaverini, B. L. DeMarco, W. M. Itano, B. M. Jelenkovic, C. Langer, D. Leibfried, V. Meyer, T. Rosenband, and T. Schaetz, “Quantum information processing with trapped ions”, *Phil. Trans. R. Soc. Lond.*, vol. A361, pp. 1349, 2003.
- [163] J. Chiaverini, R. B. Blakestad, J. Britton, J. D. Jost, C. Langer, D. Leibfried, R. Ozeri, and D. J. Wineland, “Surface-electrode architecture for ion-trap quantum information processing”, *Quant. Info. Comput.*, vol. 5, pp. 419, 2005.
- [164] W. Dur, H. J. Briegel, J. I. Cirac, and P. Zoller, “Quantum repeaters based on entanglement purification”, *Phys. Rev. A.*, vol. 59, pp. 169, 1999.
- [165] A. M. Steane, “Error correcting codes in quantum theory”, *Phys. Rev. Lett.*, vol. 77, pp. 793, 1996.
- [166] T. M. Metodi, D. D. Thaker, and F. T. Chong, “”, in *Proceedings of the 5th Workshop on Non-Silicon Computing (NSC-5)*, 2007.
- [167] K. M. Svore, D. P. DiVincenzo, and B. M. Terhal, “Noise threshold for a fault-tolerant two-dimensional lattice architecture”, *Quant. Inf. Comp.*, vol. 7, pp. 297, 2007.
- [168] D. Gottesman, “Fault tolerant quantum computation with local gates”, *J. of Mod. Opt.*, vol. 47, pp. 333, 2000.

- [169] R. Ozeri, C. Langer, J. D. Jost, B. DeMarco, A. Ben-Kish, B. R. Blakestad, J. Britton, J. Chiaverini, W. M. Itano, D. B. Hume, D. Leibfried, T. Rosenband, P. O. Schmidt, and D. J. Wineland, “Hyperfine coherence in the presence of spontaneous photon scattering”, *Phys. Rev. Lett.*, vol. 95, pp. 030403, 2005.
- [170] S. Seidelin, J. Chiaverini, R. Reichle, J. J. Bollinger, D. Leibfried, J. Britton, J. H. Wesenberg, R. B. Blakestad, R. J. Epstein, D. B. Hume, W. M. Itano, J. D. Jost, C. Langer, R. Ozeri, N. Shiga, and D. J. Wineland, “Microfabricated surface-electrode ion trap for scalable quantum information processing”, *Phys. Rev. Lett.*, vol. 96, pp. 253003, 2006.
- [171] R. Reichle, D. Leibfried, E. Knill, J. Britton, R. Blakestad, J. Jost, C. Langer, R. Ozeri, S. Seidelin, and D. Wineland, “Experimental purification of two-atom entanglement”, *Nature*, vol. 443, pp. 838, 2006.
- [172] A. M. Steane, “Overhead and noise threshold of fault-tolerant quantum error correction”, *Phys. Rev. A*, vol. 68, pp. 042322, 2003.
- [173] P. Aliferis, D. Gottesman, and J. Preskill, “Quantum accuracy threshold for concatenated distance-3 codes”, *Quant. Inf. Comp.*, vol. 6, pp. 97, 2007.
- [174] K. Walasek and K. Lukierska-Walasek, “Quantum transverse Ising spin-glass model in the mean-field approximation”, *Phys. Rev. B*, vol. 34, pp. 4962, 1986.
- [175] R. Moessner and S. L. Sondhi, “Ising models of quantum frustration”, *Phys. Rev. B*, vol. 63, pp. 224401, 2001.
- [176] S. Beauregard, “Circuit for Shor’s algorithm using $2n+3$ qubits”, *Quant. Inf. and Comp.*, vol. 3, no. 2, pp. 175, 2003.
- [177] R. V. Meter and K. M. Itoh, “Fast quantum modular exponentiation”, *Phys. Rev. A*, vol. 71, pp. 052320, 2005.
- [178] S. Istrail, “Statistical mechanics, three-dimensionality and NP-completeness: I. universality of intracatability for the partition function of the Ising model across non-planar surfaces”, in *Proceedings of the 32nd annual ACM Symposium on Theory of Computing*, New York, NY, 2000, p. 87, ACM.
- [179] S. Schiller and V. Korobov, “Tests of time independence of the electron and nuclear masses with ultracold molecules”, *Phys. Rev. A*, vol. 71, no. 3, Part A, pp. 032505, 2005.
- [180] M. Kajita, M. Abe, M. Hada, and Y. Moriwaki, “Estimated accuracies of pure $XH(+)$ (X: even isotopes of group II atoms) vibrational transition frequencies: towards the test of the variance $m(p)/m(e)$ ”, *J. Phys. B*, vol. 44, no. 2, 2011.